Hydrodynamics and energy capture characteristics of floating wave-energy harvesting platforms

Haitao Wu

Department of Naval Architecture, Ocean and Marine Engineering

University of Strathclyde, Glasgow

July 28, 2026

This thesis is the result of the author's original research. It has been composed by the author and has not been previously submitted for examination which has led to the award of a degree.

The copyright of this thesis belongs to the author under the terms of the United Kingdom Copyright Acts as qualified by University of Strathclyde Regulation 3.50. Due acknowledgment must always be made of the use of any material contained in, or derived from, this thesis.

Signed:

Date:

Abstract

In the context of escalating global climate change, many countries have proposed carbon neutrality targets to reduce greenhouse gas emissions and promote a transition toward a low-carbon and sustainable energy structure. In this regard, the development and utilization of renewable energy sources have become a critical pathway, with marine energy gaining significant attention due to its abundant reserves and minimal environmental impact. Compared with other types of marine energy, wave energy is featured for greater stability, high energy density, and reduced susceptibility to diurnal and seasonal variations, making it a vital component of the marine renewable energy sector.

However, standalone wave energy devices still face challenges related to energy capture efficiency, structural stability, and economic viability, which limit their large-scale commercial deployment. In recent years, the integration of wave energy converters (WECs) with some floating offshore structures has emerged as a promising solution. Such integrated systems not only enhance energy utilization efficiency but also enable infrastructure sharing, reducing construction and operational costs. To promote the development of wave energy, this thesis proposes a new floating wave-energy harvesting platform concept, which consists of a SPIC concept semi-submersible floating platform and multiple point-absorber WECs.

Abstract

Extensive studies about wave-energy capture platforms have been conducted on the effects of WEC configurations, mooring systems, and PTO devices on system performance under regular or long-crested wave conditions. However, few works have considered wave–current interaction (WCI) and wave directional spreading, despite the fact that these environmental factors are commonly encountered in realistic sea states. Exploring their influences on system performance is of great significance for the design and assessment of wave-energy capture platforms.

Accordingly, this paper primarily investigates the dynamic responses and energy capture performance of the proposed wave-energy capture platform under WCI, short-crested waves, and their combined effects. To evaluate the effects of WCI and wave directional distribution, as well as to facilitate future studies on more complex multi-body connected systems, this work develops a coupled time-domain hydro-connection-mooring analysis tool based on potential flow theory, the Lagrange multiplier method, and the lumped mass method.

The results demonstrate that the wave directional spreading and WCI significantly affect platform motions, mooring loads, and wave-energy conversion efficiency, highlighting the necessity of considering these two environmental factors in realistic ocean conditions for the design and assessment of wave-energy harvesting platforms.

Contents

List of Figures

List of Tables

List of the publications

[1] **Wu H**, Zhu F*, Yuan Z* (2023). Effects of the WEC shape on the performance of a novel hybrid WEC-FOWT system. *Energy*. 288: 129907.

[2] **Wu H**, Yuan Z* (2024). Numerical investigation of the effects of short-crested irregular waves on the performance of a floating power capture platform. *Ocean Engineering*. 313: 119548.

[3] **Wu H**, Deng W*, Yuan Z* (2024). Numerical investigation of the effects of wave-current interaction on the dynamic responses of a floating power harvesting platform. *Physics of Fluids*. 36: 107115.

[4] **Wu H**, Yuan Z* (2025). WEC spacing effects on the performance of a floating energy harvesting platform. *Ocean Engineering*. 327: 120971.

[5] **Wu H**, Deng W*, Yuan Z* (2025). Effects of short-crestedness and currents on the dynamic response of a floating wave-energy harvesting platform. *Physics of Fluids*. 37: 037202.

[6] **Wu H**, Zhu F, Yuan Z* (2025). Performance analysis of the oscillating-body wave energy converter with a novel bistable mechanism under ir-

regular wave conditions. *Proceedings of the Institution of Mechanical Engineers, Part M: Journal of Engineering for the Maritime Environment.* 1-13.

[7] **Wu H**, Liao B, Deng W*, Yuan Z*. (2025). Effects of hinge properties on the hydroelastic response of an interconnected very large floating structure under wave-current interactions. *Physics of Fluids.* 37: 087194.

[8] **Wu H**, Yuan Z* (2026). Performance investigation of an oscillating-body WEC with the tristable energy capture mechanism. *Ocean Engineering.* 343: 123538.

[9] **Wu H**, Yuan Z* (2026). Influence of WEC geometric variables on the performance of an integrated WEC-VLFS system. *Ocean Engineering.* 352: 124470.

[10] **Wu H**, Jia L, Xu X, et al (2026). Hydroelasticity and power capture of raft-type WEC–interconnected VLFS configuration. *Ocean Engineering.* 363: 126646.

[11] **Wu H**, Liao B, Yuan Z* (2026). Hydroelastic analysis of a VLFS under wave-current interactions. *Ships and Offshore Structures.* (accepted)

[12] Zhang Z, Bu Y, **Wu H***, et al (2023). Parametric study of the effects of clump weights on the performance of a novel wind-wave hybrid system. *Renewable Energy.* 219: 119464.

[13] Zhang Z, Chen X, **Wu H***, et al (2023). Numerical study of a novel hybrid system with the wavestar wave energy converter array and a SPIC semi-submersible floating platform. *Journal of Cleaner Production*. 407: 137178.

[14] Cui L, **Wu H***, Li M, et al (2024). Effects of mooring failure on the dynamic behavior of the power capture platforms. *Energy*. 313: 133761.

[15] Zhang Z, Guan L, **Wu H***, et al (2024). Effects of the second-order hydrodynamics on the dynamic behavior of the platform among the wind-wave hybrid systems. *Journal of Engineering Research*. 13: 1603-16.

[16] Zhang Z, Dai L, Wang Z, **Wu H*** (2026). Effects of WEC geometry on the performance of WEC array-VLFS integrated system. *Polish Maritime Research*. 33(1): 63-73.

[17] Zhang Z, Lyu S, Morhun S, Liu W, Cui L, **Wu H*** (2026). Failure Risk Assessment and Dominant Cause Analysis of an Integrated Point-Absorber Wave Energy Converter in a Semi-Submersible Wind–Wave Hybrid System. *Ocean Engineering*. 364: 127059.

[18] Deng W, Liu D, Liu L, Li Y, **Wu H***, et al (2026). Coupled dynamic response of a floating vertical axis wind turbine under floater motions. *Ocean Engineering*. 358: 125792.

[19] Deng W, Sun M, **Wu H***, et al (2025). Effects of strut arrangement

on the dynamic responses of H-type floating vertical axis wind turbines. *China Ocean Engineering.* (accepted)

[20] **Wu H**, Xu X, Ji R, et al (2026). Hydroelastic response and power capture of an interconnected VLFS with a WEC device under wave–current interaction. *Ocean Engineering.* (under review)

[21] Zhang Z, Ge Y, Liu W, **Wu H*** (2026). A Multi-Criteria Decision Model for Failure Analysis of Offshore Structures: A Case Study on a Point-Absorber Wave Energy Converter. *Ocean Engineering.* (under review)

Acknowledgment

First and foremost, I would like to express my sincere gratitude to Dr. Zhiming Yuan for his generous financial support and for granting me the academic freedom to pursue research topics that genuinely interest me. It has been a great privilege to undertake my doctoral studies under his supervision. I have benefited greatly from his open-minded perspective, innovative research vision, and continued support. The past several years in Glasgow have been both intellectually rewarding and personally memorable.

I am also grateful to Dr. Laibin Jia and Dr. Saishuai Dai for their valuable advice and kind encouragement throughout my doctoral research. My thanks also go to Dr. Wanru Deng, Mr. Binteng Gu, Mr. Maokai Sun, Mr. Yinhua Liu, Dr. Yang Huang, Dr. Fengshen Zhu, and all friends and colleagues in Glasgow who shared this journey with me. The time spent working and living alongside you has been a pleasure and will remain a cherished memory.

I would like to extend my sincere appreciation to Prof. Zhiyang Zhang (Jiangsu Ocean University), Prof. Siming Zheng (Zhejiang University), Prof. Yang Zhao and Prof. Aijun Li (Ocean University of China), Prof. Hui Liang (Technology Centre for Offshore and Marine, Singapore), Prof. Peiwen Cong (Dalian University of Technology), and Prof. Xuanlie Zhao (Harbin Engineering University). I am grateful for their rigorous and insightful guidance when I encountered challenges in my research, from which I have benefited considerably.

My thanks also go to Mrs. Susan Pawson and all other staff of the NAOME for their efficient and professional support, which has greatly facilitated my PhD career.

Finally, I wish to express my deepest gratitude to my girlfriend, Siqi Wu, for her patience, understanding, and steadfast support over the years. I am profoundly grateful to my family for their unconditional love, encouragement, and constant support. It is their unwavering belief in me that has enabled me to complete this doctoral journey and move forward with confidence.

“ 天行健，君子以自强不息；地势坤，君子以厚德载物。 ” ——《周易》

"As Heaven moves with strength and vigor, a noble person should strive constantly for self-improvement; as Earth is broad and receptive, a noble person should carry all things with great virtue."

——I ching (The Book of changes)

Chapter 1

Introduction

1.1 Background

Replacing traditional fossil fuels with renewable energy can significantly accelerate the goal of achieving a carbon-neutral world by 2050 [1]. Wherein, ocean energy is a crucial focus area for exploiting renewable energy. It is worth noting that wind energy, wave energy, tidal energy, and photovoltaic energy are the four primary types of ocean energy. Among them, wave energy is considered much promising due to its higher energy density and capability for continuous operation [2]. The theoretical global wave energy resource is considerable [3], highlighting its potential to expedite the decarbonization of global electricity supply. After years of development, five main types of WECs have emerged: oscillating water column (OWC), overtopping, point-absorber, oscillating-surge and raft-type devices, as seem in Figure 1.1 [4]. Among them, the point-absorber WECs have garnered significant attention from academia and industry due to the relatively high energy conversion efficiency, minimal environmental impact, low construction and installation costs, and flexible deployment configurations [5].

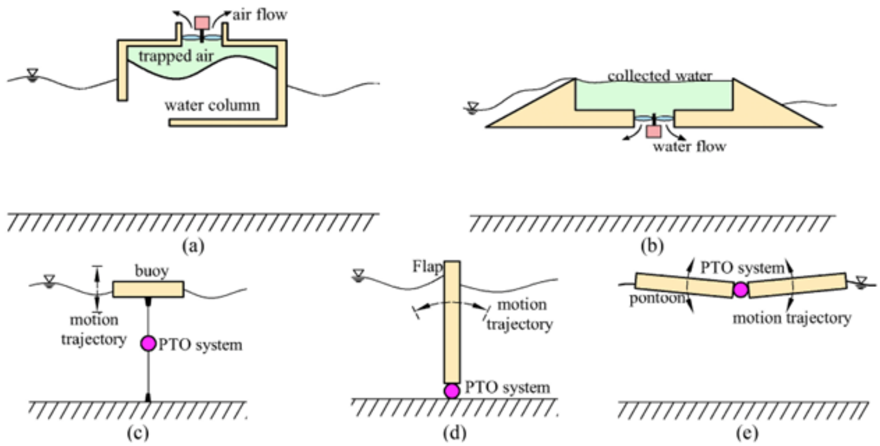

Figure 1.1: Various WECs: (a) OWC WEC, (b) overtopping WEC, (c) point-absorber WEC, (d) oscillating-surge WEC, (e) raft-type WEC [4].

However, standalone wave energy devices still face challenges related to structural stability and economic viability, which limit their large-scale commercial deployment. In recent years, the integration of the WECs with the offshore wind turbines or platforms has emerged as a promising research direction [6]. Figures 1.2-1.4 illustrate various integrated systems capable of harvesting wave energy [7–11]. Such concepts not only enhance energy utilization efficiency but also enable infrastructure sharing, reducing construction and operational costs [10]. More importantly, these integrated systems can play a crucial role in the global carbon neutrality agenda by providing an innovative technological pathway for offshore renewable energy development, thereby contributing to the transition toward a cleaner and more sustainable energy future.

In the design and performance analysis of offshore structures, environmental modeling and response assessment are typically conducted based on the actual sea conditions of the region where the structure operates. Inaccurate representation of environmental conditions may lead to biased estimations of structural responses, thereby reducing operational efficiency and even posing potential safety

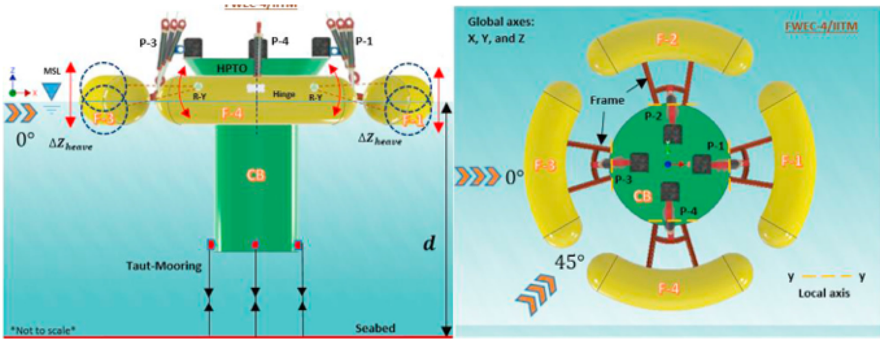

Figure 1.2: WEC array-TLP integrated system [7].

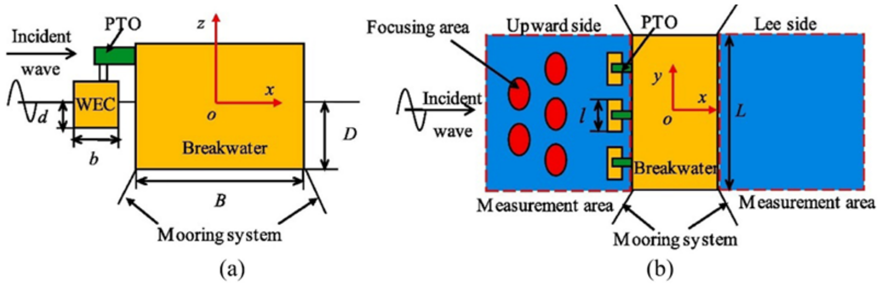

Figure 1.3: WEC array-breakwater integrated system [8].

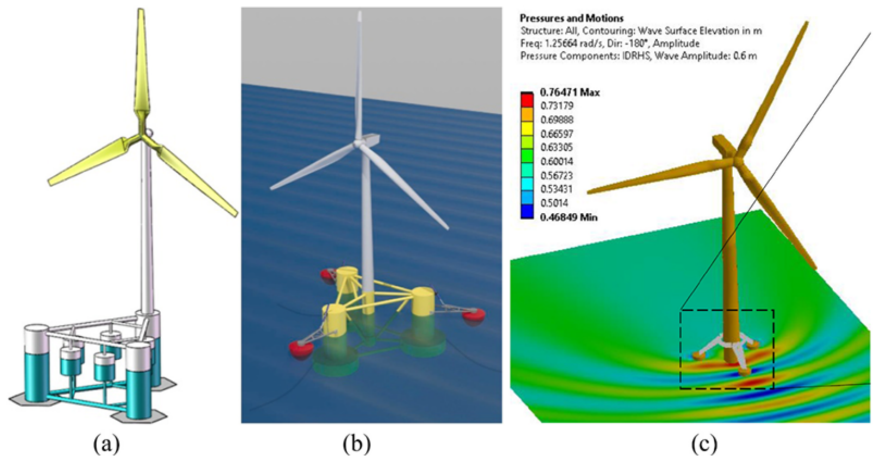

Figure 1.4: Wind-wave energy hybrid systems [9-11].

risks.

It is worth noting that short-crested waves and WCI are common and important physical phenomena in marine environments; therefore, they should be properly represented and accurately modeled in related studies and engineering analysis.

Regarding short-crested waves, they are generated by the superposition of multiple wave components propagating in different directions with random phases [12]. Unlike long-crested waves, short-crested waves exhibit finite crest lengths and directional spreading characteristic.They are commonly described using a two-dimensional (2D) frequency–direction wave spectrum [13], which more realistically represents the directional spreading of wave energy in natural seas and constitutes the predominant form of actual sea states. Investigating the effects of short-crested waves on the responses of marine structures is of significant engineering importance. Directional wave spreading can markedly alter the load and motion characteristics of structures [14]. Compared with the conventional long-crested wave assumption, short-crested wave models generally provide more realistic predictions of the dynamic responses of offshore systems under operational sea states. Therefore, incorporating short-crested wave effects is essential for reliable performance assessment and structural design.

In addition, WCI can alter wave characteristics such as wave frequency, wavelength, and propagation speed through current-induced modifications to wave dispersion and energy distribution [15,16]. Under WCI conditions, the wave actions on marine structures are no longer governed solely by waves or currents acting independently, but instead exhibit pronounced coupled effects [17]. Consequently, WCI can significantly modify the wave loads and dynamic response characteristics of structures, thereby exerting a notable influence on their station-keeping performance and mooring system loads [18]. If wave–current coupling effects are neglected in engineering analyses, the resulting load levels and structural responses may be wrongly estimated, particularly under strong current conditions or in complex sea states. Therefore, proper consideration of WCI is an essential prerequisite for improving the accuracy of load predictions and ensuring the structural safety of marine structures.

To promote the development of wave energy utilization, this thesis proposes a new floating wave-energy capture platform, which is composed of a SPIC semi-submersible platform system and multiple oscillating-body WECs, aiming to provide a promising option for efficient energy harvesting. Although numerous wave-energy capture systems have been proposed and investigated, the effects of short-crested waves and WCI on their performance have received limited attention. Therefore, the focus of this thesis is to evaluate the impacts of these two factors on the dynamic response and energy capture of the proposed wave-energy harvesting platform. Finally, the structure of this thesis is organized as follows: Chapter 1 presents the introduction, Chapter 2 describes the methodology, Chapters 3 through 5 constitute the core content, and Chapter 6 summarizes the main conclusions.

1.2 Literature Review

Section 1.2.1 presents the related literature review of the wave-energy capture platforms, consisting of a semi-submersible platform and oscillating-body WECs. In addition, the works on short-crested waves and WCI is reviewed in Sections

1.2.2 and 1.2.3, respectively.

1.2.1 Wave-energy capture systems with the floating semi-submersible platforms and oscillating-body WECs

For wave-energy capture platforms based on semi-submersible foundations, extensive studies have been conducted on WEC configurations, mooring arrangements, and PTO systems.

Regarding WEC configurations, previous studies have mainly focused on the effects of WEC shape, size, number, and layout. Ghafari et al. [19] presented a hybrid concept mounting Wavestar WECs on a DeepCwind semisubmersible platform, and evaluated the influence of WEC size on the platform motion and captured power. Wang et al. [20] investigated the performance of a floating braceless semi-submersible wind turbine with different shapes of heaving-type WECs. Chen et al. [21] evaluated the effects of the WEC number on the hydrodynamics of a wave-wind hybrid concept, concluding that the WEC increase improved the system stability under realistic sea states. Zhu et al. [22] investigated an integrated system with a point-absorber WEC array and a semi-submersible platform. They analyzed the influence of the WEC parameters on the platform response and the energy conversion of the WEC array. Jin et al. [23] performed a optimization analysis to investigate the impact of the WEC layout on the performance of integrated system composed of an oscillating-body WEC array and a semi-submersible wind turbine.

In addition to WEC configurations, the mooring system has also been widely investigated. Zhang et al. [24] designed a novel mooring configuration for an integrated ocean energy system, consisting of catenary chains and counterweights, and conducted a sensitivity analysis on the counterweights. Sun et al. [25] proposed an integrated system consisting of a semi-submersible central platform and multiple WEC buoys, and conducted a comparative analysis on the effects of different mooring configurations on the performance of the system. Cui et al. [26] investigated the effects of mooring line failure on the performance of the wave-energy capture platforms consisting of the point-absorber WEC array and the SPIC semi-submersible platform. Lee et al. [27] proposed a noval semi-taut mooring system for an integrated system combining a semi-submersible platform and a heaving-type WEC, and studied the influence of mooring parameters on the platform motion and mooring line tension.

Another important research focus is the PTO system. Li et al. [28] proposed a hybrid system composed of a semi-submersible platform and a torus-type WEC array, and investigated the impact of PTO damping on the power capture performance of the WECs. Chen et al. [29] adopted the numerical and environmental analysis of the effects of the PTO control on the dynamic behavior of the floating wind-wave integrated system. Homayoun et al. [30] studied a integrated energy harvesting system composed of a heaving WEC array and a semi-submersible wind turbine. The energy conversion was optimized by considering five PTO damping coefficients under six environmental conditions. Liu et al. [31] compared the wave capture performance and dynamic response of an integrated system combining a semi-submersible platform and multiple point-absorber WECs under different control strategies of the PTO system.

Although extensive studies have been conducted on WEC configurations, mooring arrangements, and PTO systems, limited attention has been paid to the influence of complex environmental conditions on the performance of this type of wave-energy harvesting systems. Investigating the dynamic responses and power capture characteristics of wave-energy harvesting systems under complex but common environmental conditions is also essential for their engineering design and performance assessment. Accordingly, this thesis focuses on the effects of representative complex environmental conditions, including short-crested waves and WCI, on the proposed wave-energy harvesting system. The literature on these two environmental factors is reviewed in Sections 1.2.2 and 1.2.3, respectively.

1.2.2 Short-crested irregular waves

In marine environments, multidirectionally propagating short-crested waves are commonly encountered, and their characteristics differ significantly from those of long-crested waves [32]. Therefore, accounting for wave directionality is essential for accurately predicting the response and ensuring safety of offshore structures. In general, a short-crested wave spectrum can be simulated by the product of a long-crested wave spectrum and a directional spreading function [33].

Numerous researchers have investigated the responses of various offshore structures in short-crested waves through experimental, analytical and numerical perspectives. Tödter et al. [34] conducted the experimental tests on the effects of short-crested wave conditions on the impact loads due to the tank's sloshing. Zhang et al. [35] experimentally analyzed the hydrodynamic interactions between the short-crested waves and a vertical pile array. Jiao et al. [36] utilized an experimental study to identify the differences in ship motion and load response under short-crested and long-crested wave conditions. Göteman et al. [37] compared the energy conversion of a point-absorber WEC array in long-crested and short-crested waves with an analytical approach. Ji et al. [38] investigated the influence of wave directionality on the wave run-ups and forces of a vertically fixed cylindrical array in short-crested waves. Sørum et al. [39] predicted the fatigue damage of bottom-fixed wind turbine under different wave parameters. Viuf et al. [40] evaluated the impact of wave directionality on the extreme response of a simplified end-anchored pontoon bridge. Li et al. [33] analyzed the the dynamic response of a semi-submersible floating wind turbine under short-crested waves.

Despite extensive research on the effects of short-crested waves on various offshore structures, few studies have focused on wave-energy harvesting platforms. To address this gap, one of the objectives of this thesis is to examine the dynamic responses and energy capture characteristics of the proposed wave-energy harvesting system under different wave directional spreading conditions.

1.2.3 Wave-current interactions

With the action of currents, the irregular wave profile changes due to the wave-current interactions, which may significantly affect the structural or hydrodynamic response of the marine structures. Therefore, considering WCI is crucial to maintain their safe operation in irregular waves with currents.

The spectral method is a widely used approach for simulating irregular waves with current-induced modification. Tung and Huang [41], and Huang et al. [15] proposed the spectral models that accounted for the random wave-current interaction. Hedges et al. [16] subsequently extended these models to solve for the impact of opposing currents on wave spectrum. Soares and De Pablo [42], Lai et al. [43], and Thomas [44] validated these models through numerical simulations and experimental tests, demonstrating their accuracy.

In recent years, numerous studies have adopted the spectral models to analyse the dynamic response of the offshore structures based on potential-flow model. Chen and Basu [45] investigated the structural behavior of an offshore wind turbine with WCI. Sarkar et al. [46] proposed an innovative pitch control strategy for a spar-type wind turbine, and analyzed its performance under WCI. Qu et al. [47] established the coupled numerical model of a floating wind turbine, and simulated its performance in freak waves with uniform currents. Elobeid et al. [18] evaluated the influence of WCI on the performance of a semi-submersible wind turbine.

In addition to the spectral method, another commonly used approach accounts for WCI through incorporating a steady potential into the potential-flow model. The wave loads exerted on offshore structures are calculated based on the unchanged wave spectra. Xin et al. [48] analyzed the hydrodynamic loads on a vertically-fixed cylinder under the decoupled and coupled effects of WCI. Mazarakos et al. [49] studied the dynamic behavior of the semi-submersible FWT under the uniform currents and regular waves. Dai et al. [17] conducted a parametric analysis to evaluate the effects of WCI on a large floating bridge. However, the steady-potential-based approach still has limitations in the calculation of second-order wave forces under the influence of currents [50].

Although various offshore structures have been investigated under WCI, limited attention has been paid to wave-energy harvesting platforms. To address this research gap, the remaining objectives of this thesis are to employ the spectral method to examine the dynamic responses and wave energy capture characteristics of the proposed wave-energy harvesting system under the combined effects of irregular waves and currents, including both long-crested and short-crested irregular wave conditions.

1.3 Aim and objectives

Currently, commonly used commercial hydrodynamic analysis software has limited capability to directly simulate complex multi-body connected systems. Although they can be simulated indirectly through user-defined development interfaces, the procedure is often cumbersome and requires complex mechanical derivations. Therefore, to enable more convenient future investigation of more complex multi-body connected systems, this work develops a coupled hydro–connected-mooring time-domain numerical model based on potential-flow theory, the Lagrange multiplier method, and the lumped-mass method. The detailed methodology and governing formulations are provided in Chapter 2.

The primary objectives are to investigate the effects of wave directional spreading and WCI on the performance of this integrated system. Through the results obtained from the developed numerical model, this thesis aims to provide useful references for the performance assessment and engineering design of this type of wave energy structures. The specific research objectives are as follows:

- to predict the performance of the wave-energy harvesting platform in short-crested irregular waves in **Chapter 3**.
- to analyze the influence of WCI on the performance of the wave-energy capture system under long-crested irregular wave conditions in **Chapter 4**.
- to investigate the effects of wave directional distributions on the perfor-

mance of the wave-energy capture system under WCI in **Chapter 5**.

1.4 Main contribution

The main contribution of this thesis lies in exploring the performance of a new floating wave-energy harvesting platform under short-crested waves and WCI, considered both individually and in combination. In previous studies on wave-energy capture platforms, limited attention has been paid to wave directional spreading and WCI, which are both commonly encountered in realistic marine environments.

The key findings of this work demonstrate that WCI and wave directional spreading significantly affect the performance of the proposed wave-energy harvesting system. Therefore, this thesis highlights the importance of accounting for these two factors in the design and assessment of offshore structures, as considering only long-crested waves or neglecting WCI may adversely affect their operational performance and safety.

1.5 Thesis outline

The structure of this thesis is illustrated in Figure 1.5, and a brief overview of each chapter is provided below:

- **Chapter 1** introduces the research background, presents a comprehensive review of the existing literature, outlines the research aims and objectives, highlights the main contributions of this work, and provides an overview of the thesis structure.

- **Chapter 2** introduces the methodology background for developing the coupled time-domain dynamic model of a floating multi-body connected system.
- **Chapter 3** predicts the performance of the floating wave-energy capture system under short-crested waves with different directional distributions.
- **Chapter 4** evaluates the influence of WCI on the performance of the floating wave-energy harvesting platform under combined irregular wave–current conditions.
- **Chapter 5** compares the performance of the floating wave-energy harvesting platform under long-crested and short-crested waves with WCI effects.
- **Chapter 6** summarizes the main findings of this theis and outlines directions for future research.

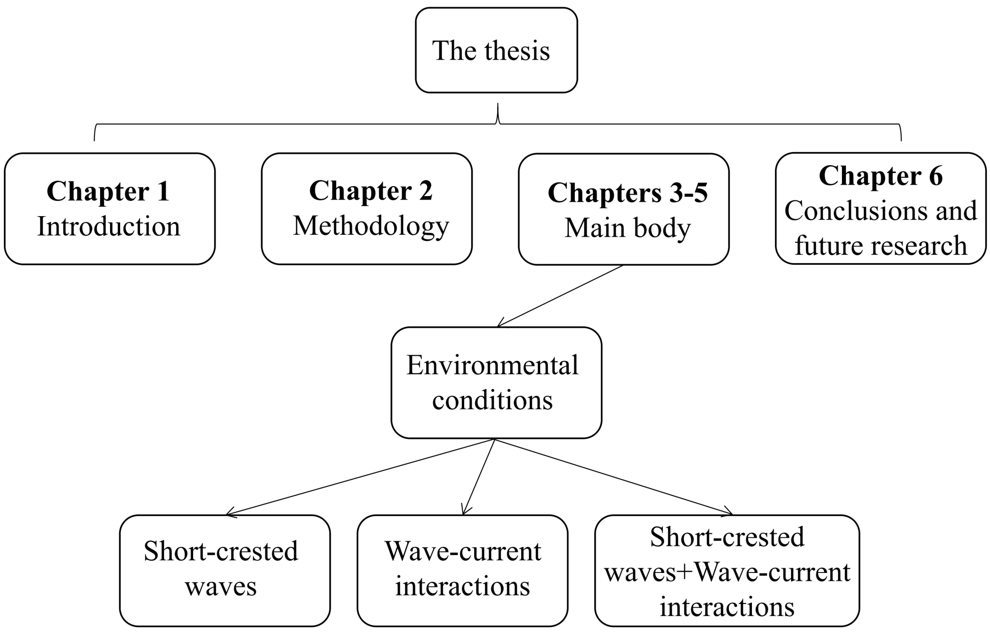

Figure 1.5: Thesis outline.

Chapter 2

Methodology

This thesis investigates a new floating wave-energy harvesting platform composed of a SPIC concept semi-submersible platform system and multiple point-absorber WECs, as seen in Figure 2.1. The figure also presents the numbering convention for the individual WECs, WEC rows and mooring lines. In order to arrange the WEC array symmetrically onto the platform, three horizontal cross braces are set between each side column and the central column. The relative rotational motion between the WECs and the platform can activate the PTO mechanism for wave energy extraction, in which the PTO device is simplified as a hinge connector equipped with rotational damping [21]. The main parameters of the semi-submersible platform, mooring system and point-absorber WEC are listed in Tables 2.1-2.3, respectively [26, 51].

Basically, the proposed wave-energy harvesting platform is a floating multi-body hinged system. To predict its dynamic responses and wave energy capture, a coupled hydro-connected-mooring analysis model is established based on the 3D potential flow theory, lumped mass method and Lagrange multiplier technique. The current chapter introduces the theoretical background underlying this cou-

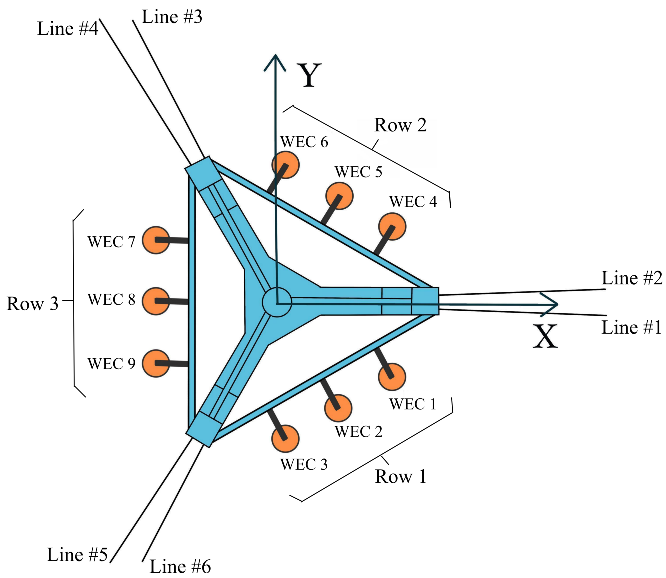

(a) plan view

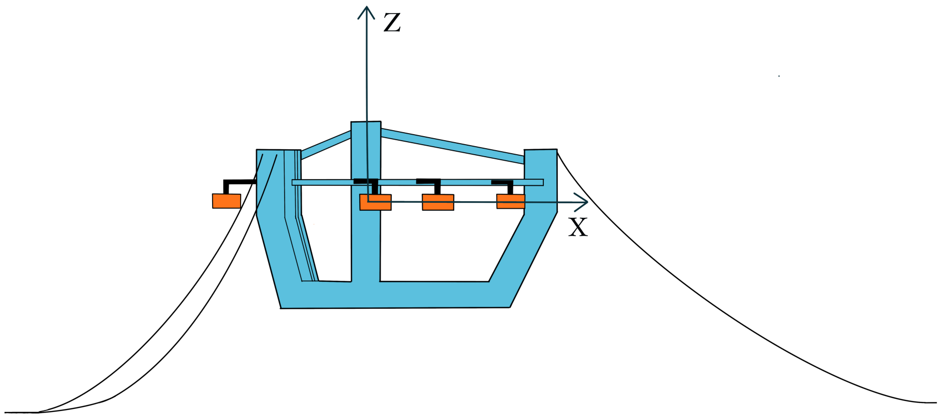

(b) side view

Figure 2.1: Illustration of the floating wave-energy harvesting platform: (a) plan view, (b) side view.

Table 2.1: Main parameters of the SPIC concept semi-submersible platform [50].

Parameter	**Value**
Draft (m)	30
Displacement (kg)	1.64×10^7
Mass (kg)	1.61×10^7
Center of gravity (CoG) below mean water line (MWL) (m)	9.68
Radius of gyration around x-axis (R_{xx}) (m)	37.00
Radius of gyration around y-axis (R_{yy}) (m)	37.00
Radius of gyration around z-axis (R_{zz}) (m)	20.00

Table 2.2: Main parameters of mooring system [50].

Parameter	**Value**
Number of mooring lines	6
Fairlead above MWL (m)	15
Anchor below MWL (m)	60
Angle between adjacent lines (deg)	5
Angle between each set of lines (deg)	120
Radius from platform center to fairleads (m)	54.5
Radius from platform center to anchors (m)	830.0
Length of mooring line (m)	800.0
Outer diameter of mooring line (m)	0.120
Mass in water (t/m)	0.303
Axial stiffness (kN)	1.243×10^6

Table 2.3: Main properties of the point-absorber WEC [26].

Property	**Value**
Radius (m)	4.402
Draft (m)	2.201
Elevation above MWL (m)	2.201
Elevation of hinge point above MWL (m)	5.987
Horizontal distance of hinge point from CoG (m)	10.696
Mass (kg)	1.484×10^5
CoG below MWL (m)	0
Roll inertia (kg·m^2)	1.097×10^6
Pitch inertia (kg·m^2)	1.540×10^6
Yaw inertia (kg·m^2)	1.701×10^6

pled model, which is organized as follows: Section 2.1 presents the potential flow theory, including the governing equations of the boundary value problem, as well as the hydrodynamic coefficients and the wave excitation force transfer functions. The irregular wave spectrum and the wave excitation forces in the time domain are derived in Sections 2.2 and 2.3, respectively. The lumped mass method is described to model the mooring lines in Section 2.4. Section 2.5 introduces the principles of the Lagrange multiplier method regarding the hinge constraints. The time-domain motion equation for this integrated system is given in Section 2.6.

Section 2.7 derives the captured power of the individual WEC.

Before introducing the theoretical methodology, the coordinate systems need to be defined. In the present study, two coordinate systems are adopted, namely the global coordinate system (O-XYZ) and body-fixed coordinate system (o-xyz). The global coordinate system is used as the reference frame for the analysis, while the body-fixed coordinate system has its origin located at the CoG of the rigid body and moves together with the body. In the global coordinate system, the XOY plane coincides with the still water surface, and the Z-axis is oriented upward normal to the still water surface. When the rigid body is in its initial position, the body-fixed axes are parallel to the global coordinate axes, as illustrated in Figure 2.2. It should be noted that the rigid body has six degrees of freedom (DoFs), namely surge, sway, heave, roll, pitch, and yaw. Among them, surge, sway, and heave correspond to translational motions along the x-, y-, and z-axes, respectively, with their positive directions defined as the positive directions of the corresponding axes. Roll, pitch, and yaw represent rotational motions about the x-, y-, and z-axes, respectively, and their positive directions follow the right-hand rule.

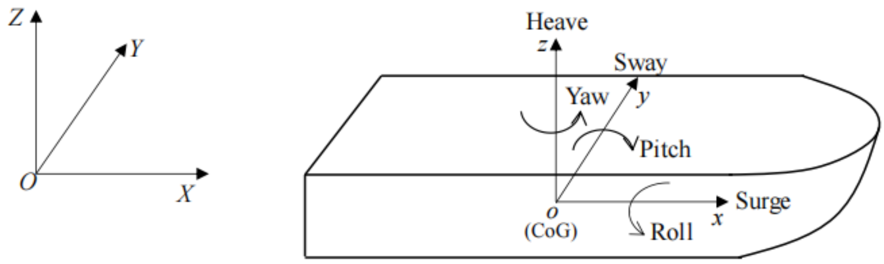

Figure 2.2: Schematic diagram of the global coordinate and body-fixed coordinate systems.

2.1 3D potential theory

Two commonly used approaches for investigating the dynamic response of large-scale floating structures and the associated fluid field are the potential-flow method and computational fluid dynamics (CFD). CFD can resolve viscous flow phenomena and the detailed evolution of the surrounding fluid field, and is therefore more suitable for capturing complex local flow features such as flow separation and vortex shedding. These effects can be particularly important for structures with sharp-edged geometrical features. In contrast, the potential-flow method is based on the assumptions of inviscid and irrotational flow, and therefore cannot directly capture viscous effects or detailed local flow evolution.

Despite these limitations, potential-flow-based models are widely used for predicting the global dynamic response of large-scale floating structures because of their high computational efficiency. In mild to moderate sea states, where strongly nonlinear viscous effects are not dominant, the potential-flow method with viscous corrections can provide reasonably accurate predictions of the dynamic response while requiring significantly lower computational cost than CFD [52]. The viscous effects associated with the structure can be incorporated through empirical formulations [53], or calibrated using CFD simulations [54] and experimental measurements [55]. It should be noted that the viscous correction is not applied directly during the solution of the velocity potential. Instead, the viscous damping estimated from aforementioned methods is incorporated into the equations of motion of the structure.

Under extreme sea states, strongly nonlinear phenomena may reduce the accuracy of potential-flow-based models, even when viscous corrections are included.

Nevertheless, fully resolved CFD simulations remain computationally expensive for long-duration irregular-wave simulations, multi-degree-of-freedom motions, incorporation of mooring systems and multiple environmental load cases. A potential-flow model with viscous corrections can achieve a reasonable balance between computational efficiency and response-prediction accuracy in practical engineering studies [56]. Therefore, this method is adopted in this work to investigate the dynamic response of the wave-energy capture system under both operational and extreme sea states.

2.1.1 Boundary-value problem

Based on the three-dimensional (3D) potential flow theory, the fluid is assumed to be incompressible, inviscid, and irrotational. Under these assumptions, the velocity potential satisfies the Laplace equation,

$$\nabla^2 \Phi = 0 \tag{2.1}$$

Additionally, the fluid velocity potential Φ can be expressed as the superposition of the incident potential Φ_I, diffraction potential Φ_D, and radiation potential Φ_R [57],

$$\Phi(t) = \Phi_I + \Phi_D + \Phi_R = \mathrm{Re}\left[\left(\varphi_I + \varphi_D + \sum_{m=1}^{M}\sum_{j=1}^{6} \xi_j^{(m)} \varphi_{rj}^{(m)}\right) e^{-i\omega t}\right] \tag{2.2}$$

where M is the number of bodies; $\xi_j^{(m)}$ denotes the complex motion amplitude in the j-th DoF of the m-th body, and $\varphi_{rj}^{(m)}$ is the corresponding radiation potential induced by unit amplitude. Under finite water depth condition, the incident potential can be expressed as [58]:

$$\varphi_I = -\frac{igA}{\omega}\frac{\cosh\big(k(z+h)\big)}{\cosh(kh)}e^{i[k(x\cos\theta+y\sin\theta)]} \tag{2.3}$$

where g is the gravity acceleration; A and ω denote the amplitude and circular frequency of the incident wave, respectively; h is the water depth; θ is the incident wave angle; k represents the wave number corresponding to ω,

$$k = \frac{\omega^2}{g\tanh(kh)} \tag{2.4}$$

The boundary value problem (BVP) for the velocity potential is subjected to the following conditions [59]:

$$-\omega^2\varphi^{\times} + g\frac{\partial\varphi^{\times}}{\partial z} = 0, \quad \text{on } S_F(z=0) \tag{2.5}$$

$$\frac{\partial\varphi^{\times}}{\partial z} = 0, \quad \text{on } S_B(z=-h) \tag{2.6}$$

$$\frac{\partial\varphi_D}{\partial n} = \frac{\partial\varphi_I}{\partial n}, \quad \text{on } S_b \tag{2.7}$$

$$\frac{\partial\varphi_{rj}^{(k)}}{\partial n^{(q)}} = \begin{cases} 0, & q \neq k, \\ -i\omega n_j, & q = k, \end{cases} \quad \text{on } S_b \tag{2.8}$$

$$\nabla\varphi \to 0, \quad \text{on } S_\infty \tag{2.9}$$

where S_F, S_B, S_b, S_∞ represent the boundaries of the free surface, seabed, body surface, and far field, respectively; $\varphi^{\times}$ can represent either the diffraction potential or the radiation potential; The generalized normal vector n_j can be defined as:

$$n_j = \begin{cases} \vec{n}, & j = 1 \sim 3 \\ \\ \vec{r} \times \vec{n}, & j = 4 \sim 6 \end{cases} \tag{2.10}$$

where $\vec{n} = (n_1, n_2, n_3)$ is the inward-pointing unit normal vector on the body surface, and $\vec{r} = (x, y, z)$ is the position vector on the body surface.

2.1.2 Hydrodynamic coefficients and wave force transfer functions

After resolving the BVP described in Section 2.1.1 using the boundary element method (BEM) [60], the added mass and radiation damping induced on the q-th body due to the motion of the k-th body can be expressed as, respectively [61]:

$$\mu_{ij}^{(q,k)} = \frac{\rho}{\omega} \iint_{S_q} \mathrm{Im}\Big(\varphi_{rj}^{(k)}\Big)\, n_i \, ds, \qquad (i = 1 \sim 6;\ j = 1 \sim 6) \tag{2.11}$$

$$\lambda_{ij}^{(q,k)} = -\rho \iint_{S_q} \mathrm{Re}\Big(\varphi_{rj}^{(k)}\Big)\, n_i \, ds, \qquad (i = 1 \sim 6;\ j = 1 \sim 6) \tag{2.12}$$

where S_q denotes the mean wetted surface of the q-th body.

The first-order wave excitation forces acting on the body comprise both the Froude-Krylov force and diffraction force. Based on the Bernoulli equation, the first-order wave excitation force transfer function can be obtained by integrating the incident and diffraction pressure over the wetted surface of the body [58],

$$\bar{F}_j^{(1)} = \iint_{S_q} (p_I + p_D)\, n_j \, dS = i\omega\rho \iint_{S_q} (\varphi_I + \varphi_D)\, n_j \, dS, \qquad j = 1, \ldots, 6 \tag{2.13}$$

As for second-order wave forces, they consist of difference-frequency and sum-frequency components. However, for offshore structures such as semi-submersible platforms, the natural frequencies of the platform motions generally do not fall within the dominant frequency range of sum-frequency wave forces [62]. Therefore, the sum-frequency forces are unlikely to excite resonant responses of the platforms. In contrast, the influence of difference-frequency forces on the low-frequency motions of the platforms cannot be neglected. Accordingly, in this work, only the second-order difference-frequency wave forces are considered. Regarding the difference-frequency wave force and moment transfer functions, their generalized forms can be expressed as, respectively [63]:

$$\left(\bar{P}^{(F)}_{jkmn}, \bar{Q}^{(F)}_{jkmn}\right) = -\frac{1}{4}\rho g \int_{WL} \zeta^{(1)}_{jm}\zeta^{(1)*}_{kn}\, \vec{n}\, dl + \frac{1}{4}\rho \iint_{S_q} \left[\nabla\phi^{(1)}_{jm} \cdot \nabla\phi^{(1)*}_{kn}\right] \vec{n}\, dS$$
$$+\frac{1}{2}\rho \iint_{S_q} \left[\vec{X}^{(1)}_{jm} \cdot \nabla \frac{\partial \phi^{(1)*}_{kn}}{\partial t}\right] \vec{n}\, dS + \frac{1}{2}\vec{\alpha}^{(1)}_{jm} \times \vec{F}^{(1)*}_{jm} \tag{2.14}$$

$$\left(\bar{P}^{(M)}_{jkmn}, \bar{Q}^{(M)}_{jkmn}\right) = -\frac{1}{4}\rho g \int_{WL} \zeta^{(1)}_{jm}\zeta^{(1)*}_{kn} (\vec{x} \times \vec{n})\, dl$$
$$+\frac{1}{4}\rho \iint_{S_q} \left[\nabla\phi^{(1)}_{jm} \cdot \nabla\phi^{(1)*}_{kn}\right] (\vec{x} \times \vec{n})\, dS + \frac{1}{2}\rho \iint_{S_q} \left[\vec{X}^{(1)}_{jm} \cdot \nabla \frac{\partial \phi^{(1)*}_{kn}}{\partial t}\right] (\vec{x} \times \vec{n})\, dS$$
$$+\frac{1}{2}\vec{\alpha}^{(1)}_{jm} \times \vec{M}^{(1)*}_{jm} \tag{2.15}$$

where $\zeta^{(1)}_r$, $\phi^{(1)}$, $\vec{X}^{(1)}$, $\vec{\alpha}^{(1)}$, $\vec{F}^{(1)}$ and $\vec{M}^{(1)}$ denote the first-order relative wave elevation, velocity potential, displacement, rotation, hydrodynamic force and moment under unit wave amplitude, respectively; m and j represent the m-th incident wave direction and the j-th wave component under the corresponding direction, respectively; Similarly, n and k denote the n-th incident wave direction and the k-th wave component under the corresponding direction, respectively.

To improve computational efficiency, the Newman approximation method is widely employed in engineering applications when calculating second-order difference-frequency drift forces [64]. The core of this approach is to approximate the off-diagonal elements of the second-order transfer function matrix using its diagonal elements [65],

$$\begin{cases} \bar{P}^{(*)}_{jkmn} = \dfrac{1}{2}\left(\bar{P}^{(*)}_{jjmn} + \bar{P}^{(*)}_{kkmn}\right) \\ \bar{Q}^{(*)}_{jkmn} = \dfrac{1}{2}\left(\bar{Q}^{(*)}_{jjmn} - \bar{Q}^{(*)}_{kkmn}\right) \end{cases} \tag{2.16}$$

where * can denote F or M.

It should be particularly noted that, in the unidirectional wave conditions, the off-diagonal elements are given by [65]:

$$\begin{cases} \bar{P}^{(*)}_{jk} = \dfrac{1}{2}\left(\bar{P}^{(*)}_{jj} + \bar{P}^{(*)}_{kk}\right) \\ \bar{Q}^{(*)}_{jk} = 0 \end{cases} \tag{2.17}$$

2.2 Irregular wave spectrum

In this work, the JONSWAP spectrum is used to model long-crested irregular waves, which can be expressed as [66]:

$$S(\omega) = \alpha_s H_s^2 \, \omega^{-5} \omega_p^{-4} \exp\left[-1.25\left(\frac{\omega}{\omega_p}\right)^{-4}\right] \gamma^{\exp\left[-\frac{(\omega-\omega_p)^2}{2\sigma^2\omega_p^2}\right]} \tag{2.18}$$

where α_s is the spectral parameter; H_s, ω_p and γ are the significant wave height, spectral peak period and enhancement factor, respectively; As $\omega < \omega_p$, the spectral parameter σ is equal to 0.07, while it is taken as 0.09 for $\omega \geq \omega_p$.

The stochastic WCI model can be obtained from the irregular wave spectrum and regular WCI model. Then, the long-crested irregular wave spectrum $S(\omega, u)$ with the current-induced modifications is formulated as [15]:

$$S(\omega, u) = \frac{4S(\omega)}{\left[1 + \frac{4\omega u}{g}\right]^{1/2} \left[1 + \left(1 + \frac{4\omega u}{g}\right)^{1/2}\right]^2} \tag{2.19}$$

where u refers to the current velocity, where positive and negative values represent the currents flowing along and opposite to the positive X-axis of the global coordinate system, respectively.

It is worth noting that an opposing current increases the amplitude and decreases the wavelength of wave components, resulting in steeper waves. Under sufficiently strong opposing currents, the wave steepness may reach the breaking limit ($\omega = -g/(4u)$), leading to wave breaking. Because Eq. (2.19) cannot account for the wave-breaking effects, it may overestimate the spectral densities at high frequencies. To overcome this limitation, an "equilibrium range limit" is adopted [16],

$$S_{ER}(\omega, u) = \frac{B^* g^2}{(\omega - k_c u)^5} \frac{1}{1 + \frac{2u(\omega - k_c u)}{g}} \tag{2.20}$$

where $B*$ is a Phillips constant [67]. It should be noted that the spectral value at any specific frequency is the minimum result from the calculations of Eqs. (2.19) and (2.20) [47]. In addition, the wave number in Eq. (2.20) is solved by the dispersion function in the presence of current [16],

$$\frac{(\omega - k_c u)^2}{g} = k_c \tanh(k_c h) \tag{2.21}$$

Based on the aforementioned wave spectrum model considering WCI, the wave elevation can be expressed as follows [18]:

$$\eta(x,t) = \sum_{j=1}^{N_w} A_j \cos(k_{cj}x - \omega_j t + \alpha_j) \tag{2.22}$$

where j denotes the index of wave component and α_j is a random phase angle uniformly distributed in $[0, 2\pi]$; N_w represents the total number of wave components. The amplitude of the j-th wave is calculated by the formula $A_j = \sqrt{2\,S(\omega_j, u)\,\Delta\omega}$, and $\Delta\omega$ is the frequency interval. Correspondingly, the resultant wave velocities in the horizontal and vertical directions are

$$u_w(x,z,t) = u + \sum_{j=1}^{N_w} A_j(\omega_j - uk_{cj}) \frac{\cosh[k_{cj}(z+h)]}{\sinh(k_{cj}h)} \cos(k_{cj}x - \omega_j t + \alpha_j) \tag{2.23}$$

$$v_w(x,z,t) = \sum_{j=1}^{N_w} A_j(\omega_j - uk_{cj}) \frac{\sinh[k_{cj}(z+h)]}{\sinh(k_{cj}h)} \sin(k_{cj}x - \omega_j t + \alpha_j) \tag{2.24}$$

More discussions and demonstrations on the wave elevation and velocity under the influence of the underlying currents can be found in [42].

For the short-crested irregular waves, they propagate along multiple directions. Therefore, a long-crested wave spectrum that takes into account both frequency and direction is used to model the short-crested wave [57],

$$S(\omega, \theta) = D(\theta)\,S(\omega) \tag{2.25}$$

where $D(\theta)$ represents the directionality function, which can be expressed as:

$$D(\theta) = C\cos^n(\theta - \bar{\theta}), \quad \text{for } -\frac{\pi}{2} \leq \theta - \bar{\theta} \leq \frac{\pi}{2} \tag{2.26}$$

where n is the spreading exponent; $\bar{\theta}$ is the mean wave direction. It should be noted that the integral of the short-crested wave spectrum over the range of wave directions is equal to that of the long-crested wave spectrum, demonstrating their wave energy is the same.

$$\int_{-\frac{\pi}{2}+\bar{\theta}}^{\frac{\pi}{2}+\bar{\theta}} S(\omega,\theta)\,d\theta = S(\omega) \tag{2.27}$$

Therefore, the value of C satisfies the following condition,

$$\int_{-\frac{\pi}{2}+\bar{\theta}}^{\frac{\pi}{2}+\bar{\theta}} D(\theta)\,d\theta = C\int_{-\frac{\pi}{2}+\bar{\theta}}^{\frac{\pi}{2}+\bar{\theta}} \cos^n(\theta-\bar{\theta})\,d\theta = 1 \tag{2.28}$$

For short-crested waves under WCI, the directional spectrum is constructed by combining the WCI-modified long-crested wave spectrum with the directional spreading function,

$$S^{\times}(\omega,\theta) = D(\theta)\,S^{\times}(\omega) \tag{2.29}$$

where $S^{\times}(\omega)$ represents the long-crested wave spectrum with the current-induced modifications, such as Eqs. (2.19) and (2.20).

In Eq. (2.29), the WCI-modified long-crested spectrum is used as the frequency-spectrum component, while the directional spreading function redistributes the wave energy over different propagation directions. Since the directional spreading function is normalised, the total wave energy of the short-crested wave spectrum remains consistent with that of the corresponding long-crested wave spectrum under the same current condition. This enables a controlled comparison between long-crested and short-crested wave cases.

It should be noted that this approach is an engineering approximation. In a fully direction-dependent WCI formulation, the influence of current would vary among different directional wave components because each component has a different relative angle with respect to the current direction. However, a generally applicable and validated spectral model with WCI effects for short-crested waves is not currently available for the present application. Therefore, the adopted formulation provides a practical way to include both WCI effects and directional spreading while maintaining energy consistency. The direction-dependent modification of each wave component by currents is acknowledged as a limitation and is recommended for future investigation.

2.3 Wave excitation forces in the time-domain

For irregular waves, the wave excitation forces include both first-order and second-order components. Short-crested waves consist of irregular waves from multiple incident directions, and each directional irregular wave is itself composed of multiple regular wave components. Therefore, under short-crested waves, the first-order and second-order wave forces exerted on the body can be expressed as, respectively [68]:

$$F_e^{(1)}(t) = \sum_{m=1}^{N_d} \sum_{j=1}^{N_w} A_{jm}\, \bar{F}^{(1)}(\omega_j, \theta_m) \cos(-\omega_j t + \alpha_{jm} + \beta_{jm}) \tag{2.30}$$

$$F_e^{(2)}(t) = \sum_{m=1}^{N_d} \sum_{n=1}^{N_d} \sum_{j=1}^{N_w} \sum_{k=1}^{N_w} A_{jm} A_{kn} \Big[\bar{P}_{jkmn}^{(*)}(\omega_j, \omega_k, \theta_m, \theta_n) \cos((\omega_j - \omega_k)t + (\alpha_{jm} - \alpha_{kn})) + \bar{Q}_{jkmn}^{(*)}(\omega_j, \omega_k, \theta_m, \theta_n) \sin((\omega_j - \omega_k)t + (\alpha_{jm} - \alpha_{kn})) \Big] \tag{2.31}$$

where N_d is the number of wave directions; β_{jm} is the phase of $\bar{F}^{(1)}(\omega_j, \theta_m)$; A_{jm} and A_{kn} are wave amplitudes; ω_{jm} and ω_{kn} are the incident frequencies; θ_m and θ_n are the incident angles; α_{jm} and α_{kn} are the random phases of the regular wave components, which are uniformly distributed in $[0, 2\pi]$; For A_{jm}, it can be expressed as [69]:

$$A_{jm} = \sqrt{2\, S^{*}(\omega_j, \theta_m)\, \Delta\omega\, \Delta\theta} \tag{2.32}$$

where $S^{*}(\omega, \theta)$ denotes the short-crested wave spectrum with WCI influence or without WCI influence.

In this work, the directional range of 180° centred around the mean incident wave direction is assumed to be uniformly divided into 20 intervals ($\Delta\theta$), resulting in 21 directional sub-spectra for the short-crested wave spectrum. Each of these sub-spectra is further discretised uniformly into 500 frequency intervals ($\Delta\omega$) over the range from 0.04 rad/s to 2.4 rad/s. To ensure the randomness of the irregular wave realisation, the frequency ω_j of the j-th wave component is randomly distributed within the j-th frequency interval [70]. Finally, the first- and second-order wave-force transfer functions obtained from the frequency-domain calculation are interpolated, which provides the second-order wave force induced by any pair of wave components under two arbitrary incident directions, as well as the first-order wave force induced by any wave component under one given incident direction.

As for long-crested waves, they consist of multiple regular wave components in a single incident direction. Therefore, based on Eqs. (2.30) and (2.31), the expressions for first-order and second-order wave forces under long-crested waves are as follows [71]:

$$F_e^{(1)}(t) = \sum_{j=1}^{N_w} A_j \bar{F}^{(1)}(\omega_j) \cos(-\omega_j t + \alpha_j + \beta_j) \tag{2.33}$$

$$F_e^{(2)}(t) = \sum_{j=1}^{N_w} \sum_{k=1}^{N_w} A_j A_k \Big[\bar{P}_{jk}^{(*)}(\omega_j, \omega_k) \cos((\omega_j - \omega_k)t + (\alpha_j - \alpha_k)) + \bar{Q}_{jk}^{(*)}(\omega_j, \omega_k) \sin((\omega_j - \omega_k)t + (\alpha_j - \alpha_k)) \Big] \tag{2.34}$$

where $A_j = \sqrt{2\, S^*(\omega_j)\, \Delta\omega}$, and $S^*(\omega)$ represents the long-crested wave spectrum with WCI influence or without WCI influence; β_j is the phase of $\bar{F}^{(1)}(\omega_j)$.

2.4 Lumped mass method

Mooring line dynamics are commonly simulated using three main approaches: the quasi-static method, the lumped-mass method, and the slender-rod method. The quasi-static method offers high computational efficiency, but it generally neglects the inertia and dynamic response of the mooring line [72]. In contrast, the slender-rod method can provide a more detailed representation of the continuous deformation and dynamic behaviour of the line, but this is achieved at the expense of greater modelling complexity and higher computational cost [73]. The lumped-mass method provides a practical compromise between these two approaches by discretizing the mooring line into a series of nodes and segments. This approach enables the main dynamic effects of the mooring line to be captured while maintaining relatively high computational efficiency [74].

Since this work focuses on the global dynamic response of the mooring system and its coupling with the platform motions, rather than local bending behaviour or cross-sectional structural response of the mooring line, the lumped-mass method proposed by Hall and Goupee [74] is adopted in this thesis to simulate the mooring line dynamics. In this approach, the continuous mooring line is discretized into N uniform segments and $N+1$ nodes. The mass assigned to each node is taken as half of the total mass of the two adjacent segments. By solving the equations of motion for each mass node, the mooring forces and dynamic response of the entire mooring line can be obtained. At each time step, the nodal states are updated to capture the global dynamic behavior of the mooring system. Let r_i and r_{i+1} denote the global position vectors of two adjacent mass nodes. The segment connecting these two nodes is denoted as segment $i+1/2$. The strain of segment $i+1/2$ is given by the following expression:

$$\varepsilon_{i+1/2} = \frac{|r_{i+1} - r_i|}{l} - 1 \tag{2.35}$$

where $|r_{i+1} - r_i|$ represents the current length of the segment, and l denotes the initial length of the segment.

The unit tangent vector of segment $i+1/2$ is given by:

$$\hat{q}_{i+1/2} = \frac{r_{i+1} - r_i}{|r_{i+1} - r_i|} \tag{2.36}$$

The tension in segment $i+1/2$ can be calculated as:

$$T_{i+1/2} = \frac{\pi d^2}{4} E_{i+1/2}\, \varepsilon_{i+1/2}\, \hat{q}_{i+1/2} \tag{2.37}$$

where $E_{i+1/2}$ is the Young's modulus of segment $i+1/2$, and d denotes the equivalent volume diameter. The tension exists only when the segment is in tension, acting in the direction from node i to node $i+1$; it vanishes when the segment is under compression.

The strain rate $\dot{\varepsilon}_{i+1/2}$ can be expressed as:

$$\dot{\varepsilon}_{i+1/2} = \frac{\partial \varepsilon_{i+1/2}}{\partial t} = \frac{\partial}{\partial t}\left(\frac{|r_{i+1} - r_i|}{l}\right) \tag{2.38}$$

To enhance numerical stability, an internal damping force is further introduced for this segment,

$$C_{i+\frac{1}{2}} = \frac{\pi}{4} d^2 C_{\text{int}} \dot{\varepsilon}_{i+\frac{1}{2}} \hat{q}_{i+\frac{1}{2}} = \frac{\pi}{8} d^2 C_{\text{int}} \left(\frac{r_{i+1} - r_i}{|r_{i+1} - r_i|^2}\right) \tag{2.39}$$

where C_{int} is the internal damping coefficient of the mooring line, with units of stress per unit strain rate.

The drag force and added mass acting on node i are calculated using the Morison equation [75]. The unit tangential vector at node i, defined between its two adjacent nodes, can be approximately expressed as:

$$\hat{q}_i = \frac{r_{i+1} - r_i}{|r_{i+1} - r_i|} \tag{2.40}$$

The transverse drag force component acting on mass node i is given by:

$$D_{p_i} = \frac{1}{2} \rho C_{dn} dl \left| (\dot{r}_i . \hat{q}_i)\hat{q}_i - \dot{r}_i \right| \left[(\dot{r}_i . \hat{q}_i)\hat{q}_i - \dot{r}_i \right] \tag{2.41}$$

where C_{dn} denotes the transverse drag coefficient. $\dot{r}_i$ represents the relative flow velocity at mooring node i under still-water condition. Similarly, the tangential drag force component at mass node i can be calculated as:

$$D_{q_i} = \frac{1}{2}\rho C_{dt} dl \left|(-\dot{r}_i.\hat{q}_i)\hat{q}_i\right| \left[(-\dot{r}_i.\hat{q}_i)\hat{q}_i\right] \tag{2.42}$$

where C_{dt} denotes the tangential drag coefficient.

The surrounding fluid around mass node i generates an added mass force a_i, which consists of both transverse and tangential components. It can be expressed as:

$$a_i = a_{p_i} + a_{q_i} = \frac{\pi}{4}\rho d^2 \left[C_{an}\left(I - \hat{q}_i\hat{q}_i^{\mathrm{T}}\right) + C_{at}\left(\hat{q}_i\hat{q}_i^{\mathrm{T}}\right)\right] \tag{2.43}$$

where C_{an} and C_{at} denote the transverse and tangential added mass coefficients, respectively; I represents the identity matrix.

When the mooring node interacts with the seabed, horizontal friction is neglected, and the vertical reaction force is transmitted through a linear spring-damper system, which can be expressed as:

$$B_i = dl\left[(z_{\mathrm{bot}} - z_i)k_b - \tilde{z}_i c_b\right]\hat{e}_z \tag{2.44}$$

where z_{bot} denotes the seabed elevation, while z_i and $\dot{z}_i$ represent the vertical position and velocity of the node, respectively; k_b is the seabed stiffness coefficient per unit area, c_b is the viscous damping coefficient per unit area, and $\hat{e}_z$ is the unit vector in the positive z-direction.

W_i denotes the submerged weight, i.e., the net buoyancy or weight acting on mass node i. The net buoyancy of segment i+1/2 is given by:

$$W_{i+\frac{1}{2}} = \frac{\pi}{4}d^2 l(p - \rho)g \tag{2.45}$$

where p is the density of mooring line.

Since this force is uniformly distributed between the two mass nodes, the vector form of the submerged weight W_i acting on mass node i is given by:

$$W_i = \frac{1}{2}\left(W_{i+\frac{1}{2}} + W_{i-\frac{1}{2}}\right)\hat{e}_z \tag{2.46}$$

Finally, the equation of motion for mass node i can be written as:

$$(m_i + a_i)\,\ddot{r}_i = T_{i+\frac{1}{2}} - T_{i-\frac{1}{2}} + C_{i+\frac{1}{2}} - C_{i-\frac{1}{2}} + W_i + B_i + D_{p_i} + D_{q_i} \tag{2.47}$$

where $m_i + a_i$ represents the sum of the mass and added mass; $T_{i+1/2} - T_{i-1/2} + C_{i+1/2} - C_{i-1/2}$ corresponds to the internal stiffness and damping forces; $W_i + B_i$ represents the weight and contact forces; $D_{pi} + D_{qi}$ denotes the drag forces.

2.5 Lagrange multiplier technique

For this wave-energy harvesting platform concept, the WEC array is rigidly mounted on the platform through hinged connections. For such a multi-body connected system, it can generally be modelled using methods such as the Newton–Euler method, Lagrange's equations, the Lagrange multiplier method, and Kane's method. The Newton–Euler method, Lagrange's equations, and Kane's method formulate the dynamic model of the system based on force equilibrium, energy relationship, and generalized velocity, respectively [76–78]. However, when applied to multi-body connected systems, these approaches often require relatively complex mechanical derivations. In contrast, the Lagrange multiplier method explicitly represents the connections between rigid bodies by introducing constraint equations, thereby enabling the dynamic model to be formulated in a more direct manner [79].

Owing to its simplicity in modelling the connections in multi-body systems, this thesis adopts the Lagrange multiplier method to establish the time-domain dynamic model of the wave-energy capture system. The core of the Lagrange multiplier method lies in enforcing displacement continuity for dynamic modelling, which can be realized by introducing the constraint matrix and the vector of hinge internal forces [80],

$$\begin{cases} D_j^{\mathrm{T}}\, F_{cj} = F_{rc}^{(p,q)} \\ D_j\, \xi^{(p,q)} = 0 \end{cases} \tag{2.48}$$

where D_j is the constraint matrix for the two connected floating bodies at the j-th hinge; F_{jc} is the internal force vector at the j-th hinge; $F_{rc}^{(p,q)}$ represents the reaction force vector acting on the two connected bodies at this hinge; $\xi^{(p,q)}$ is the displacement vector composed of the p-th and q-th bodies.

The constraint matrix D_j can be expressed as [81]:

$$D_j = A_j\,[L_p \;\; L_q] \tag{2.49}$$

where,

$$A_j = \begin{bmatrix} \cos\alpha^j & \sin\alpha^j & 0 & 0 & 0 & 0 \\ -\sin\alpha^j & \cos\alpha^j & 0 & 0 & 0 & 0 \\ 0 & 0 & 1 & 0 & 0 & 0 \\ 0 & 0 & 0 & \cos\alpha^j & \sin\alpha^j & 0 \\ 0 & 0 & 0 & 0 & 0 & 1 \end{bmatrix} \tag{2.50}$$

$$L_p = \begin{bmatrix} 1 & 0 & 0 & 0 & -(z_g^p - z_c^j) & (y_g^p - y_c^j) \\ 0 & 1 & 0 & (z_g^p - z_c^j) & 0 & -(x_g^p - x_c^j) \\ 0 & 0 & 1 & -(y_g^p - y_c^j) & (x_g^p - x_c^j) & 0 \\ 0 & 0 & 0 & 1 & 0 & 0 \\ 0 & 0 & 0 & 0 & 1 & 0 \\ 0 & 0 & 0 & 0 & 0 & 1 \end{bmatrix} \tag{2.51}$$

$$L_q = \begin{bmatrix} -1 & 0 & 0 & 0 & (z_g^q - z_c^j) & -(y_g^q - y_c^j) \\ 0 & -1 & 0 & -(z_g^q - z_c^j) & 0 & (x_g^q - x_c^j) \\ 0 & 0 & -1 & (y_g^q - y_c^j) & -(x_g^q - x_c^j) & 0 \\ 0 & 0 & 0 & -1 & 0 & 0 \\ 0 & 0 & 0 & 0 & -1 & 0 \\ 0 & 0 & 0 & 0 & 0 & -1 \end{bmatrix} \tag{2.52}$$

where A_j is the coordinate transformation matrix; α_j is the relative angle between the hinge rotational axis and the y-axis of global coordinate system; L_p and L_q are block matrices; (x_g^p, y_g^p, z_g^p) and (x_g^q, y_g^q, z_g^q) denote the center of mass coordinates of the p-th and q-th bodies, respectively; x_c^j, y_c^j, z_c^j represents the coordinates of the j-th hinge. More details on deriving the constraint matrix for multi-body connected system can be found in the literature [82].

2.6 A coupled hydro-connected-mooring dynamic model

Due to the hinge connectors in a multi-body floating system, the displacement continuity condition should be considered in its time-domain motion equation [83],

$$\begin{cases} \big[M_f + \mu(\infty)\big]_{6M\times 6M}\big[\ddot{\xi}(t)\big]_{6M\times 1} + \big[\int_0^t R(t-\tau)\dot{\xi}(\tau)\,d\tau\big]_{6M\times 1} \\ \qquad + \big[C_v + C_{\mathrm{PTO}}\big]_{6M\times 6M}\big[\dot{\xi}(t)\big]_{6M\times 1} + \big[K_h + K_{lock}\big]_{6M\times 6M}\big[\xi(t)\big]_{6M\times 1} \\ \qquad + [D]^{\mathrm{T}}_{6M\times m}\big[F_c(t)\big]_{m\times 1} = \big[F_e(t)\big]_{6M\times 1} + \big[F_m(t)\big]_{6M\times 1} + \big[F_d(t)\big]_{6M\times 1} \\ [D]_{m\times 6M}\big[\ddot{\xi}(t)\big]_{6M\times 1} = [0]_{m\times 1} \end{cases} \tag{2.53}$$

where M_f and $\mu(\infty)$ are the mass and added mass matrix at infinite frequency, respectively; C_v and C_{PTO} refer to the linearized viscous damping and PTO damping matrices, respectively; K_h is the hydrostatic stiffness matrix; $F_e(t)$ and $F_d(t)$ are the wave excitation force and current drag force, respectively; $F_m(t)$ is the mooring force, which can be solved by the lumped mass method; $F_c(t)$ are the internal forces of the hinge connectors, and D refers to the constraint matrix; m=5(M-1) denotes the number of DoFs constrained. It is worth noting that, under severe sea states, the WECs should be locked to remain stationary relative to the platform, thereby preventing damage to the PTO system. In the numerical simulation, this locking condition is realized by introducing a stiffness matrix K_{lock}. As for the retardation function matrix $R(t)$, which represents the fluid memory effects, it can be expressed as [84]:

$$R(t) = \frac{2}{\pi} \int_0^{\infty} \lambda(\omega) \cos(\omega t) \, d\omega \tag{2.54}$$

The drag force of the current can be generally expressed as [85]:

$$F_{dj}(\theta) = C_{dj}(\theta) \, |u_r| \, u_r, \quad j = 1 \sim 6 \tag{2.55}$$

where $C_{dj}(\theta)$ denotes the current coefficient corresponding to the relative heading angle θ between the current incident direction and the integrated system; u_r is the relative current velocity along the incident direction. Generally, the current coefficients can be obtained through model tests, CFD simulations, or empirical formulas. For example, under a known relative heading angle θ_k and current velocity u, if the forces and moments at the center of mass ($k = 1 \sim 6$) are obtained via experiments, CFD, or empirical methods, the drag coefficient for that specific heading angle can then be derived as [65]:

$$C_{dj}(\theta_k) = \frac{F_{dj}(\theta_k)}{u^2} \tag{2.56}$$

Regarding the derivations of C_{PTO} and K_{lock}, a reference is provided by describing the PTO damping and locking stiffness matrices associated with the j-th WEC and the platform at the corresponding hinge,

$$\begin{bmatrix} C_{gj} & -C_{gj} \\ -C_{gj} & C_{gj} \end{bmatrix} = T_{ej}^{\mathrm{T}} \begin{bmatrix} C_{lj} & -C_{lj} \\ -C_{lj} & C_{lj} \end{bmatrix} T_{ej} \tag{2.57}$$

$$\begin{bmatrix} K_{gj} & -K_{gj} \\ -K_{gj} & K_{gj} \end{bmatrix} = T_{ej}^{\mathrm{T}} \begin{bmatrix} K_{lj} & -K_{lj} \\ -K_{lj} & K_{lj} \end{bmatrix} T_{ej} \tag{2.58}$$

where C_{lj} and K_{lj} are the PTO damping and locking stiffness matrices imposed at the j-th hinge; C_{gj} and K_{gj} represent the PTO damping and locking stiffness matrices in the global coordinate systems; T_{ej} is the element transformation matrix for the j-th hinge. The matrices C_{lj}, K_{lj} and T_{ej} can be expressed as, respectively:

$$C_{lj} = \begin{bmatrix} 0 & 0 & 0 & 0 & 0 & 0 \\ 0 & 0 & 0 & 0 & 0 & 0 \\ 0 & 0 & 0 & 0 & 0 & 0 \\ 0 & 0 & 0 & 0 & 0 & 0 \\ 0 & 0 & 0 & 0 & c_{pj} & 0 \\ 0 & 0 & 0 & 0 & 0 & 0 \end{bmatrix} \tag{2.59}$$

$$K_{lj} = \begin{bmatrix} 0 & 0 & 0 & 0 & 0 & 0 \\ 0 & 0 & 0 & 0 & 0 & 0 \\ 0 & 0 & 0 & 0 & 0 & 0 \\ 0 & 0 & 0 & 0 & 0 & 0 \\ 0 & 0 & 0 & 0 & k_{pj} & 0 \\ 0 & 0 & 0 & 0 & 0 & 0 \end{bmatrix} \tag{2.60}$$

$$T_{ej} = \begin{bmatrix} d_{ej} & 0 & 0 & 0 \\ 0 & d_{ej} & 0 & 0 \\ 0 & 0 & d_{ej} & 0 \\ 0 & 0 & 0 & d_{ej} \end{bmatrix} \tag{2.61}$$

where c_{pj} is the PTO damping coefficient imposed at the j-th hinge; k_{pj} is the PTO locking stiffness coefficient imposed at the j-th hinge, which is assigned a sufficiently large value; d_{ej} is the direction cosine matrix of the j-th hinge local coordinate system relative to the global coordinate system [86],

$$d_{ej} = \begin{bmatrix} \cos(X_j'X) & \cos(X_j'Y) & \cos(X_j'Z) \\ \cos(Y_j'X) & \cos(Y_j'Y) & \cos(Y_j'Z) \\ \cos(Z_j'X) & \cos(Z_j'Y) & \cos(Z_j'Z) \end{bmatrix} \tag{2.62}$$

where $O - X_j'Y_j'Z_j'$ denotes the local coordinate system of the j-th hinge.

Figure 2.2 presents the flowchart of numerical simulation of the coupled dynamic model. First, the hydrodynamic coefficients of the integrated system are obtained from frequency-domain calculation using the potential-flow software AQWA. These coefficients are then transferred to the time-domain simulations as external load inputs, which are implemented in MATLAB. In addition to the hydrodynamic loads, the external loads also include the current drag force, PTO damping force and PTO locking force. The mooring system is simulated using the open-source module MoorDyn, which is developed based on the lumped-mass method. The hinged constraints within the integrated system are modeled using the Lagrange multiplier method. It should be noted that, after combining the Cummins equation with the constraint equation, the resulting governing equations form a second-order differential–algebraic equation (DAE) system, which can be solved using the fourth-order Runge–Kutta method. MoorDyn solves the mooring line dynamics using a second-order Runge–Kutta scheme. It is worth noting that the coupling between the motion equation of the integrated system and the mooring equation is implemented using a loosely coupled strategy [74].

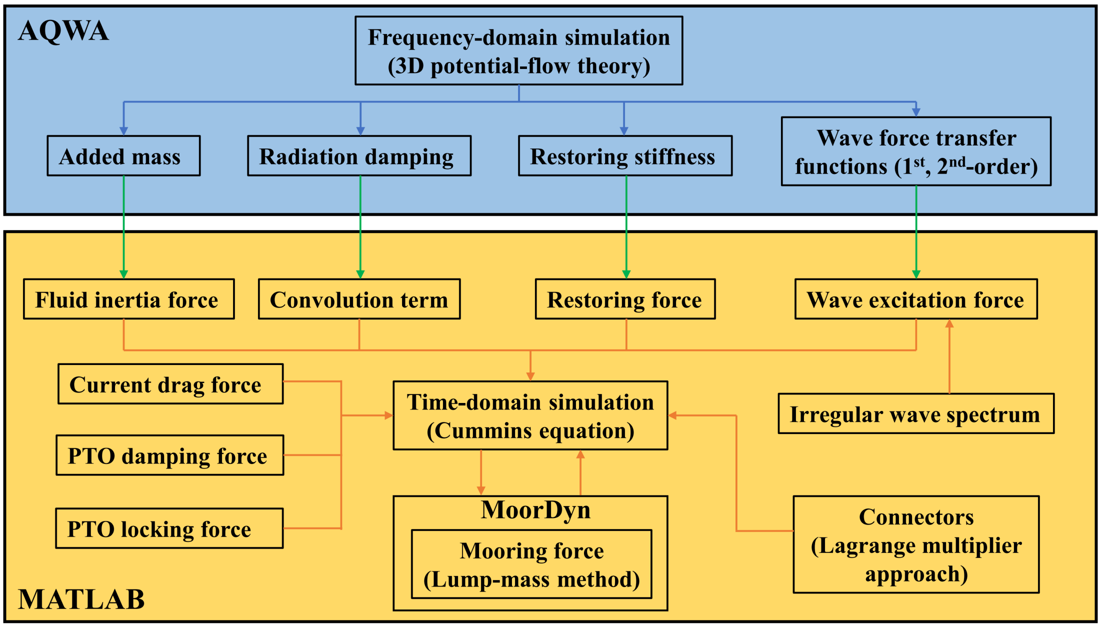

Figure 2.3: Flowchart of numerical simulation of the coupled dynamic model.

2.7 Captured power of the individual WEC

By solving Eq. (2.53), the PTO damping force acting on the integrated system can be obtained.

$$[C_{\mathrm{PTO}}]_{6M\times 6M}\left[\dot{\xi}(t)\right]_{6M\times 1}=[F_{\mathrm{PTO}}(t)]_{6M\times 1} \tag{2.63}$$

Accordingly, the PTO damping force acting on the j-th WEC related to its local hinged coordinate system can be expressed as:

$$F_{\mathrm{PTO},h}^{(j)}(t)=\sqrt{\left(F_{\mathrm{PTO},4}^{(j)}(t)\right)^2+\left(F_{\mathrm{PTO},5}^{(j)}(t)\right)^2} \tag{2.64}$$

where $F_{\mathrm{PTO},4}^{(j)}$ and $F_{\mathrm{PTO},5}^{(j)}$ denote the PTO damping force components acting on the j-th WEC in the roll and pitch DoFs, respectively.

Finally, the average power captured by the j-th WEC over a time interval T

can be formulated as [87]:

$$P_w^{(j)} = \frac{1}{T}\int_t^{t+T} \frac{\left[F_{\mathrm{PTO},h}^{(j)}(t)\right]^2}{c_{pj}}\,dt \tag{2.65}$$

Chapter 3

The floating wave-energy harvesting platform in short-crested irregular waves

The primary objective of this chapter is to investigate the dynamic behavior of the wave-energy harvesting platform under short-crested irregular wave conditions. To ensure the reliability of the numerical analysis, a mesh convergence study was first carried out for the hydrodynamic models of both the platform and the WEC, followed by damping corrections for the hydrodynamic models. Furthermore, to verify the developed coupled dynamic model and the short-crested wave spectrum, this chapter compares the response results obtained from the developed numerical model with those predicted by AQWA. Finally, time-domain simulations using the proposed dynamic model are adopted to evaluate the effects of wave directionality on the platform motion, mooring line tension, and power absorption of the WECs. The results show that the wave directionality has a significant influence on the dynamic response and power capture of the wave-energy capture platform. Since short-crested waves are commonly encountered in marine environments, it is recommended that the wave directional distribution be considered in the design and performance assessment of this type of offshore structures.

3.1 Viscous corrections for the hydrodynamic models

Before the viscous corrections, the mesh convergence of the hydrodynamic models needs to be verified. In this thesis, the wetted surfaces of the platform and WEC are discretized into 14000 and 2640 panel elements, respectively. There are two methods calculating the steady drift forces in AQWA, namely, the near-field and the far-field methods. By comparing the steady drift force results with these two methods, it can be determined whether the mesh discretization reaches convergence [53]. Figure 3.1 illustrates the surge steady drift forces of the platform and WEC. It can be inferred from the figure that the results with the two methods agree well.

Figure 3.2 shows the physical model of the platform [88]. Cao et al. [89] obtained the damping ratios of the six DoFs through the experimental tests. Based on these damping ratios, the viscous damping of the platform is considered in its hydrodynamic model. The platform response amplitude operators (RAOs) were measured by Cao et al. [88] under the white noise test. The RAOs could be obtained from the measured motion response and wave spectra. The white noise wave has a significant wave height of 5 m and a spectral peak period ranging from

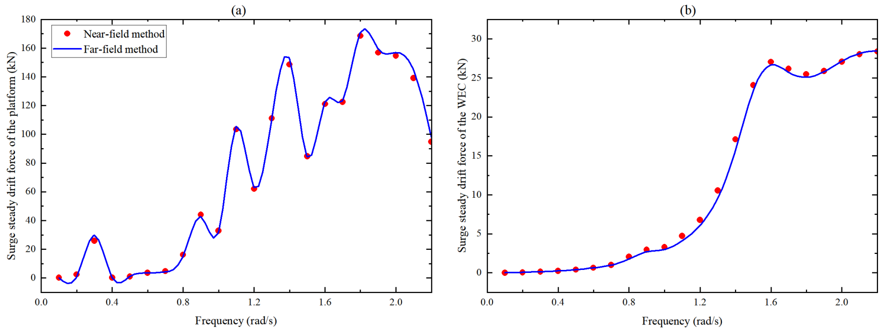

Figure 3.1: Comparison of the surge steady drift forces of the platform and WEC with near-field and far-field methods.

5 to 20 s. After the viscous correction for the platform, this work adopts the time-domain simulations to obtain the RAO results. A comparison of the numerical and experimental RAOs for the platform motions is presented in Figure 3.3. From the figure, it can be observed that the numerical and experimental results agree well.

Figure 3.2: Illustration of the physical model of the platform [88].

Figure 3.4 illustrates the physical model of the WEC [90]. He et al. [90] conducted the experimental studies on the heave DoF. In their work, the heave RAOs of the WEC floater were tested at four specific frequencies. Zhou et al. [91] found that the effects of viscous damping on the response of WEC buoy are much less pronounced than those of radiation damping when its diameter-to-draft ratio is large. However, to ensure an accurate estimate, 6% critical damping is still

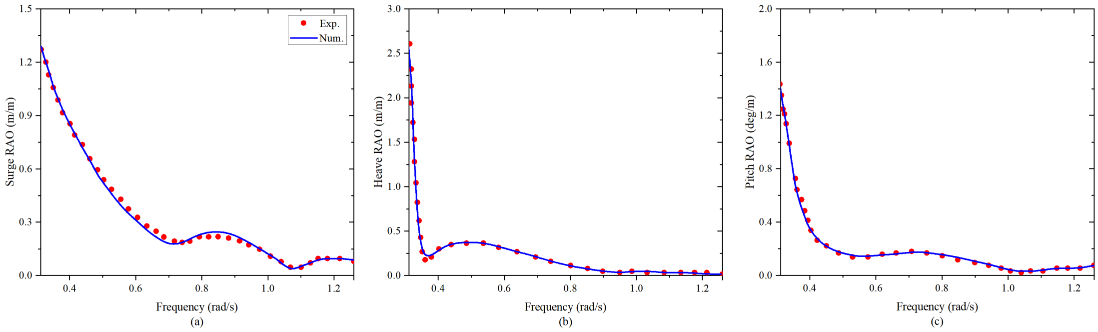

Figure 3.3: Comparison of the motion RAOs of the platform between the numerical and experimental results.

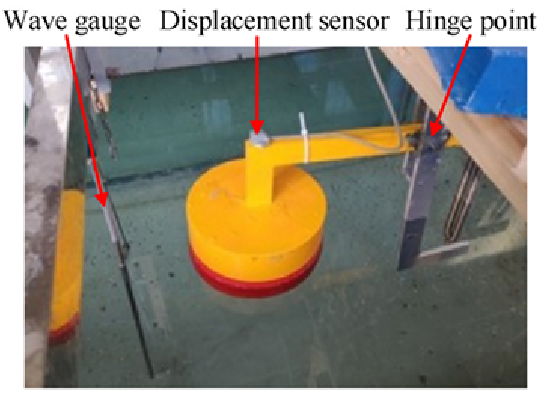

Figure 3.4: Schematic diagram of the physical model of the WEC [90].

introduced for viscous correction in the heave DoF [92]. It should be noted that there is no PTO damping at the hinge point. Figure 3.5 shows the heave RAOs of the WEC from both experimental and numerical studies. As seen in the figure, the numerical results agree with the experimental data well.

3.2 Verifications of the coupled dynamic model and the short-crested wave-spectrum model

To ensure the reliability of all the studies presented in this thesis, the coupled hydrodynamic–connected–mooring dynamic model is verified in this section. Mean-

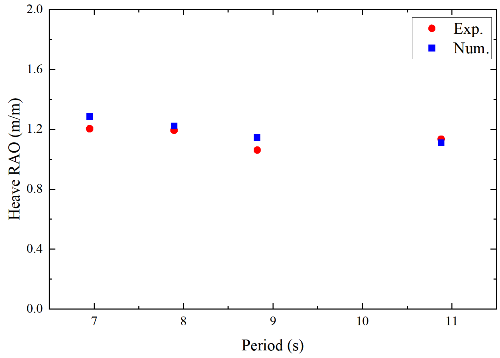

Figure 3.5: Comparison of the heave RAOs of the WEC between the numerical and experimental results.

while, as the focus of this chapter is to investigate the wave-energy capture platform under short-crested wave conditions, the short-crested irregular wave spectrum model introduced in Chapter 2 also requires verification. It is worth noting that AQWA provides the function to simulate short-crested waves [66], with a wave-spectrum model that is consistent with that introduced in this thesis.

The wave-energy capture platform is modelled separately in AQWA and in the developed model. The dynamic responses and captured power of this system under short-crested wave condition are then calculated using these two numerical tools. The parameters of the short-crested wave are specified as follows: the significant wave height is 3.8 m, the spectral peak period is 8.3 s, the enhancement factor is 2.4, the spreading exponent is 2, and the mean incident direction is 0°. Figure 3.6 presents the surge, heave, and pitch responses of the platform, while Figure 3.7 shows the tension response of #5 and the power captured by WEC 1. It can be observed from these figures that the results obtained using the two numerical tools are generally in good agreement. Therefore, the dynamic model developed in this thesis, together with the adopted short-crested wave-spectrum model, is demonstrated to be accurate for the subsequent studies.

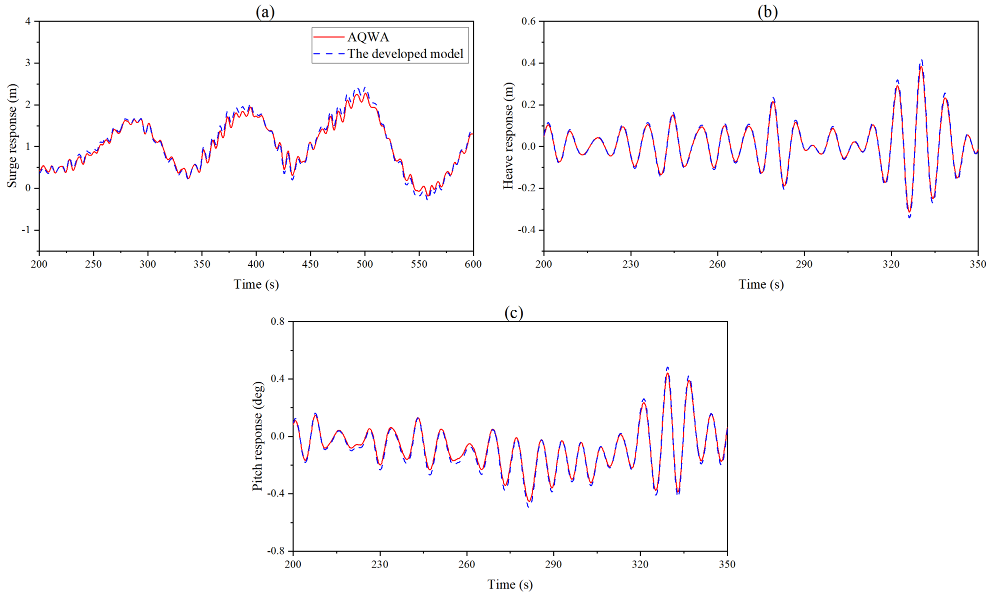

Figure 3.6: Comparison of the platform motions under short-crested wave condition using AQWA and the developed model.

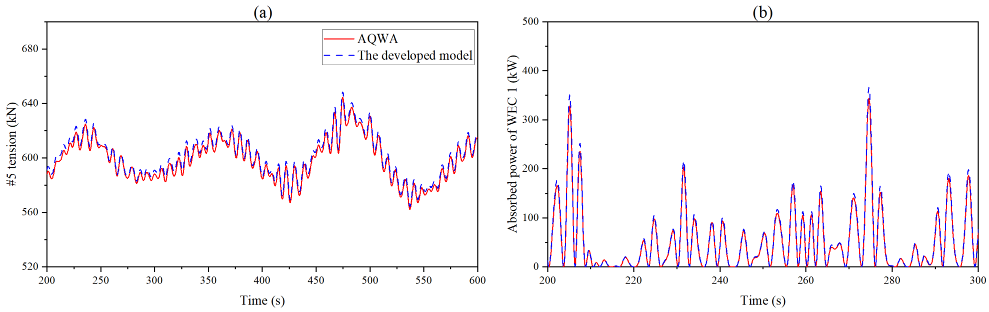

Figure 3.7: Comparison of #5 tension and absorbed power of WEC 1 under short-crested wave condition using AQWA and the developed model.

3.3 Results and discussion

This section focuses on the dynamic responses and power capture characteristics of the wave-energy capture platform under short-crested wave conditions. The operating site is assumed to be located 20 km offshore in the north of the South China Sea. Five design environmental conditions (ECs) are reported for this site in the previous work of Cao et al [93]. It's assumed that there are no wind and current loads, and only the irregular waves are considered in this study. Table 3.1 lists the parameters of EC1-EC5, where EC1-EC3 represent operational conditions, and EC4-EC5 denote severe conditions.

Table 3.1: Five ECs.

	H_s(m)	T_p(s)	γ
EC1	2.0	6.2	2.0
EC2	3.8	8.3	2.4
EC3	6.8	10.1	3.7
EC4	8.1	11.4	3.1
EC5	10.3	14.1	2.0

Cao et al. [93] conducted a dynamic response analysis of the SPIC semi-submersible platform under long-crested wave conditions for the aforementioned five ECs. However, multidirectional wave propagation is commonly observed in real marine environments, and short-crested waves exhibit markedly different characteristics from long-crested waves. Therefore, it is meaningful to further investigate the effects of wave distribution on the dynamic responses and energy capture features of the wave-energy harvesting platform, for the design and engineering application of this type of offshore structure.

Although directional wave spectra for this site are not available, different spreading exponents ($n = 2 - 8$) are introduced to represent various degrees of directional spreading. Meanwhile, it's assumed that the mean incident wave direction is 0°.

In the time-domain simulations, the total simulation duration is set to 4100 s. The Cummins motion equation is solved using a time step of 0.1 s, whereas a smaller time step of 0.01 s is adopted for solving the mooring dynamic equations. Furthermore, to eliminate the influence of initial transient responses, the first 500 s of the time history from each simulation are excluded.

3.3.1 Characteristics of short-crested wave conditions

To characterize the short-crested waves, this section introduces the 2D wave spectra of EC2 for various spreading exponents, as shown in Figure 3.8. As demonstrated in the figure, the spectral value of the wave spectrum is maximal at the spectral peak frequency. In addition, it can be inferred that a larger spreading component indicates less energy is focused around the peripheral direction, and more around the dominant direction. Furthermore, since the total energy of the wave spectrum remains constant, the spectral value around the dominant direction increases as the spreading exponent becomes larger.

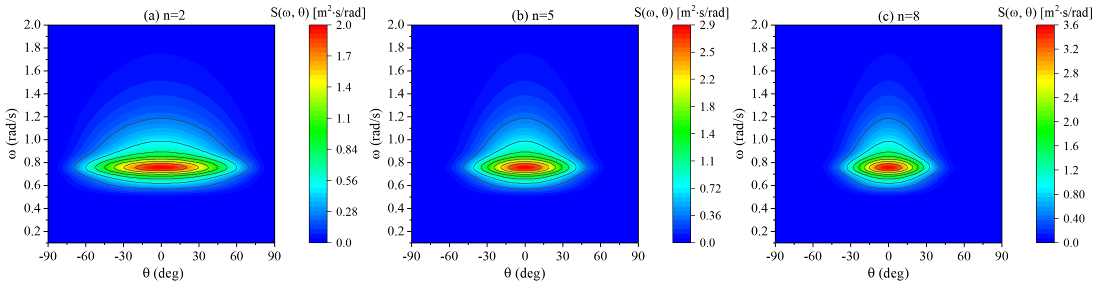

Figure 3.8: 2D wave spectra of EC2 with various spreading exponents.

3.3.2 Determination of PTO damping coefficients

Based on the layout of the WEC array, all WECs have only two distinct relative angles with respect to the mean wave incident direction. The WECs with the same relative angle are classified into the same group. Accordingly, the WECs in Row 3 are assigned to another group, denoted as Group A, while the WECs in Rows 1 and 2 are assigned to another group, denoted as Group B. In addition, it's assumed that all WECs within each group have the same PTO damping coefficient.

WEC-A and WEC-B are defined to represent the WECS in Groups A and B, respectively. To determine the PTO damping coefficients that maximize the absorbed power of WEC-A and WEC-B, namely the optimal damping coefficients, a parametric analysis is conducted under EC1-EC3 with different spreading exponents.

Figure 3.9 presents the absorbed power of WEC-A with various PTO damping coefficients. In this figure, it can be observed that under EC1-EC3, WEC-A absorbs the most power at the PTO damping coefficients of 2.5×10^4 kN.m.s/rad, 4.6×10^4 kN.m.s/rad and 6.7×10^4 kN.m.s/rad, respectively. In addition, it can be found that under EC1, the variation pattern of the absorbed power regarding the spreading component is different from those under other two ECs. The absorbed power exhibits a decreasing trend across the spreading exponents under EC1, but it shows an opposite trend under the other two ECs.

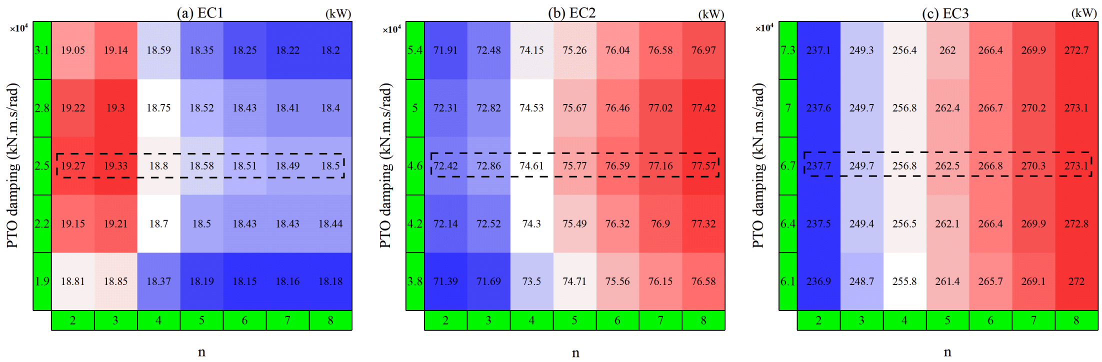

Figure 3.9: Absorbed power of WEC-A for various spreading exponents versus different PTO damping coefficients under three operational ECs.

Figure 3.10 shows the absorbed power of WEC-B with various PTO damping coefficients. It can be seen in this figure that under EC1-EC3, the absorbed power of WEC-B reaches maximal at the PTO coefficients of 2.5×10^4 kN.m.s/rad, 4.4×10^4 kN.m.s/rad and 6.7×10^4 kN.m.s/rad, respectively. In addition, the absorbed power shows a decreasing trend across the spreading components under EC1-EC3. It is noteworthy that under the identical EC, WEC-B absorbs more power than WEC-A.

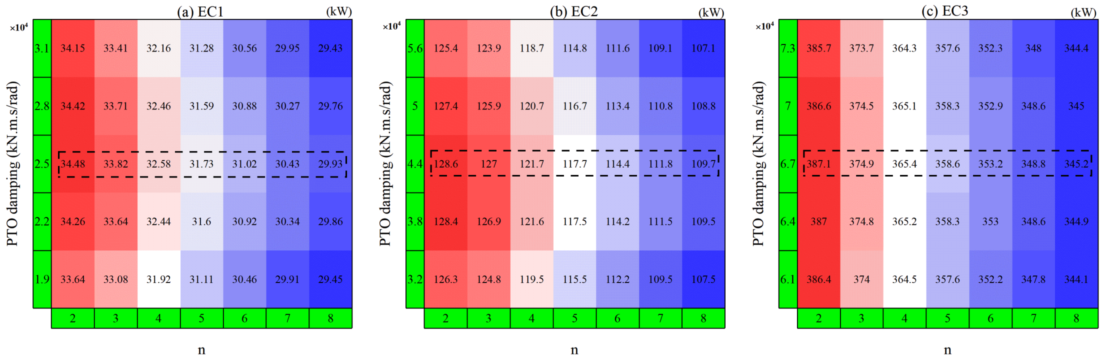

Figure 3.10: Absorbed power of WEC-B for various spreading exponents versus different PTO damping coefficients under three operational ECs.

In the subsequent analysis, under EC1-EC3, the PTO damping coefficients of the WECs in Rows 1 and 2 are set to the optimal damping coefficients of WEC-B, whereas those of the WECs in Row 3 are set to the optimal damping coefficients of WEC-A.

3.3.3 Platform motion response

To analyze the platform motions under short-crested wave conditions, the mean values and standard deviations (STDs) of the surge, heave, and pitch responses are presented in this section, as shown in Figures 3.11-3.13.

From Figure 3.11(a), it can be observed that under EC1, the mean surge value remains nearly constant under different spreading exponents, which implies that the wave directionality hardly changes the equilibrium position of the platform in the surge direction. However, as n=2, the surge response has a smaller STD compared to a larger spreading component, which is due to the fact that for n=2, the scattered wave distribution is unable to stimulate a larger motion in the surge direction.

As seen in Figures 3.11(b)-3.11(e), under EC2-EC5, the mean surge value shows a slight increasing trend across the spreading component, which indicates the differences in the mean drift force caused by variations in the spreading exponent are large enough to affect its equilibrium position. In addition, under EC5, the variation pattern of the surge STD regarding the spreading component is different from that under EC2-EC4. Under EC2-EC4, the short-crested waves with larger spreading exponents can excite a larger surge slow-drift force , which leads to a more intense surge response. As a result, the surge STD has an increasing trend across the spreading component. However, under EC5, the surge STD decreases as the spreading component increases. This may be attributed to the fact that the restraning effect of the mooring system outweighs the excitation effect of the surge slow-drift force.

In Figure 3.12(a), it can be observed that there is a obvious jump from n=3 to n=4 in the mean response of the heave motion under EC1, and it remains constant when $n > 3$. This indicates that as the spreading component exceeds a certain threshold, the constraint forces at the hinges are sufficiently large to push the platform upward from its initial heave equilibrium position. In addition, the heave STD increases as the spreading exponent increases. This is due to the fact that the short-crested waves with more focused distribution excites a larger heave oscillation.

As shown in Figure 3.12(b), under EC2, the mean value and STD of the heave response for n=2 are similar to those for n=8, but smaller than those for n=3-7. This may be attributed to the fact that the phase differences among the hinge

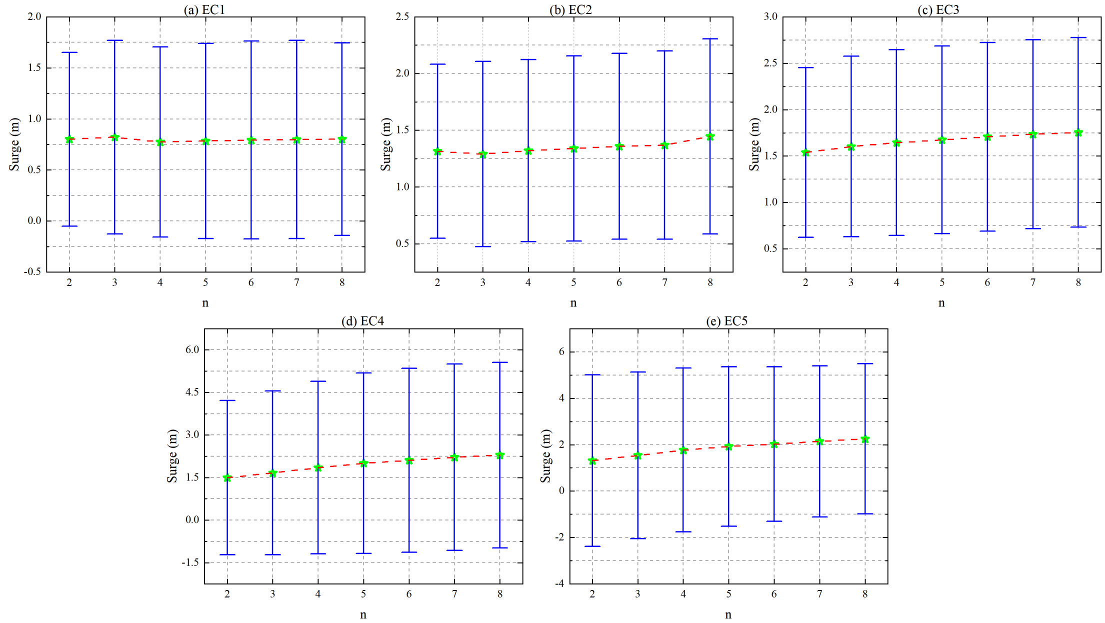

Figure 3.11: Surge mean value and STD of the platform for various spreading exponents under five ECs.

constraint forces lead to a relatively small upward excitation, when the wave distribution is significantly scattered or focused.

It can be found from Figures 3.12(c)-3.12(e) that under EC3-EC5, the variation patterns of the mean value or STD of the heave response regarding the spreading component are similar. For the mean value, it remains almost constant for different spreading components. This means that the differences in wave excitation caused by variations in wave directional spreading are insufficient to alter the heave equilibrium position. As for the STD, it has an upward trend across the spreading component, which is due to the fact that the more focused the wave distribution is, the more intense the heave response is.

It is worth noting from Figure 3.13 that the variation pattern of the pitch STD across the spreading component under EC1 is similar to that of the surge STD (as shown in Figure 3.11(a)). This phenomenon is attributed to the coupling

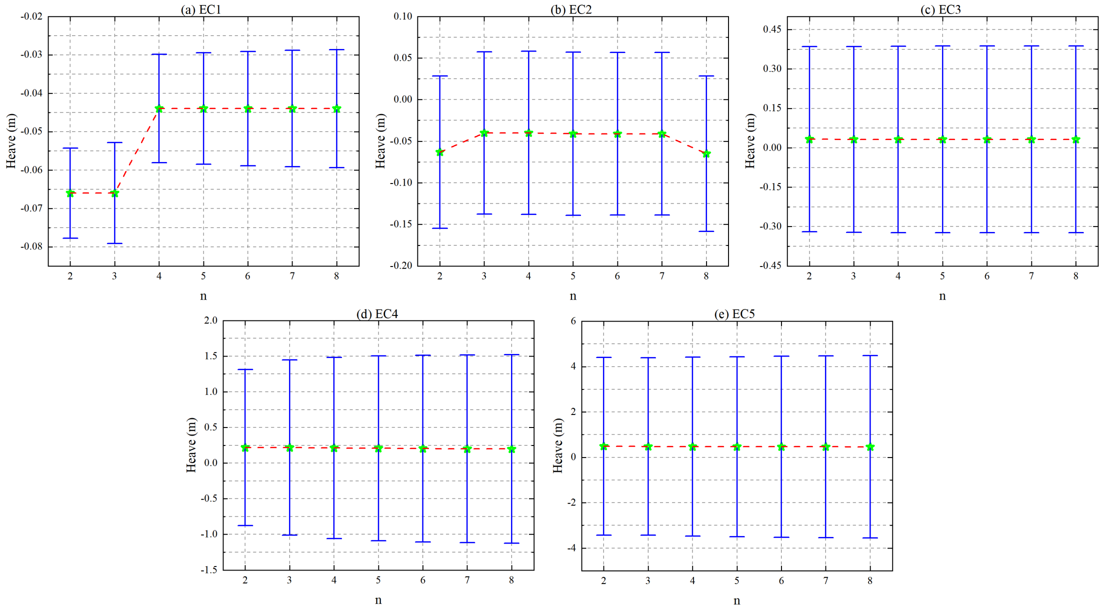

Figure 3.12: Heave mean response and STD of the platform for various spreading exponents under five ECs.

effects between the surge and pitch motions. In addition, the variation trends of the pitch mean value under EC1, and the pitch mean value and STD across the spreading component under EC2-EC5 are similar to those of the heave response. This indicates that the coupling effects between the heave and pitch motions are significant.

3.3.4 Mooring line tension

To analyze the dynamic response of the mooring line under short-crested wave conditions, Figure 3.14 shows the mean value and STD of the #5 tension response. The reason for selecting #5 as the object is that its tension response is maximal under this mean wave incidence direction, which is crucial for assessing the safety of the mooring system.

From Figures 3.14(a)-3.14(c), it can be observed that under EC1-EC3, the

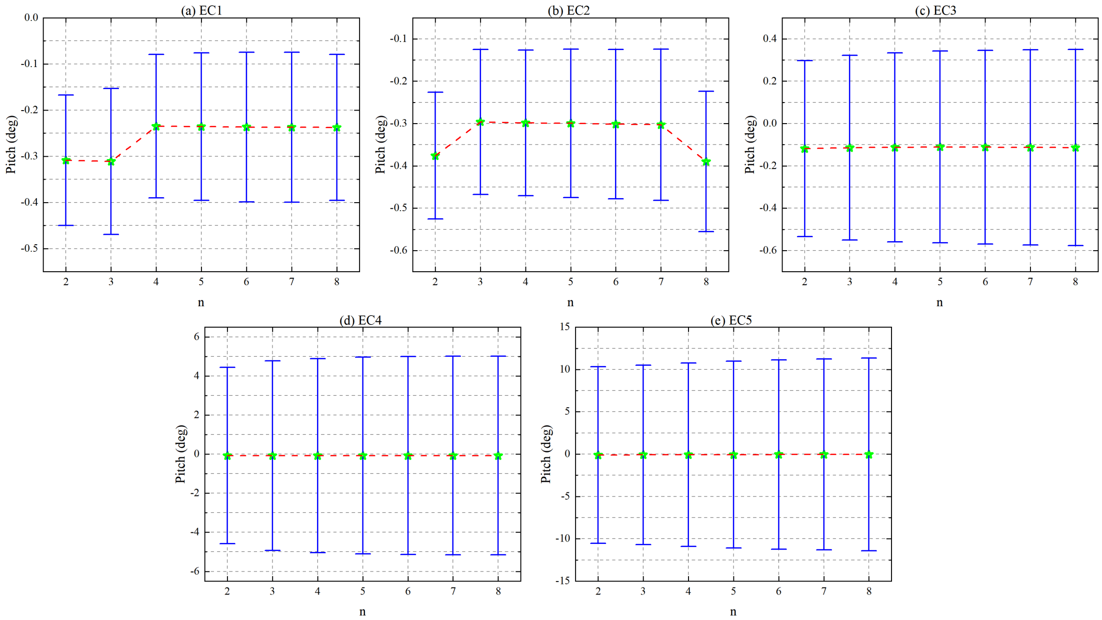

Figure 3.13: Pitch mean response and STD of the platform for various spreading exponents under five ECs.

tension mean response remains almost constant regarding the spreading component. This is due to the fact that although the longitudinal equilibrium position of the platform varies for different spreading components, it is not able to make a significant change in the average suspended length of #5 in the water. For the tension STD, it can be found in Figure 3.14(a) that it is maximal for n=3 and minimum for n=8. This implies that the tension oscillation is more intense as the wave directionality is relatively scattered. However, a different situation occurs in Figure 3.14(b), which is that the tension STD reaches maximal for n=8. This indicates that under EC2, the tension can be excited with a more intense response under a short-crested wave with more focused energy. From Figure 3.14(c), it can be seen that there is a decreasing trend in the tension STD from n=5 to n=8 under EC3. This reflects that the more focused the wave distribution is, the weaker the tension oscillation is.

As seen in Figures 3.14(d)-3.14(e), under EC4-EC5, the mean value and STD of the tension response show an overall decreasing trend across the spreading component. This can be attributed to the fact that the arrangement of #5 is more aligned with the direction perpendicular to the mean incident wave direction. Consequently, a broader wave distribution is more likely to induce a larger tension response of #5.

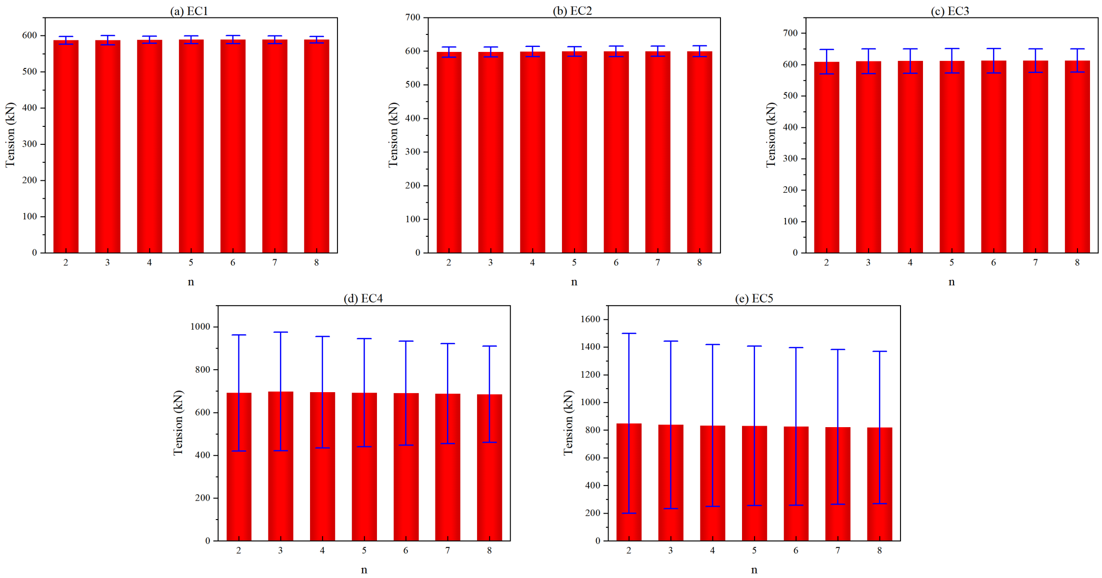

Figure 3.14: The mean value and STD of #5 tension response for various spreading exponents under five ECs.

3.3.5 Power capture performance

To investigate the power capture performance of point-absorber WECs under short-crested wave conditions, this section analyzes the power absorption of the individual WEC, WEC row, and WEC array in the following studies. In addition, the effects of multi-body hydrodynamic interactions and the platform motions on power capture are also demonstrated. Since the wave-energy capture platform is symmetric about the mean wave incidence direction, only five individual WECs (WECs 1-3, WEC 7, and WEC 8) are considered, while only two rows of WECs, Rows 1 and 3, are investigated. It is worth noting that, in order to evaluate the effects of the hydrodynamic interactions and platform motion on the wave energy conversion, another three scenarios are set up as "Single WEC", "Wave farm", "Wave-energy capture system (fixed)". For the convenience of subsequent studies, these four scenarios are defined as Scenarios 1-4, respectively. Scenario 1 corresponds to the individual WECs, Scenario 2 represents the WEC array, Scenario 3 is the fixed wave-energy capture platform, and Scenario 4 refers to the floating wave-energy capture platform.

The individual WEC

Figure 3.15 demonstrates the mean absorbed power of the individual WECs among four scenarios for various spreading components under EC1.

The influence of the wave distribution on the power capture performance of the individual WECs is first investigated. From Figures 3.15(a)-3.15(b), it can be observed that the absorbed power of WECs 1 and 2 decreases as the spreading exponent increases. This can be attributed to the fact that the layouts of WECs 1 and 2 are more aligned with the direction perpendicular to the mean incident wave direction. As a result, a more focused wave distribution tends to reduce their vertical responses relative to the hinges.

It can be found from Figure 3.15(c) that the variation pattern of the absorbed power of WEC 3 regarding the spreading component is consistent among the latter three scenarios, and WEC 3 absorbs the most power for n=3. As the spreading exponent gradually increases, the power absorbed by WEC 3 no longer exhibits significant variations.

From Figure 3.15(d), it can be seen that among all scenarios, WEC 7 absorbs the most power for the intermediate spreading exponents. The absorbed power exhibits an first increasing and then decreasing trend across the spreading component. This indicates that both excessively focused and scattered wave distributions cannot induce large vertical response of WEC 7 relative to the hinge.

it can be noticed in Figure 3.15(e) that among the latter three scenarios, the absorbed power of WEC 8 has an increasing trend across the spreading component. However, starting from $n = 6$, the power absorbed by WEC 8 shows no significant increase with further increase in the spreading exponent. This may be attributed to the fact that the wave distribution at $n = 6$ is already sufficient to induce its near-maximum vertical response relative to the hinge, such that further increase in the spreading exponent have only a limited influence.

The effects of hydrodynamic interactions and platform motion on the power capture of individual WECs are then explored. It can be observed from Figure 3.15(a) that the absorbed power of WEC 1 gradually decreases from Scenario 1 to Scenario 4. This phenomenon demonstrates that the hydrodynamic interactions have an adverse influence on the power capture of WEC 1.

From Figure 3.15(b), it can be found that WEC 2 absorbs the most power among Scenario 1 and the least among Scenario 2. Meanwhile, the power captured by WEC 2 among Scenario 3 is more than that among Scenario 4. These phenomena indicate that although the hydrodynamic interactions within the WEC array have an adverse impact on the power capture of WEC 2, the hydrodynamic interference induced by the platform can partially improve its power absorption.

As seen in Figure 3.15(c), the captured power of WEC 3 gradually decreases among the latter three scenarios. In addition, the performance of WEC 3 among Scenario 1 experiences from the best to the worst as the spreading exponent increases, which implies that the more focused the wave distribution is, the more significant the impact of hydrodynamic interactions has on enhancing power absorption of WEC 3.

It can be observed from Figure 3.15(d) that the power absorbed by WEC 7 among the latter three scenarios is much larger than that among Scenario 1. Meanwhile, WEC 7 exhibits the best and the worst performance among Scenarios 3 and 4, respectively. This suggests that the hydrodynamic interference induced by the platform enhances the performance of WEC 7, while the platform motion has the adverse effects on its power capture.

In Figure 3.15(e), the performance of WEC 8 among Scenario 1 gradually transitions from being much better to being slightly weaker than that among Scenario 2 as the spreading component increases. This suggests that the hydrodynamic interactions within the WEC array can enhance the power absorption of WEC 8 as the wave distribution becomes focused. In addition, for large spreading exponent, WEC 8 absorbs more power among Scenario 4 than among Scenario 3, while its captured power among Scenarios 1 and 2 is significantly lower than that under Scenarios 3 and 4. These phenomena demonstrate that the presence of platform can improve the power capture of WEC 8 under focused wave distribution.

To quantify the influence of multi-body hydrodynamic interactions and platform motion on the power capture of the individual WECs, an influence factor

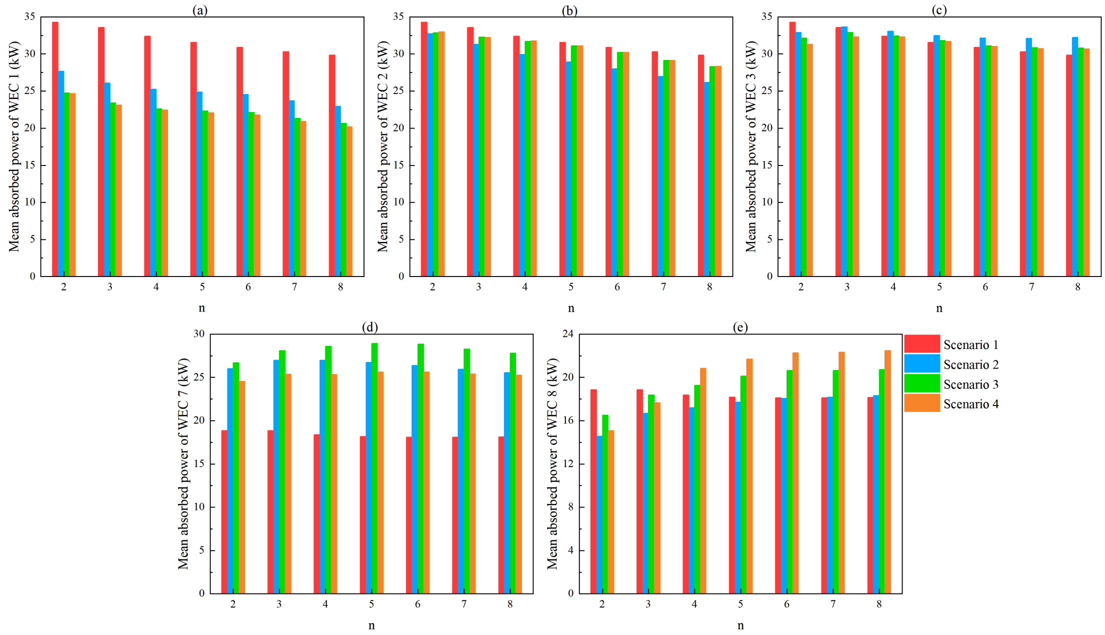

Figure 3.15: Absorbed power of the WECs among different scenarios for various spreading exponents under EC1.

q_s is proposed, of which the calculation formula can be expressed as:

$$q_s = \frac{P_m^i}{P_s^i} \tag{3.1}$$

where P_m^i and P_s^i denote the capture power of the i-th WEC among multi-body scenario (including Scenarios 2-4) and Scenario 1, respectively.

Figures 3.16 illustrate q_s of the individual WECs among Scenarios 2-4 under EC1 with different spreading components. From Figure 3.16(a), it can be observed that the value of q_s of WEC 1 are smaller than 1 among three scenarios, indicating that hydrodynamic interactions are not conducive to the power absorption of WEC 1. Furthermore, q_s decreases progressively from Scenario 2 to Scenario 4, implying that the presence of platform negatively affect the power capture of WEC 1. The discrepancy of q_s between Scenario 2 and Scenario 3 is more pronounced than that between Scenario 3 and Scenario 4, suggesting that the hydrodynamic interference induced by the platform has a more significant impact on the power absorption of WEC 1. Notably, among three scenarios, the variation trend of q_s across the spreading component is consistent, with n=2 and n=8 representing the points of maximum and minimum values, respectively.

It can be seen from Figure 3.16(b) that the value of q_s of WEC 2 are also smaller than 1 among three scenarios. Additionally, q_s among Scenarios 3 and 4 are larger than that among Scenario 2, while q_s among Scenarios 3 and 4 is almost consistent. This suggests that the presence of platform mitigates the negative impact of the hydrodynamic interactions within the WEC array on the power absorption of WEC 2. Specifically, for n=5, due to the inclusion of platform, the absorbed power of WEC 2 among Scenarios 3 and 4 is close to that among Scenario 1. It is noteworthy that among Scenarios 3 and 4, q_s initially increases and then decreases with the spreading component, while among Scenario 2, it shows a decreasing trend. This indicates that among Scenario 2, the negative impact of hydrodynamic interactions within the WEC array increases with the spreading component.

In Figure 3.16(c), it can be found that among Scenarios 3 and 4, the value q_s of WEC 3 is close to 1 as n=4, while that is smaller and larger than 1 for $n < 4$ and $n > 4$, respectively. This indicates that the spreading component (n=4) serves as a threshold for the platform to benefit the energy conversion of WEC 3. Additionally, q_s of WEC 3 among Scenario 2 is larger than that among Scenarios 3 and 4, suggesting that the inclusion of the platform is detrimental to the energy conversion of WEC 3. For $n < 4$, q_s of WEC 3 among Scenario 3 is larger than that among Scenario 4, while for $n > 3$, that is close among both scenarios. This implies that when the wave distribution is relatively scattered, the platform motion further hinders the performance of WEC 3.

As shown in Figure 3.16(d), the value of q_s of WEC 7 is larger than 1 among three scenarios, indicating that the hydrodynamic interactions enhance its energy absorption. q_s among Scenario 2 is larger than that among Scenario 4 but smaller than that among Scenario 3, which indicates that the hydrodynamic interference induced by the platform significantly enhances the performance of WEC 7, while the platform motion remarkably diminishes this advantage. Additionally, the variation trend in q_s across the spreading component is similar among three scenarios, initially increasing and then decreasing. This means that the maximum advantage of hydrodynamic interactions is realized for a specific spreading component.

It can be noticed from Figure 3.16(e) that, the value of q_s of WEC 8 among Scenario 2 is smaller than 1 for $n < 6$, and approximate to 1 for $n > 5$. For $n < 4$, the value of q_s of WEC 8 among Scenarios 3 and 4 is smaller than 1, indicating that the inclusion of platform is detrimental to the power absorption when the wave distribution is relatively scattered. Additionally, q_s of WEC 8 among Scenario 2 is smaller that that among other two scenarios, suggesting that the inclusion of platform improves its power capture. Furthermore, for $n > 3$, q_s among Scenario 4 is larger than that among Scenario 3. This means the platform motion has a positive impact on the performance of WEC 8 as the wave distribution is focused.

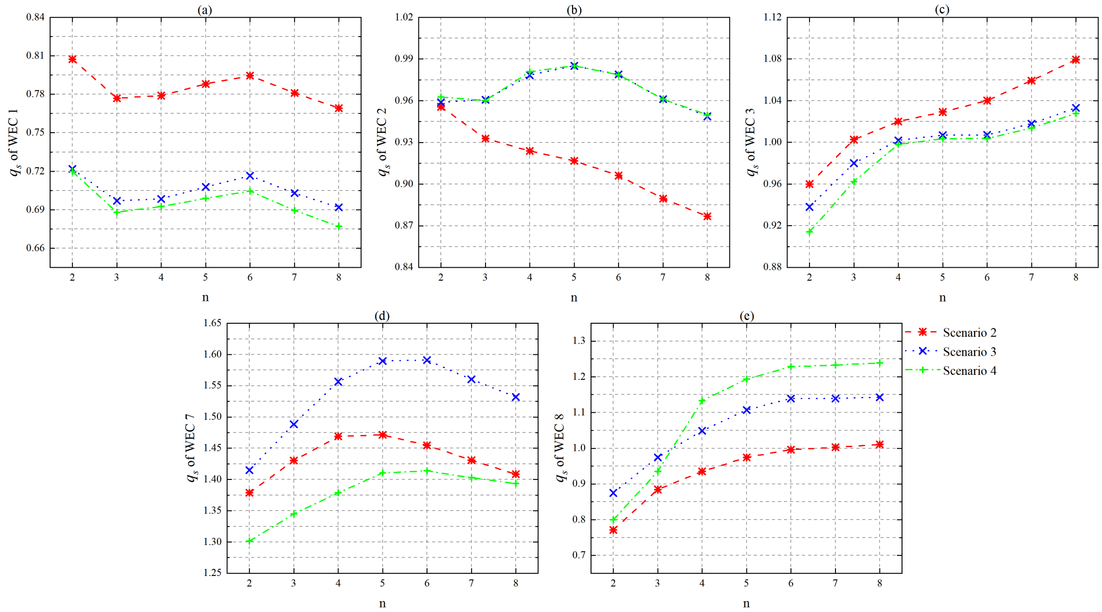

Figure 3.16: q_s of the WECs among different scenarios for various spreading exponents under EC1.

The WEC row

Figure 3.17 illustrates the mean absorbed power of WEC rows among Scenarios 2-4 under EC1 with various spreading components. It can be observed from the figure that, the absorbed power of Row 1 is larger than that of Row 3. This can be attributed to the fact that Row 1 is arranged more perpendicular to the mean incident wave direction. Under multidirectional short-crested wave conditions, the vertical responses of the WECs in Row 1 relative to the hinges are larger than those of the WECs in Row 3. The absorbed power of Row 1 decreases with the spreading component, indicating that the more focused the wave distribution is, the poorer the performance of Row 1 is. Additionally, the power absorption of Row 1 is the highest among Scenario 2 and the lowest among Scenario 4, suggesting that the presence of platform is detrimental to the performance of Row 1.

For Row 3, its performance is best among Scenario 3, implying that the hydrodynamic interference induced by the platform can enhance the power absorption of Row 3, whereas the platform motion diminishes this advantage. The absorbed power of Row 3 shows an initial increasing and then decreasing trend across the spreading component among Scenarios 2 and 3. In addition, among Scenario 4, the performance of Row 3 steadily improves for $n < 7$, while the power absorption of Row 3 remains almost unchanged for $n > 5$. Furthermore, the power absorbed by Row 3 among Scenario 2 is more than that among Scenario 4 when the spreading component is relatively small, and vice versa when the spreading component is relatively large. This phenomenon suggests that whether the presence of platform is beneficial for the power absorption of Row 3 depends on the wave distribution.

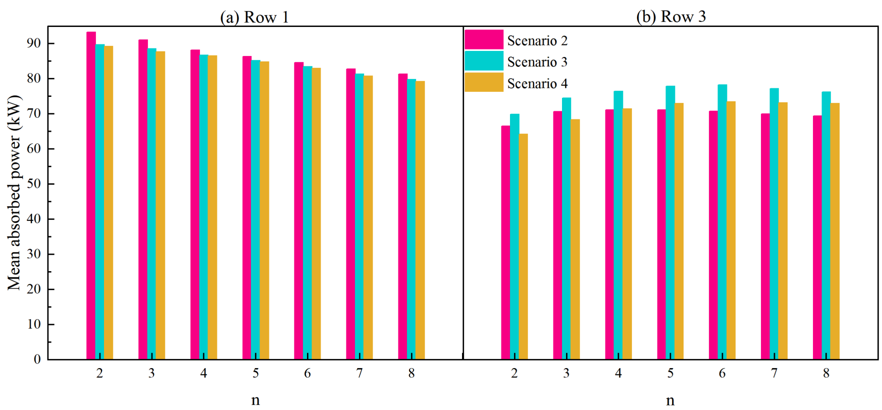

Figure 3.17: Absorbed power of the WEC rows among different scenarios for various spreading exponents under EC1.

To quantify the impact of hydrodynamic interactions and platform motion on the power capture of WEC rows, an influence factor q_r is proposed, which can be formulated as:

$$q_r = \frac{\sum_{i=(j-1)\times 3+1}^{j\times 3} P_m^i}{\sum_{i=(j-1)\times 3+1}^{j\times 3} P_s^i} \tag{3.2}$$

where j denotes the index of WEC row.

Figure 3.18 illustrates q_r of the WEC rows among Scenarios 2-4 under EC1 with various spreading exponents. It can be observed from the figure that, the value of q_r of Row 1 is smaller than 1, indicating that the hydrodynamic interactions are detrimental to its power absorption. Additionally, q_r of Row 1 is the highest among Scenario 2 and the lowest among Scenario 4, suggesting that the presence of the platform further diminishes the performance of Row 1. q_r of Row 1 among Scenario 2 does not vary significantly with the spreading component. Meanwhile, among Scenarios 3 and 4, q_r of Row 1 initially increases and then decreases with the spreading component. These phenomena demonstrate that the power absorption of Row 1 is more significantly affected by the wave directionality among Scenarios 3 and 4 compared to Scenario 2.

For Row 3, the value of q_r is larger than 1, which means that hydrodynamic interactions promote its energy conversion. In addition, q_r of Row 3 is the highest among Scenario 3, reflecting that the hydrodynamic interference of platform enhance its performance, while the platform motion diminishes this advantage. It is noteworthy that the spreading component (n=4) marks the point where the performance of Row 3 among Scenario 2 begins to fall behind that among Scenario 4. Furthermore, q_r of Row 3 shows an initial increasing and then decreasing trend across the spreading component, while the decreasing trend is relatively moderate compared to the increasing trend. This phenomenon indicates that compared to focused wave distributions, the performance of Row 3 is more likely to be influenced under scattered wave distributions.

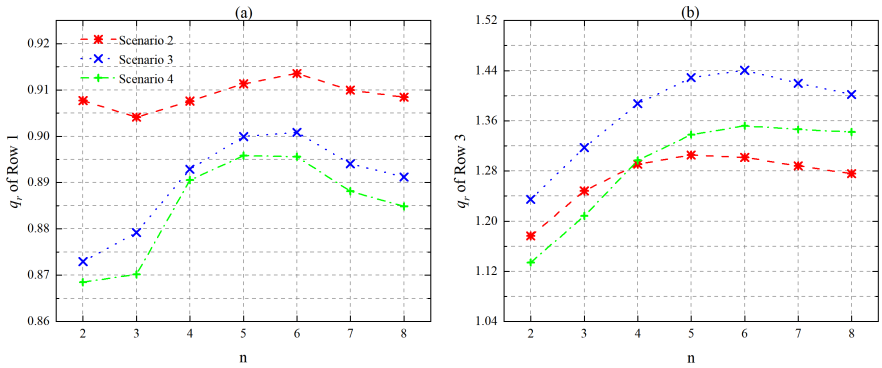

Figure 3.18: q_r of the WEC rows among different scenarios for various spreading exponents under EC1.

The WEC array

Figure 3.19 illustrates the total absorbed power of the WEC array among Scenarios 2-4 under ECs 1-3 with various spreading components. From Figure 3.19(a), it can be observed that under EC1, the power absorbed by the WEC array remains almost constant for lower spreading components ($n < 4$), but declines as the spreading component increases. This suggests that the performance of WEC array decreases when the wave directionality is focused. Additionally, among Scenario 3, the power absorbed by the WEC array is slightly lower than that among Scenario 2 only at $n = 2$. For the other spreading exponents, the WEC array among Scenario 3 demonstrates superior performance compared to that among other two scenarios. Furthermore, the least power is absorbed among Scenario 4 compared to the other two scenarios. This phenomenon demonstrates that the platform motion is detrimental to the performance of the WEC array.

In Figure 3.19(b), it is evident that under EC2, the WEC array absorbs the most power among Scenario 3 and the least among Scenario 4. This indicates that the hydrodynamic interference induced by the platform is disadvantageous to power absorption of the WEC array. Overall, the power absorbed by the WEC

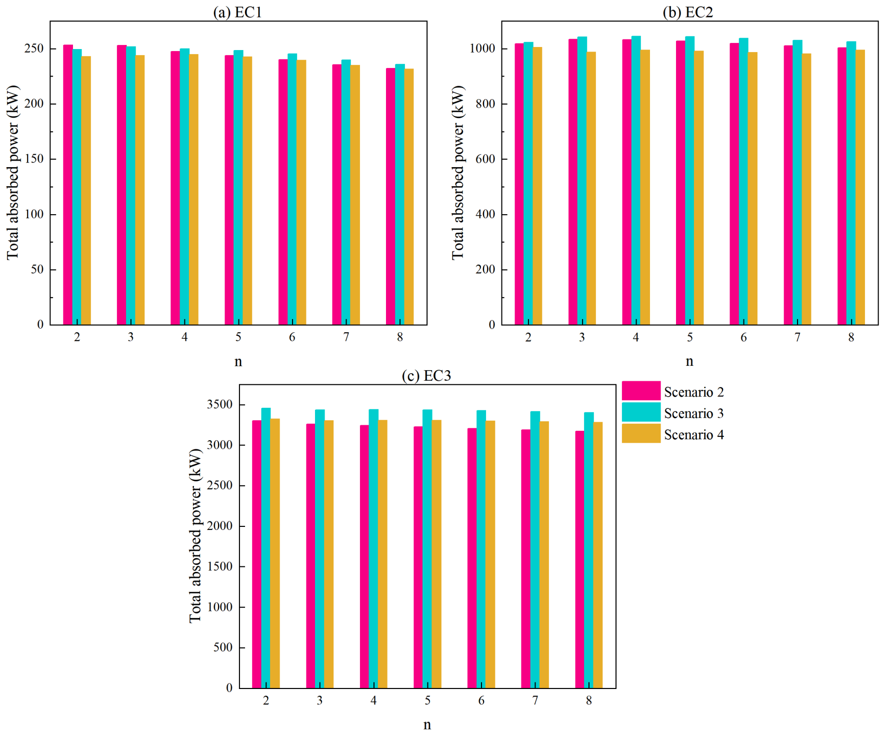

Figure 3.19: Absorbed power of the WEC array among different scenarios for various spreading exponents under EC1-EC3.

arrays among Scenarios 2 and 3 shows an initially increasing and then decreasing trend across the spreading component, while its absorbed power among Scenario 4 shows no clear trend across the spreading component. However, there is no significant difference in power absorption of the WEC array for different spreading components, which reflects that the wave directionality does not significantly affect the performance of the WEC array.

As seen in Figure 3.19(c), the power absorbed by the WEC array is the highest among Scenario 3 and the lowest among Scenario 2 under EC3. This implies that the presence of platform enhances the performance of the WEC array, but the platform motion diminishes this advantage. Additionally, among Scenario 2, there is a slight downward trend in power absorption of the WEC array across the spreading component, whereas its performance among Scenarios 3 and 4 shows slight variation for different spreading components. This indicates that the power absorption of the WEC array is less affected by the wave distribution under EC3.

To quantify the impact of the hydrodynamic interactions and platform motion on the power capture of the WEC array, an influence factor q_t is proposed, of which the calculation formula can be written as:

$$q_t = \frac{\sum_{i=1}^{9} P_m^i}{\sum_{i=1}^{9} P_s^i} \tag{3.3}$$

Figure 3.20 illustrates q_t of the WEC array among Scenarios 2-4 for different spreading components under EC1-EC3. From Figure 3.20(a), it can be observed that under EC1, the value of q_t of the WEC array among scenarios 2 and 4 are smaller than 1. Meanwhile, q_t of the WEC array among Scenario 3 are smaller than 1 for $n < 5$ but larger than 1 for the other spreading components. Additionally, q_t of the WEC array is minimal among Scenario 4. For $n < 4$, q_t of the WEC array among Scenario 2 is larger than that among Scenario 3, but the opposite trend is observed for the other spreading components. Furthermore, for $n > 5$, the difference in q_t of the WEC array between Scenarios 2 and 4 is slight. These phenomena demonstrate that the hydrodynamic interference induced by the platform can promote the performance of the WEC array under the focused wave distribution, whereas the platform motion significantly diminishes this advantages.

As shown in Figure 3.20(b), under EC2, the vlaue of q_t of the WEC array is larger than 1, indicating that the hydrodynamic interactions are favorable for its power absorption. q_t of the WEC array is the largest among Scenario 3 and the smallest among Scenario 4, which implies that the platform-induced interference enhances the performance of the WEC array among Scenario 2, whereas the platform motion has the opposite effects. Additionally, q_t of the WEC array among Scenarios 2 and 3 exhibits an increasing trend across the spreading component, demonstrating that the hydrodynamic interactions among Scenarios 2 and 3 contribute more to the power absorption of the WEC array under more focused wave distribution.

It can be seen from Figure 3.20(c) that under EC3, the value of q_t of the WEC array is also larger than 1. In addition, q_t of the WEC array is maximal among Scenario 3 and minimal among Scenario 2, indicating that the presence of platform enhances its performance, but the platform motion slightly diminishes this advantage. Furthermore, q_t of the WEC array shows an upward trend across the spreading component among these three scenarios, which reflects that the power absorption of the WEC array benefits more from the hydrodynamic interactions when the wave distribution becomes more focused.

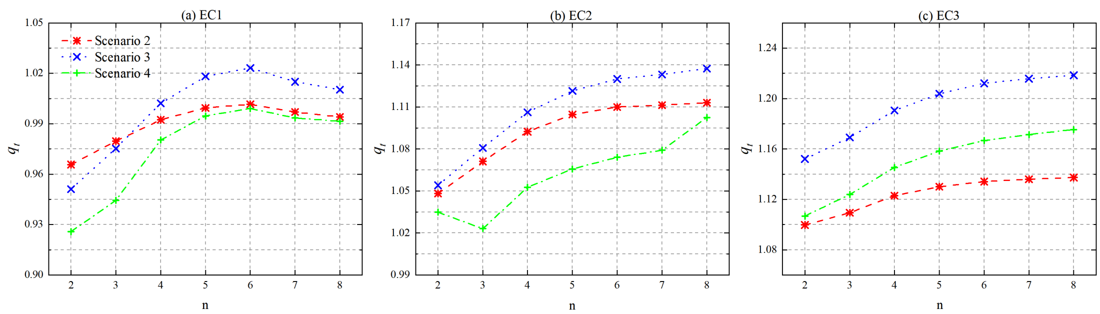

Figure 3.20: q_t of the WEC array among different scenarios for various spreading exponents under EC1-EC3.

3.4 Summary

This chapter investigates the dynamic response and power capture characteristics of the floating wave-energy harvesting platform under short-crested wave conditions. A series of time-domain simulations are conducted to analyze the effects of the wave distribution on the platform motion, mooring line tension, and the power absorption of this wave-energy capture system. Five ECs are selected, including three operational conditions and two severe conditions. Based on the results, some key conclusions are summarized as follows:

(1)Under EC1, the mean surge response shows slight variations across different spreading components, whereas under EC2-EC5, it exhibits an increasing trend. A transition occurs in the mean heave and pitch responses under EC1 when the spreading component exceeds 3, while under EC2, they are relatively small for the spreading components of 2 and 8. Additionally, under EC3-EC5, the mean heave and pitch responses remain almost constant for various spreading components.

(2)Under EC1-EC4, the STD of the surge response shows an increasing trend across the spreading component, whereas under EC5, it exhibits a decreasing trend. Under EC1 and EC4, the STD of the heave response increases with the spreading component, while under EC2-EC3 and EC5, it remains almost constant. Additionally, the STD of the pitch response demonstrates an increasing trend across the spreading component under EC1-EC5.

(3)For the #5 tension response, the wave distribution has a slight impact on its mean value and STD under EC1-EC3. However, under EC4-EC5, both the mean value and STD of the #5 tension response exhibit a decreasing trend across the spreading component.

(4)Under EC1, WEC 1 absorbs significantly more power among Scenario 1 compared to the other three scenarios, whereas the opposite trend is observed for WEC 7. In addition, Row 1 exhibits a decreasing trend in power absorption among Scenarios 2-4 across the spreading component under EC1. Furthermore, Row 1 and Row 3 absorb the most power among Scenarios 2 and 3 under EC1, respectively.

(5)For the WEC array, under EC1, there is a slight decreasing trend in its power absorption across the spreading component. Under EC2-EC3, the power captured by the WEC array among the three multi-body scenarios shows slight variation with the spreading components. In addition, under EC1-EC3, Scenario 3 can be regarded as the best design for the WEC array.

Numerous works have been conducted on wave-energy capture systems in irregular waves wave, but few of them consider the short-crested wave conditions. This chapter investigates the proposed wave-energy harvesting platform in short-crested waves, analyzing its dynamic responses and captured power under different wave distributions. Since multidirectional wave propagation is commonly encountered in real ocean environments, this work provides useful reference for the engineering design and performance evaluation of this type of offshore structures.

Chapter 4

The floating wave-energy harvesting platform under wave-current interaction

This chapter explores the effects of WCI on the dynamic behavior of the floating wave-energy harvesting platform under a typically operational condition. After completing the verification of this spectral model input with WCI effects introduced in Chapter 2, a series of time-domain simulations are employed to implement multiple loading scenarios, which consider the current direction, current velocity as well as WCI. The findings demonstrate that the presence of current significantly alters the wave excitation forces, leading to notable changes in the platform motion, mooring line tension and power absorption of this wave-energy capture system. Since the WCI is a common physical phenomenon in marine environments, this study highlights the importance of incorporating it in the analysis of wave-energy harvesting platforms under combined wave–current conditions.

4.1 Verification of the spectral model input with WCI effects

Since this chapter focuses on the proposed wave-energy capture platform under combined irregular wave and current conditions, it is necessary to verify the spectral model input with WCI effects introduced in Chapter 2.

Figure 4.1 compares the wave spectra with WCI effects obtained in the present study with those reported by Qu et al. [47]. The irregular wave is modelled using the JONSWAP spectrum, with the parameters set as $H_s = 9.14$ m, $T_p = 13.6$ s, and $\gamma = 1$. The current is assumed to be uniform, and two velocity cases are considered, namely $u = -1$ m/s and 1 m/s. As shown in the figure, the results obtained in the present study are generally in good agreement with those reported by Qu et al. Therefore, the spectral model with WCI effects adopted in this thesis is considered reliable for the subsequent analysis.

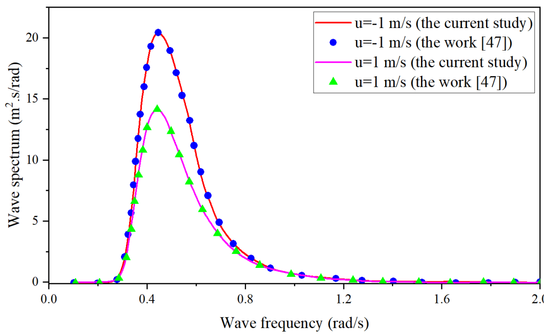

Figure 4.1: Comparison of the wave spectra with WCI effects between the current study and the work presented by Qu et al. [47].

4.2 Results and discussion

This section focuses on the influence of WCI on the performance of the floating wave-energy harvesting platform under operational conditions. Under these ECs, the wind is assumed to be negligible, while only the irregular wave and current are considered. The irregular wave is simulated with H_s=3.8 m, T_p=8.3 s, and γ=2.4 [93]. For operational sea states at the selected site, the typical current velocity ranges from 0.5 m/s to 0.7 m/s [93]. In this study, the maximum current velocity is assumed to be 0.5 m/s for the present EC, and three current velocities (u=0 m/s, 0.25 m/s and 0.5 m/s) are considered. Additionally, the wave incident angle is fixed at 0°, while the current incident direction includes 0° and 180°.

Cao et al. [93] investigated the dynamic behavior of the SPIC semi-submersible platform under combined long-crested wave and current conditions without considering WCI. However, in real marine environments, WCI is commonly encountered and may significantly modify wave characteristics, thereby affecting the dynamic responses and power capture of offshore structures. Therefore, further investigation into the influence of WCI on the proposed wave-energy harvesting platform is essential for improving the reliability of its design and performance assessment.

For each time-domain simulation, the total simulation duration is set to 4100 s. The Cummins equation of motion is resolved using a time step of 0.1 s, while a finer time step of 0.01 s is employed to solve the motion equations of the mooring lines. To minimise the effects of initial transient responses, the first 500 s of time history from each simulation are discarded.

4.2.1 Characteristics of wave spectra

Figure 4.2 presents the wave spectra under various current velocities, which varies from -0.5 m/s to 0.5 m/s with an interval of 0.25 m/s. As shown in the figure, the spectral peak becomes larger under the opposing current, while the situation is reversed under the following current. Additionally, the wave spectrum under opposing current exhibits a wider frequency bandwidth compared to that under following current. Furthermore, the figure shows that the spectral value is larger under higher opposing current velocity, while the spectral value decreases as the velocity increases under the following current.

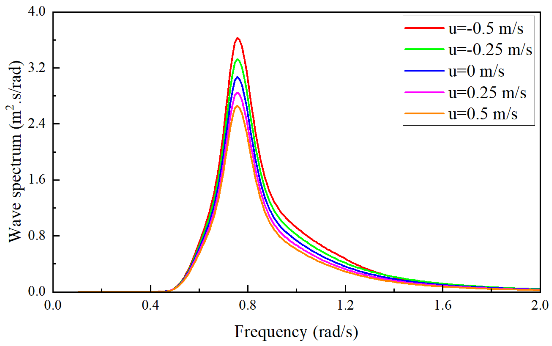

Figure 4.2: The wave spectra with various current velocities.

4.2.2 Determination of PTO damping coefficient

A parametric study is conducted to seek the optimal PTO damping coefficient for the WEC to absorb the most power, which varies from 4.3×10^4 kN·m·s/rad to 5.8×10^4 kN·m·s/rad. Figure 4.3 presents the absorbed power of the WEC with various PTO damping coefficients under different current velocities. As shown in the figure, the maximum power of the WEC from u = -0.5 m/s to 0.5 m/s, is 131.3 kW, 118.2 kW, 110.5 kW, 101.2 kW, and 93.09 kW, respectively. Within this range of current velocities, the maximum power of the WEC shows a decreasing trend. This is because the vertical response of the WEC decreases because of the decreased amplitude of the wave components. Additionally, the WEC can absorb the most power at multiple PTO damping coefficients. However, to facilitate subsequent comparative studies on the impact of current velocity, the optimal PTO damping coefficient is determined to be 5.06×10^4 kN·m·s/rad.

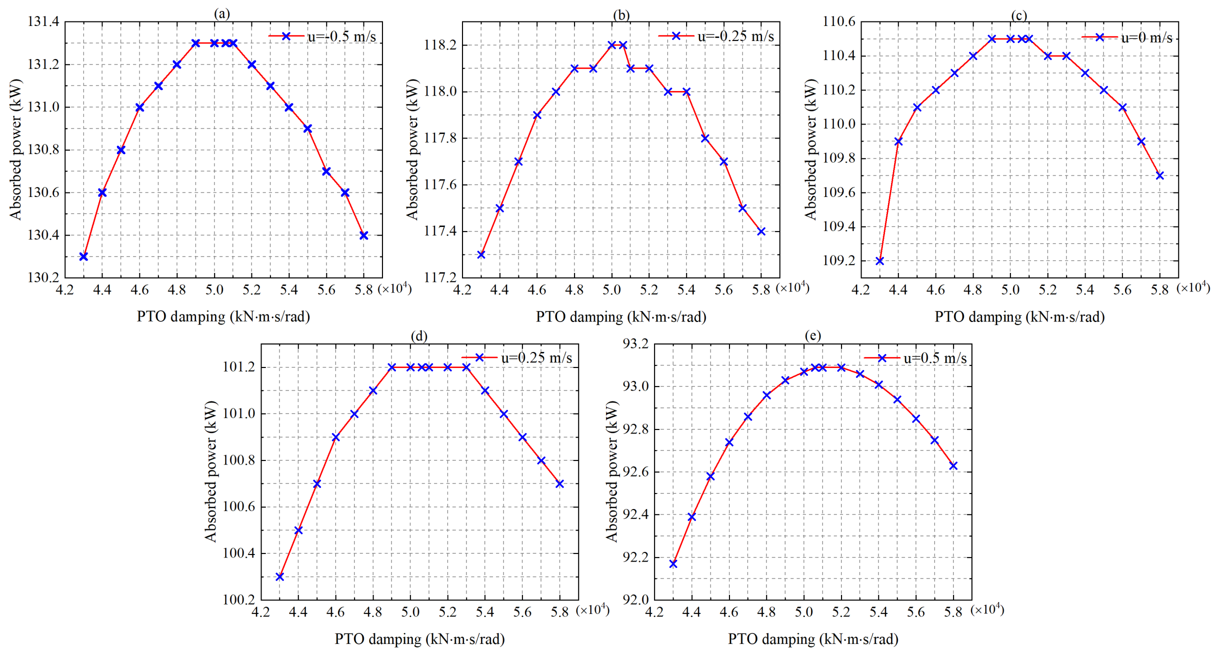

Figure 4.3: Absorbed power of the WEC with various PTO damping coefficients under various current velocities: (a) u=-0.5 m.s; (b) u=-0.25 m/s; (c) u=0 m/s; (d) u=0.25 m/s; (e) u=0.5 m/s.

4.2.3 Wave excitation forces and moments acting on the platform

Figure 4.4 presents the mean values and standard deviations (STDs) of the first-order wave force and moment responses in the surge, heave, and pitch DoFs with various current velocities. The figure reveals that the mean value of the

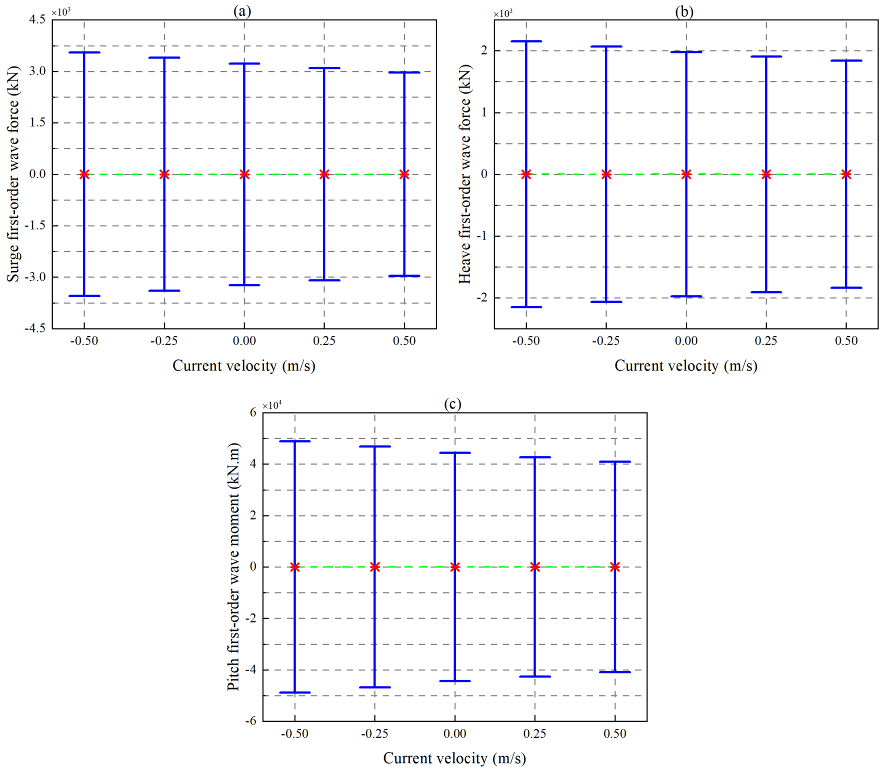

Figure 4.4: First-order wave forces and moments in the surge (a), heave (b) and pitch (c) DoFs under different current velocities.

first-order wave force response remains zero because the first-order wave force is calculated as a linear superposition of harmonic wave components. Meanwhile, the STD of the first-order wave force response shows a decreasing trend across the current velocity range. This can be attributed to the gradual reduction in spectral density as the current velocity changes from -0.5 m/s to 0.5 m/s (as shown in Figure 4.2). Consequently, the amplitudes of the wave components decrease, leading to a reduction in the corresponding first-order wave force.

Figure 4.5 illustrates the mean values and STDs of the second-order wave force and moment responses in the surge, heave, and pitch DoFs under different current velocities. For the semi-submersible platform, the second-order wave forces involve the slow-drift and mean drift wave forces. As shown in the figure,

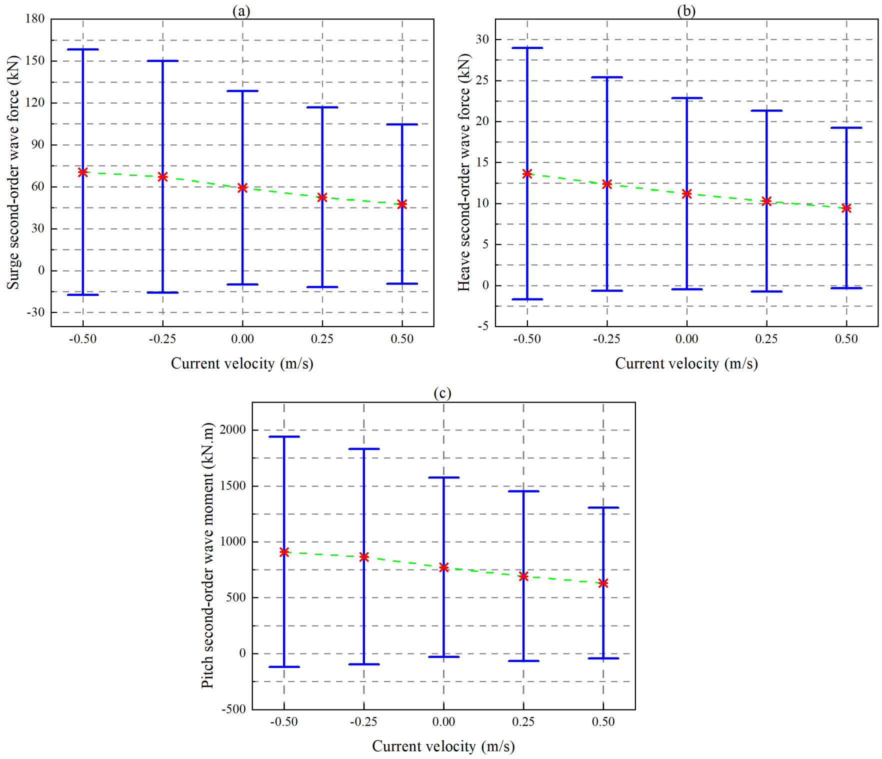

Figure 4.5: Second-order wave forces and moments in the surge (a), heave (b) and pitch (c) DoFs under different current velocities.

the second-order wave force response exhibits a non-zero mean value due to the contribution of the mean drift force. Additionally, the mean value and STD of the second-order wave force response exhibit a decreasing trend across this current velocity range. This is also because the amplitudes of wave components gradually decrease with the current velocity changing from -0.5 m/s to 0.5 m/s, leading to a reduction in the corresponding slow-drift force.

4.2.4 Platform motion

Figure 4.6 shows the mean values and STDs of the platform responses in the surge, heave, and pitch DoFs with and without WCI. In this figure, "without current" denotes the reference case with (u=0 m/s), whereas "with WCI" and "without WCI" refer to the current cases with and without the current-induced modifications on the wave spectrum, respectively.

In Figure 4.6(a), it can be observed that across the current velocity range (u=-0.5 m/s - 0.5 m/s), the surge mean response exhibits an increasing trend. The opposing current tends to weaken the excitation effects of the surge mean drift force, leading to a reduction in the mean response without the current. Meanwhile, when the wave and current directions are aligned, the surge mean response increases significantly. Due to WCI, the opposing current increases the surge mean drift force, while the following current reduce it. Therefore, when the wave and current have opposite directions, the surge mean response with WCI is larger than that without WCI, while the case is opposite when the current follows the wave.

Generally, the surge STD is affected by both second-order slow-drift and first-order wave forces, with the former playing a dominant role. Without WCI, the surge STD is originally expected to be the same with that without current. However, the figure shows that the surge STD at u=0 m/s is larger than those at other current velocities. Meanwhile, regardless of whether the current is opposing or following, a higher current velocity lead to a smaller surge STD. This indicates that the current acts as a damping mechanism, reducing the oscillation amplitude of the response. A higher current velocity implies stronger damping effects. When the velocity is the same, the opposing current results in a larger surge STD with WCI compared to the following current. Meanwhile, the surge STD with WCI is larger than that without WCI under the opposing current, while under the following current, the situation is reversed. These phenomena are due to the fact that the surge slow-drift and first-order wave forces with WCI have a decreasing trend across the current velocity range (u=-0.5 m/s - 0.5 m/s).

As seen in Figure 4.6(b), across the current velocity range (u=-0.5 m/s - 0.5 m/s), both the mean value and STD of the heave response show a decreasing trend. Within this current velocity range, the surge mean response increases, resulting in a longer suspension length of the upstream mooring line. Therefore, the heave restoring stiffness also increases, which explains the reduction in the heave response. Additionally, the heave mean value with WCI is similar to that without WCI. This is because the hydrostatic restoring stiffness in the heave DoF is relatively large, and the variation in the mean drift force is insufficient to change the mean equilibrium position. However, the heave STD shows noticeable changes due to WCI. When the current and wave have opposite directions, the heave STD with WCI is larger than that without WCI, while the situation is reversed when the current follows the wave. This is because the opposing current increases the first-order wave force, while the following current has the opposite impact.

From Figure 4.6(c), the pitch mean response decreases within the current velocity (u=-0.5 m/s - 0.5 m/s). The excitation effects of the opposing current exceed that of the pitch mean drift moment, causing the platform to rotate clockwise around its CoG. In the absence of current, the pitch mean response is negative due to the mean drift moment. When the wave is aligned with the current, the platform continues to rotate counterclockwise. Furthermore, when the current and wave have opposite directions, the pitch mean response with WCI is slightly smaller than that without WCI, while the situation is reversed when the wave is aligned with the current. Due to WCI, the opposing current increases the pitch mean drift moment, partially counteracting the excitation effects of the current. Under the following current, the mean drift moment decreases with WCI, which causes the pitch mean response to be larger than that without WCI.

It is worth noting that the current also has damping effects on the pitch DoF. The figure shows that the pitch STD is maximal in the absence of current. Without WCI, the damping effects are more pronounced in the opposing current compared to the following current, and the damping effects increase with a higher current velocity. However, with WCI, the damping effects are not prominent in the opposing current due to the increase in the pitch slow-drift and first-order wave moments. This can be inferred from the nearly identical pitch STD under u = -0.5 m/s and u = -0.25 m/s. Additionally, the pitch STD with WCI is larger than that without WCI under the opposing current, while the situation is reversed under the following current. This is because with WCI, the following and opposing currents respectively decrease and increase the pitch slow-drift and first-order wave moments.

To further evaluate the influence of WCI on the platform DoFs, the significant amplitudes (SAs) of the motion responses are selected. In this section, the SAs of the low-frequency (LF) and wave-frequency (WF) responses in the surge, heave, and pitch DoFs are presented, and they can be calculated using the following formula [41]:

$$A_s = 2\sqrt{\int_{\omega_1}^{\omega_2} S_{mr}(\omega)\, d\omega} \tag{4.1}$$

where $S_{mr}(\omega)$ is the motion response spectrum. ω_1 and ω_2 represent the start and end frequencies for calculating the LF or WF SAs. In the analysis of the dynamic responses of floating structures, the frequency range of 0–0.2 rad/s is commonly defined as the LF region, whereas the range of 0.2–2 rad/s is taken as

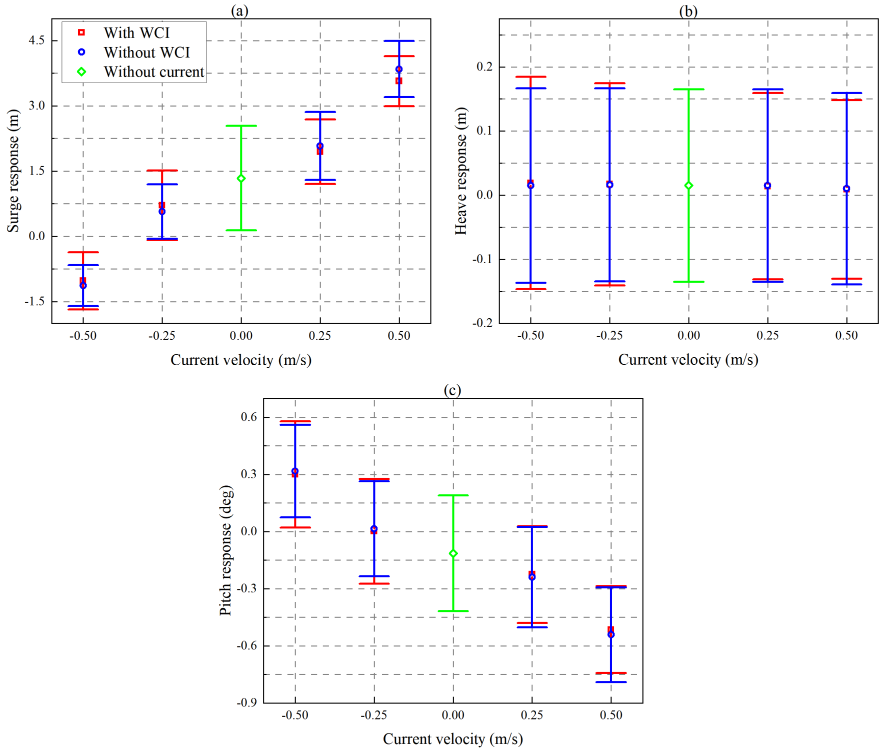

Figure 4.6: Mean values and STDs of the platform surge (a), heave (b) and pitch (c) responses with and without WCI.

the WF region [94]. Therefore, the same two frequency ranges are adopted in the present study to calculate the LF and WF SAs, respectively.

Figure 4.7 illustrates the SAs of the WF and LF motion responses with and without WCI. From Figure 4.7(a), the surge WF SA is much smaller than the LF one. Particularly in the absence of current, the surge motion only exhibits the LF response. This phenomenon suggests that the LF response dominates the surge motion. Under the opposing current, the surge LF SA with WCI is larger than that without WCI, while the situation is reversed under the following current. This can be attributed to the fact that the second-order drift wave force with WCI is enhanced under the opposing current, thereby inducing a larger surge LF response, while for the following current, the situation is reversed.

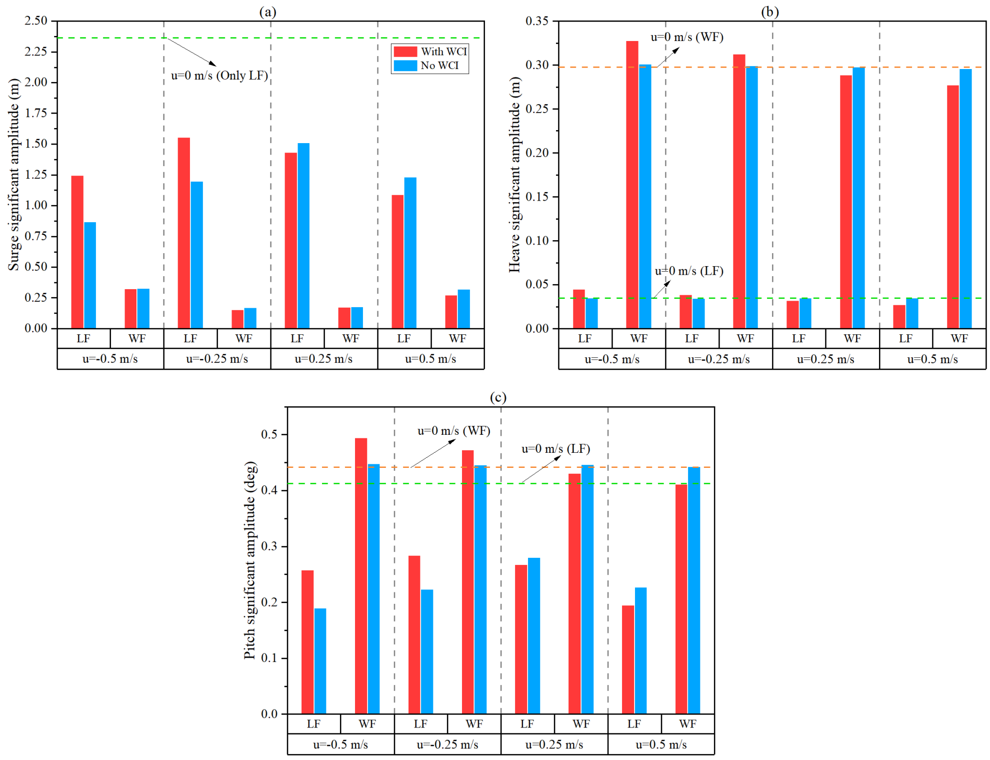

Figure 4.7: SAs of the LF and WF responses of the surge (a), heave (b) and pitch (c) DoFs with and without WCI.

Additionally, as seen in Figure 4.7(a), the surge LF SA without current is much larger than that with current, indicating notable damping effects of the current. Regardless of whether the current is opposing or following, a higher current velocity results in a smaller surge LF SA. This means that a higher current velocity corresponds to stronger damping effects on the surge LF response. Additionally, without WCI, the surge LF SA is larger under the following current compared to opposing current, suggesting that the opposing current has stronger damping effects. Due to the increase in the second-order drift wave forces with WCI under the opposing current, the surge LF SA is larger compared to the following current.

It can also be observed from Figure 4.7(a) that under the following current, the surge WF SA with WCI is smaller than that without WCI. This is attributed to the reduction in the first-order wave force due to WCI, which consequently leads to a weaker surge WF response. Under the opposing current, WCI increases the first-order wave force; therefore, the surge WF SA should be larger as expected. However, this figure shows the opposite situation. This is because that the enhanced second-order drift force with WCI produces a stronger LF excitation to the surge motion, thereby reducing the relative contribution of the first-order wave force and suppressing the WF response. Furthermore, a smaller current velocity results in a smaller surge WF SA under both opposing and following currents.

From Figure 4.7(b), the heave LF and WF SAs remain almost unchanged with varying current velocities without WCI, indicating that the current has no prominent influence on the heave response without WCI. This can be attributed the fact that the current acts in the horizontal direction, whereas the heave motion occurs in the vertical direction. Consequently, the current provides little excitation to the heave DoF when the WCI is not considered. Meanwhile, with WCI, both the heave LF and WF SAs exhibit a decreasing trend across the current velocity (u=-0.5 m/s - 0.5 m/s). This is because that the second-order drift and first-order wave forces decrease within this current velocity range. Furthermore, the heave WF SA is significantly larger than the LF one, indicating that WF response dominates the heave motion.

As shown in Figure 4.7(c), although the pitch WF SA is larger than the LF one, the difference between them is not significant. This indicates that the pitch motion can not neglect the LF response. Interestingly, the variation patterns of the pitch LF SA regarding the current velocity and WCI are similar to those of the surge one. This is due to the coupling effects between the pitch and surge DoFs, the former's LF response is induced by the latter. As for the pitch WF SA, its variation patterns concerning the current velocity and WCI are similar to those of the heave one. This phenomenon is primarily attributed to the impainfluence of WCI on the first-order wave force.

4.2.5 Mooring line tension

Considering #1 and #5 are located at the downstream and upstream positions, respectively, this section selects them to evaluate the impact of WCI on mooring line tension response.

Figure 4.8 presents the mean values and STDs of the tension responses of #1 and #5 with and without WCI. The figure shows that the mean value of #5 tension exhibits the variation patterns with respect to the current velocity and WCI consistent with the surge mean response, while the mean tension response of #1 exhibits an opposite trend. These phenomena results from the positions of the mooring lines. Furthermore, the STD of tension response without current is larger than that with current, suggesting that the current has damping effects.

Figure 4.8(a) shows that regardless of the following or opposing current, a larger current velocity causes stronger damping effects. Under the opposing current, the STD of #1 tension response with WCI is larger than that without WCI, while under the following current, the situation is reversed. Meanwhile, with WCI, the STD of #1 tension response under the following current is smaller than that under the opposing current. These phenomena are similar to those for the surge STD.

It is evident from Figure 4.8(b) that With WCI, a higher current velocity

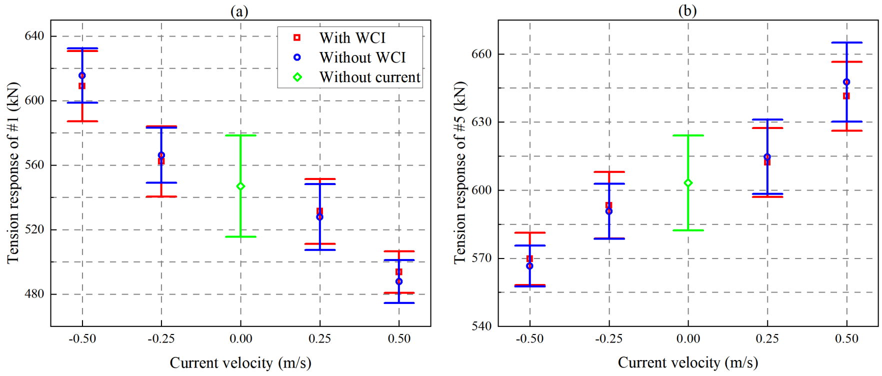

Figure 4.8: Mean values and STDs of the tension responses of #1 (a), and #5 (b) with and without WCI.

implies stronger damping effects. Meanwhile, the STD of #5 tension response under the opposing current is smaller than that under the following current, indicating that the damping effects of the current are particularly prominent under the opposing current. Additionally, without WCI, the damping effects under the opposing current decrease with a smaller current velocity, whereas the situation is reversed for the following current. Similar to #1, under the opposing current, the STD of #5 tension response without WCI is smaller than that with WCI, while under the following current, the situation is reversed.

To further explore the impact of WCI on the mooring line tension, the SAs of the LF and WF tension responses of #1 and #5 are presented in Figure 4.9, with their calculation formula identical with Eq. (4.1) for the platform motion.

In Figure 4.9(a), the LF SA of #1 tension is much larger than the WF one, indicating that the LF response contributes more to the #1 tension. Particularly in the absence of current, the #1 tension response only has the LF SA. However, in the presence of current, the contribution of WF response cannot be neglected. It is noteworthy that the variation patterns of the LF SA of #1 tension with respect to current velocity and WCI are similar to those of the surge LF SA,

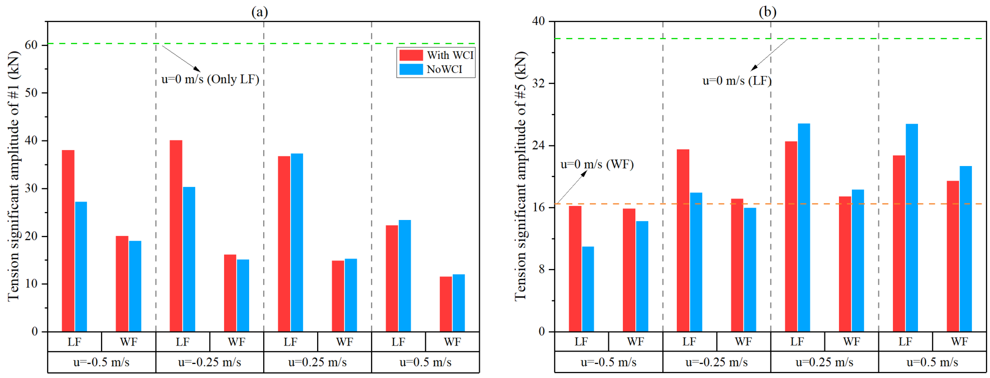

Figure 4.9: SAs of the LF and WF responses of #1 tension (a), and #5 (b) with and without WCI.

suggesting that the LF tension response of the downstream mooring line relies on the surge LF response. When the current is opposing, the WF SA of #1 tension is larger at a higher current velocity, while the situation is reversed for the following current. Besides, under the opposing current, the WF SA of #1 tension with WCI is larger than that without WCI, while under the following current, the situation is reversed. These phenomena can be attributed to the fact that the opposing and following currents can respectively increase and decrease the first-order wave forces.

It can be observed from Figure 4.9(b) that, for #5, the difference between the WF and LF SAs of the tension response is smaller compared to the #1. Particularly at u=-0.5 m/s, the WF SA of #5 tension with WCI is only slightly smaller than the LF one, while without WCI, the WF SA even exceeds the LF one. Additionally, regarding the LF tension response, it is inferred that the damping effects of the opposing current are more prominent compared to the following current. Furthermore, when the current is opposing, the LF and WF SAs of #5 tension response with WCI are larger than those without WCI, while for the following current, the situation is reversed. This phenomenon is related to the fluence of current direction on the first-order and second-order drift wave forces. Moreover, the WF SA of #5 tension shows an increasing trend across the current velocity range (u=-0.5 $\sim$ 0.5 m/s). This suggests that for the WF tension response, the opposing current exhibits damping effects, while the following current displays amplifying effects. Besides, a larger current velocity causes more prominent corresponding effects.

4.2.6 Power capture performance

To evaluate the influence of WCI on the power capture of the wave-energy harvesting platform, the individual WEC, WEC row, and WEC array are selected for the research objective, respectively. For the individual WEC, WECs 1-3, WEC 7, and WEC 8 are selected for analysis. Regarding the WEC row, Rows 1 and 3 are considered. These selections are based on the fact that this wave-energy capture system is symmetric about the incident directions of wave and current forces.

Figure 4.10 shows the power absorbed by individual WECs with and without WCI. As seen in the figure, regardless of WCI, WEC 1 and WEC 3 absorb similar power at the same current velocity. Meanwhile, WEC 2 absorbs less power than WECs 1 and 3. This indicates that the vertical responses of WECs 1 and 3 relative to the hinges are larger than that of WEC2. Additionally, WECs 7 and 8 absorb much more power than WEC1-WEC3. This can be attributed to the fact that WECs 7 and 8 are positioned on the wave-facing side, where they are directly exposed to stronger incoming wave excitation. By contrast, the excitation acting on WECs 1–3 is substantially weakened because of the shielding effect and the energy absorption of the wave-facing WECs. Moreover, the performance of

WEC7 is superior to that of WEC8.

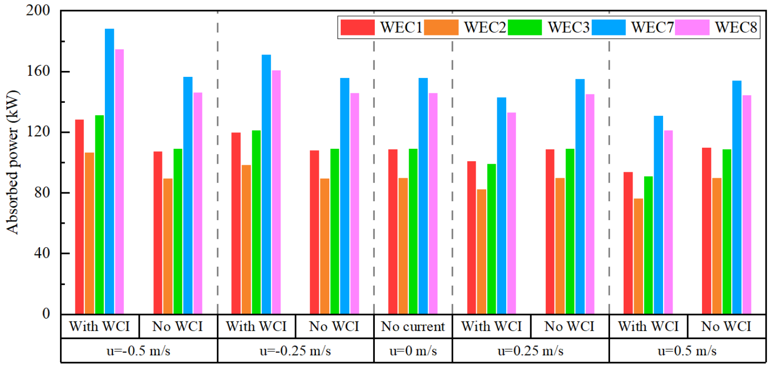

Figure 4.10: Absorbed power the individual WECs with and without WCI.

It can be also observed from Figure 4.10 that without WCI, the power absorbed by the individual WECs remains nearly constant over the range of current velocities (u=-0.5 $\sim$ 0.5 m/s), while the capture power of the individual WECs with WCI exhibits a decreasing trend across the current velocity. Furthermore, under the opposing current, the power absorbed by individual WECs with WCI is more than that without WCI, while under the following current, the situation is reversed. These phenomena can ultimately be attributed to the effects of WCI on the vertical excitation forces acting on the individual WECs.

Figures 4.11 and 4.12 respectively show the captured power of the WEC rows and WEC array with and without WCI. From the Figure 4.11, without WCI, the change in the current velocity does not alter the power absorbed by Rows 1 and 3. Meanwhile, with WCI, the power absorbed by Rows 1 and 3 gradually decreases within the current velocity range (u=-0.5 $\sim$ 0.5 m/s). Additionally, Row 3 performs better in energy conversion compared to Row 1. Furthermore, under the opposing current, the power absorbed by Rows 1 and 3 with WCI is larger than that without WCI, while under the following current, the situation is reversed.

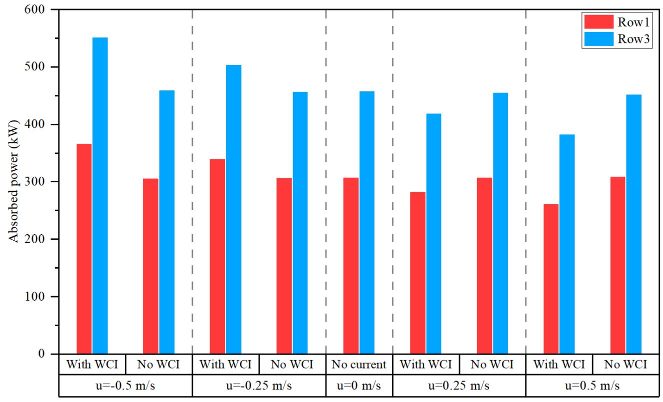

Figure 4.11: Absorbed power the WEC rows with and without WCI.

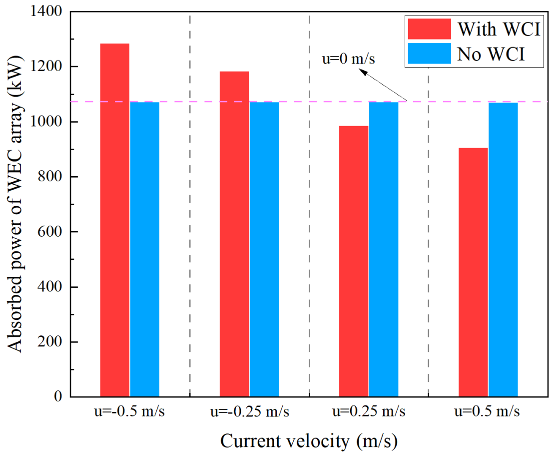

Figure 4.12: Absorbed power the WEC array with and without WCI.

As seen in Figure 4.12, the captured power of the WEC array without WCI remains unchanged under different current velocities. Meanwhile, with WCI, the captured power of the WEC array presents a decreasing trend across the current velocity range (u=-0.5 $\sim$ 0.5 m/s). Additionally, under the opposing current, the energy conversion performance of the WEC array with WCI is better than that without WCI, while under the following current, the situation is reversed.

4.3 Summary

This chapter investigates the dynamic responses and power capture characteristics of the floating wave-energy harvesting platform under combined irregular wave and current conditions. A series of time-domain simulations are conducted to evaluate the effects of WCI on the platform motion, mooring line tension, and the power absorption of this wave-energy capture system. Different current directions and velocities are considered in the analysis. Based on the results, some key findings are drawn as follows:

(1)The surge and heave motions of the platform are dominated by the LF and WF responses, respectively, while both LF and WF responses dominate the pitch motion. Additionally, the current exhibits damping effects on the LF responses of surge and pitch, while it amplifies the surge WF response. Furthermore, without WCI, the heave response and pitch WF response remain unchanged at different current velocities, while with WCI, they gradually decrease from u=-0.5 to 0.5 m/s.

(2)The LF responses of #1 and #5 tension are reduced due to the damping effects of the current, while the WF response of #1 tension is amplified by the current. Furthermore, the WF response of #5 tension shows an increasing trend from u=-0.5 to 0.5 m/s.

(3)Without WCI, the power absorbed by the individual WECs, WEC rows, and WEC array is almost unaffected by the variation in the current velocity. However, with WCI, their power harvesting performance gradually weakens within the current velocity range (u=-0.5 $\sim$ 0.5 m/s).

WCI is rarely considered in the existing studies on wave-energy capture systems under combined irregular wave and current conditions. To address this limitation, this chapter investigated the proposed wave-energy capture platform under WCI, focusing on its dynamic responses and captured power under different current directions and velocities. Since WCI is a common physical phenomenon in marine environments, this work provides useful references for the design and performance assessment of similar offshore structures.

Chapter 5

The floating wave-energy harvesting platform under combined short-crested waves and wave-current interaction

The focus of this chapter is to investigate the effects of the short-crestedness and current on the dynamic behavior of the floating wave-energy harvesting platform under both operational and severe conditions with WCI. Time-domain simulations are conducted to analyze the platform motion, mooring line tension and power absorption of this wave-energy capture system, which consider several factors such as the current velocity, current direction, and wave distribution. Additionally, the hydrodynamic stability of the platform under severe conditions is evaluated through the phase plots. The results demonstrate that the presence of current and short-crested characteristic can alter the wave excitation forces, which significantly affects the dynamic response and power capture of this harvesting system. Given that the WCI and multidirectional wave propagation are commonly encountered in marine environments, both factors should be taken into account in the design and performance evaluation of this type of offshore structures.

5.1 Results and discussion

Under operational and severe conditions, the winds are assumed to be negligible, while only the irregular waves and currents are considered. For operational sea states at the selected site, the typical current velocity ranges from 0.5 m/s to 0.7 m/s, while for severe sea states, the typical current velocity ranges from 0.9 m/s to 1.3 m/s [93]. In this study, the current velocities for the operational and severe conditions are assumed to be 0.5 m/s and 1 m/s, respectively. Meanwhile, the current incident direction includes 0° and 180°. As for the specific information for the considered ECs including the irregular wave parameters [93], they are presented in Table 5.1. It is notable that the incident angle for the long-crested waves and the mean incident angle for short-crested waves are both assumed to be 0°. Besides, for short-crested waves, the spreading exponent (n) is taken as a constant value of 2.

In the adopted directional spreading function, a smaller value of (n) corresponds to a broader directional distribution of wave energy, whereas a larger value indicates a more concentrated distribution approaching the long-crested wave condition. Therefore, the use of (n=2) provides a clear distinction between long-crested and short-crested wave conditions. This choice is also consistent with the

Table 5.1: Operational and severe conditions (SCW: Short-crested wave; LCW: Long-crested wave).

Operational conditions	H_s (m)	T_p (s)	γ	Wave category	u (m/s)
LC1-1-S	3.8	8.3	2.4	SCW	-0.5
LC1-1-L	3.8	8.3	2.4	LCW	-0.5
LC1-2-S	3.8	8.3	2.4	SCW	0
LC1-2-L	3.8	8.3	2.4	LCW	0
LC1-3-S	3.8	8.3	2.4	SCW	0.5
LC1-3-L	3.8	8.3	2.4	LCW	0.5
Severe conditions	H_s (m)	T_p (s)	γ	Wave category	u (m/s)
LC2-1-S	8.3	11.4	3.1	SCW	-1
LC2-1-L	8.3	11.4	3.1	LCW	-1
LC2-2-S	8.3	11.4	3.1	SCW	0
LC2-2-L	8.3	11.4	3.1	LCW	0
LC2-3-S	8.3	11.4	3.1	SCW	1
LC2-3-L	8.3	11.4	3.1	LCW	1

objective of the present study, as it allows the influence of short-crestedness on the performance of the proposed wave-energy capture system to be more clearly evaluated. Furthermore, WCI is a common phenomenon in real marine environments and may substantially modify the hydrodynamic loads acting on offshore structures. Accordingly, incorporating WCI into the analysis is essential for achieving a more reliable design and performance assessment of the proposed wave-energy harvesting system.

For long-crested waves under WCI, the spectral model introduced in Chapter 2 is adopted, and its reliability has been verified in Chapter 4. The same spectral modelling framework can also be extended to short-crested waves under WCI. In order to ensure energy consistency between long-crested and short-crested waves, the long-crested wave spectrum considering WCI is used as the frequency-spectrum component in the short-crested wave-spectrum model. Although this procedure enables a controlled comparison between long-crested and short-crested wave cases, it is an engineering approximation. Therefore, the development and verification of a direction-dependent WCI spectral model for short-crested waves is recommended for future research.

Each time-domain simulation is conducted over a total duration of 4100 s. The Cummins equation of motion is solved using a time step of 0.1 s, while the mooring-line dynamics are resolved with a finer time step of 0.01 s. To minimise the influence of initial transient effects, the first 500 s of each simulated time history are excluded. For the response spectra of the platform motion and mooring line tension, they are obtained by applying the fast Fourier transform (FFT) to the corresponding time histories of the dynamic responses.

5.1.1 Determination of PTO damping coefficients

Under operational conditions, the parametric studies are adopted to determine the optimal PTO damping coefficients for the WEC to absorb the most power, as shown in Figure 5.1. It is observed that at each current velocity, the most power captured by the WEC under long-crested waves is much larger than that under short-crested waves. Additionally, the optimal PTO damping coefficient (5.06×10^4) under long-crested waves is higher than that (4.7×10^4) under short-crested waves. Furthermore, the most power absorbed by the WEC decreases as the current velocity ranges from -0.5 to 0.5 m/s, while the optimal PTO damping remains unchanged. In the subsequent analysis, the PTO damping coefficients of the WECs under short- and long-crested waves are set as 4.7×10^4 and 5.06×10^4 kN·m·s/rad, respectively.

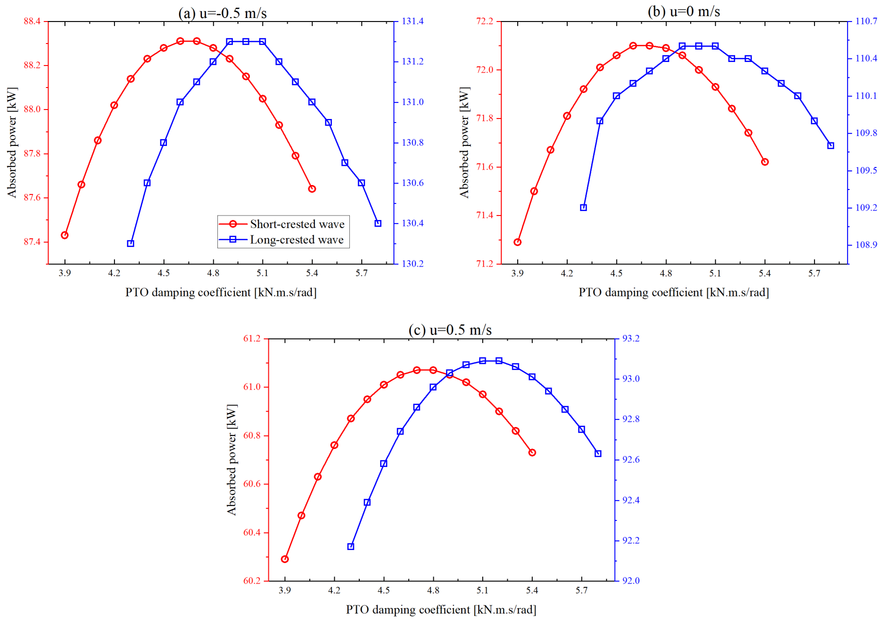

Figure 5.1: Power absorption of the WEC with different PTO damping coefficients under various operational conditions.

5.1.2 Wave excitation forces and moments acting on the platform

Figures 5.2 and 5.3 illustrate the responses of the surge, heave and pitch wave excitation forces and moments of the platform under operational and severe conditions. From these figures, it can be observed that the wave forces and moments are larger under long-crested waves than under short-crested waves. This is because the energy of long-crested waves is more focused compared to short-crested waves. Additionally, it is obvious that the average values of the first-order wave force and moment responses are nearly zero.

In Figure 5.2, the STDs of the first-order, and the mean values and STDs of second-order wave forces and moments exhibit a downward trend as the current speed varies from -0.5 to 0.5 m/s. This indicates that under operational conditions, the opposing currents increase the first-order and second-order wave forces and moments, while the following currents have the opposite effects.

Figure 5.3 shows that for the surge and heave DoFs, the STDs of the first-order wave forces under both long-crested and short-crested wave conditions decrease as the current speed varies from -1 to 1 m/s, as well as the STD of the pitch first-order wave moment in long-crested waves. Regarding the STD of the pitch first-order wave moment under short-crested wave conditions, it is larger at u = 0 m/s than at u = -0.5 m/s and 0.5 m/s. These phenomena indicate that under severe conditions, the surge and heave first-order wave forces increase under the opposing currents, while the following currents have the opposite effects. Furthermore, the presence of the currents reduces the pitch first-order wave moments.

It is also observed from Figure 5.3 that the heave second-order wave force response decreases gradually as the current speed varies from -1 to 1 m/s. Similarly, the pitch second-order wave moment response under long-crested waves follows the same trend as that for the heave DoF. Additionally, the mean value of surge second-order wave forces in both long-crested and short-crested waves decreases under the opposing currents, while for the pitch DoF in short-crested waves, the opposing currents slightly reduce the STD of its second-order wave forces. This implies that under severe conditions, the opposing currents reduce the surge mean drift forces under both long-crested and short-crested wave conditions and the pitch slow drift moments under short-crested wave conditions.

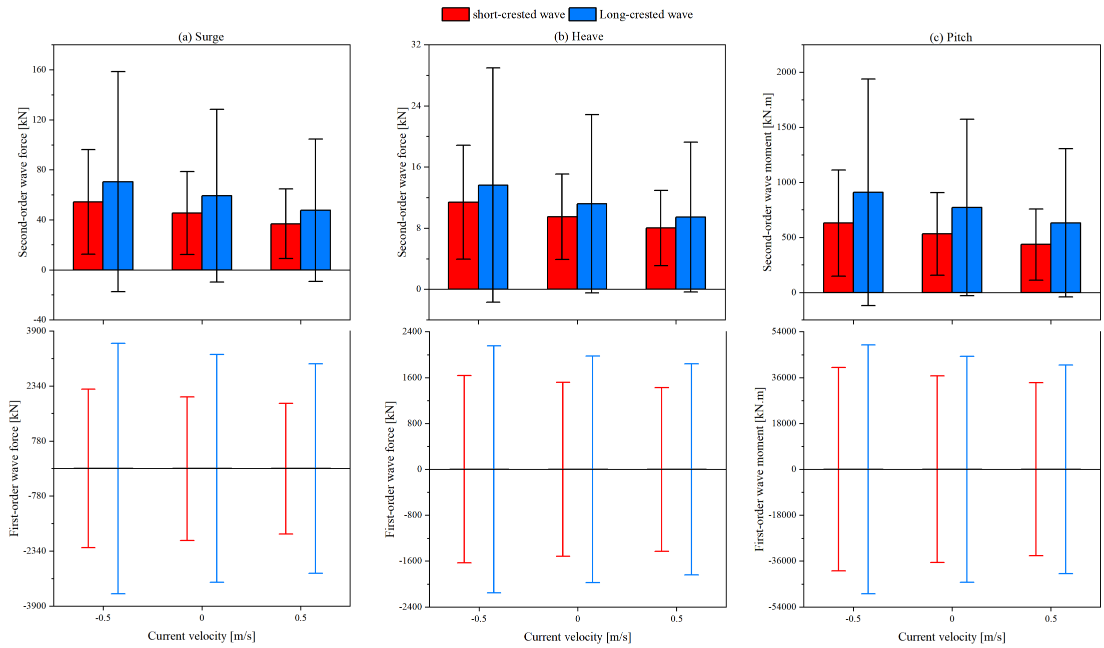

Figure 5.2: Surge (a), heave (b) and pitch (c) wave forces and moments under various operational conditions.

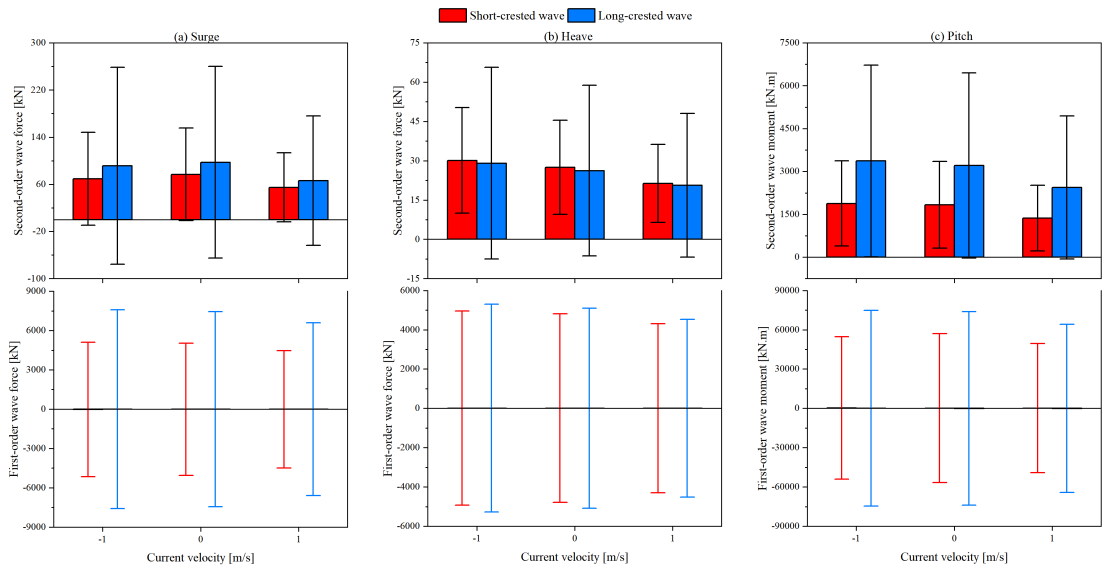

Figure 5.3: Surge (a), heave (b) and pitch (c) wave forces and moments under various severe conditions.

5.1.3 Platform motion

Motion response

Figures 5.4 and 5.5 respectively present the surge, heave, and pitch responses of the platform under operational and severe conditions. From these two figures, it can be found that the heave response in short-crested waves is smaller than that under long-crested waves. This is because the heave wave excitation forces are larger in long-crested waves. Besides, the opposing currents increase the heave response, whereas the following currents have the opposite effects.

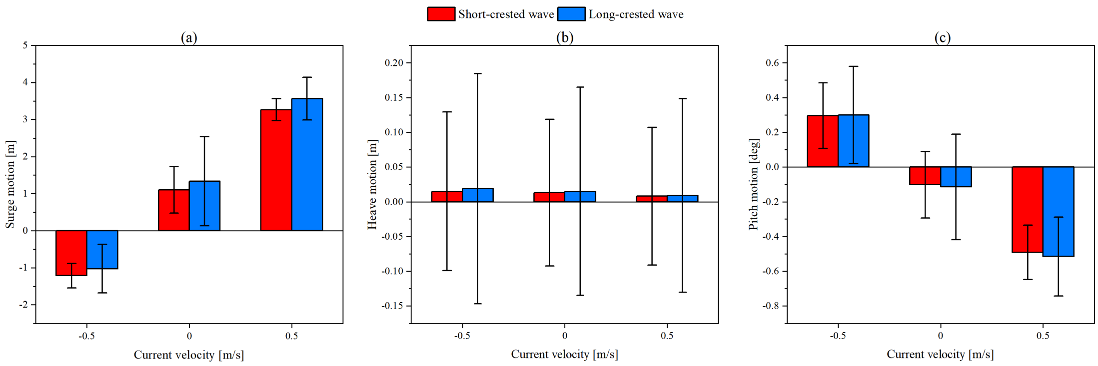

Figure 5.4: Surge (a), heave (b) and pitch (c) mean values and STDs under different operational conditions.

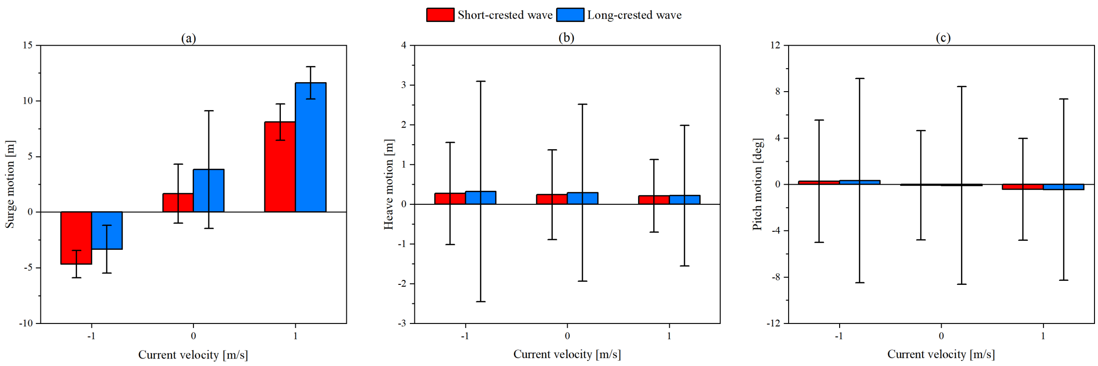

Figure 5.5: Surge (a), heave (b) and pitch (c) mean values and STDs under different severe conditions.

Under both operational and severe conditions, the surge mean response under the opposing currents is negative. This indicates that for the surge, the excitation of the opposing currents is stronger than the second-order mean drift forces. Meanwhile, the surge mean value with the following currents is much larger than that without the currents, suggesting that, although the following currents reduce the mean drift forces, the current loads are the dominant factor determining the surge equilibrium position. Furthermore, the difference in the surge mean response between short- and long-crested waves is due to the variation in the mean drift forces.

As seen in Figure 5.4, the positive pitch mean values are observed under the opposing currents. This is attributed to the fact that the current-induced excitation exceeds the contribution from the mean drift moment. Meanwhile, the mean pitch response under long-crested waves is almost identical to that under short-crested waves. Under the no-current and following-current conditions, the pitch mean response is larger for long-crested waves than for short-crested waves, owing to the larger mean drift moment induced by long-crested waves. In addition, although the following current reduces the mean drift moment, the pitch mean response under the following currents remains significantly larger than that without the currents. This indicates that the current plays a dominant role in determining the pitch equilibrium position.

It is observed in Figure 5.4 that the STDs of the surge and pitch responses without the currents are larger than those with the opposing currents. However, the first-order and slow drift wave forces and moments for these two DoFs are smaller under the opposing currents. Thus, it can be inferred that the current loads exhibit the damping effects under operational conditions. Moreover, compared to long-crested waves, the STDs of the surge and pitch responses are smaller under short-crested waves, which is due to the larger excitation under long-crested waves.

Figure 5.5 exhibits that the surge STD with the opposing currents is smaller than that without the currents, implying that the current loads also act as a damping role under severe conditions. However, when the waves and currents are aligned, the STD of the surge response under short-crested waves is larger than that under long-crested waves. It is due to the fact that the surge mean displacement is larger under long-crested waves, leading to an increase in its restoring stiffness. Regarding the pitch STD, its variation trends across different wave and current conditions are similar to those of the heave response

Motion response spectrum

Figures 5.6-5.7 respectively illustrate the surge, heave and pitch motion response spectra of the platform under operational and severe conditions. From these two figures, it is evident that the surge response comprises both LF and WF components. Although the bandwidth of the LF region is narrower than that of the WF region, the spectral values in the LF region are much larger.

Under operational conditions, the surge response under short-crested waves is smaller than that under long-crested waves. Furthermore, under severe conditions, when the waves and currents are aligned, the surge LF response under short-crested waves is slightly larger than that under long-crested waves. Furthermore, the surge LF response without the currents is significantly larger than that with the currents. For the heave DoF, the WF component dominates its response. Besides, the heave response under short-crested waves is smaller than that under

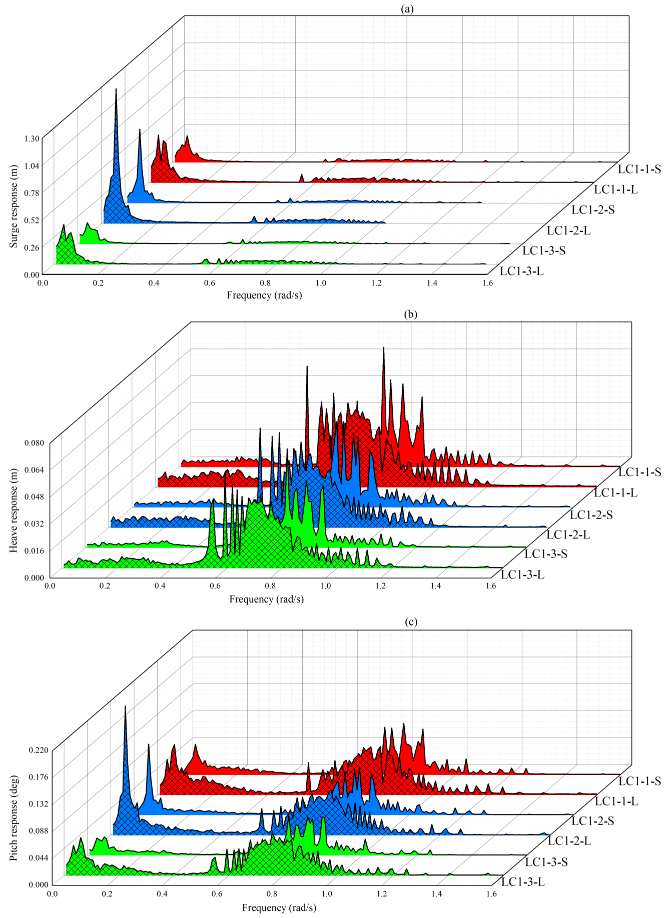

Figure 5.6: Surge (a), heave (b) and pitch (c) motion response spectra under various operational conditions.

long-crested waves. Additionally, the heave response exhibits a decreasing trend across u=-0.5-0.5 m/s.

As shown in Figure 5.6, under operational conditions, unlike the surge response, the pitch WF response is larger than its LF response. However, due to the surge-pitch coupling effects, the LF response also makes a significant contribution to the pitch DoF. In addition, the variation trends of the pitch LF and WF responses under different wave and current conditions are similar to those of the surge LF response and heave WF response, respectively. Figure 5.7 reveals

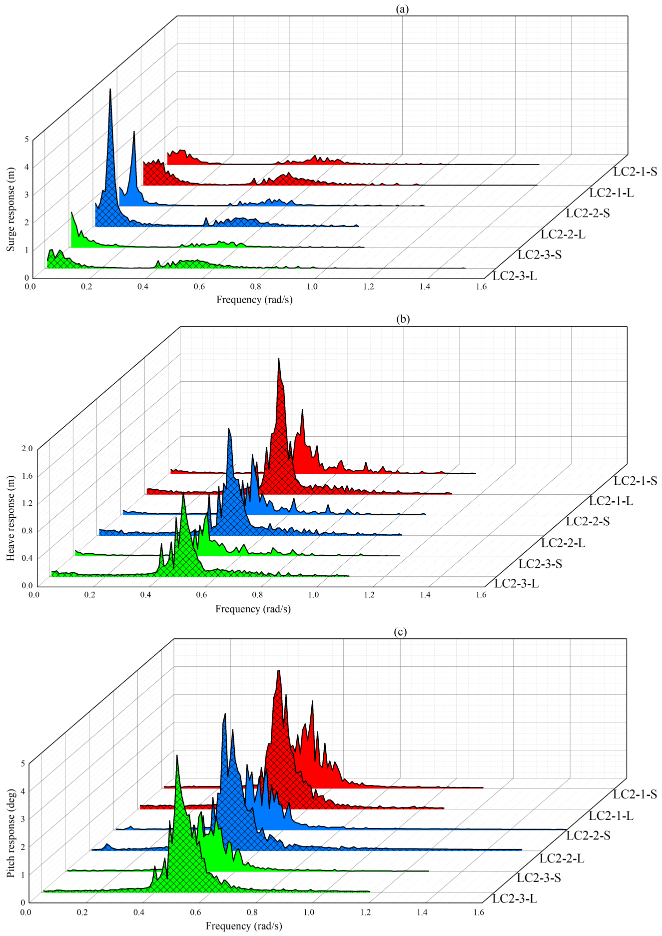

Figure 5.7: Surge (a), heave (b) and pitch (c) motion response spectra under various severe conditions.

that, under severe conditions, the WF response dominates the pitch DoF, which is distinct from the operational conditions. Besides, similar to the surge and heave WF responses, the pitch WF response under short-crested waves is smaller than that under long-crested waves.

Motion significant amplitude

To further investigate the platform motion characteristics, Figures 5.8 and 5.9 respectively present the surge, heave and pitch SAs within the LF and WF regions

(0 - 0.2 rad/s and 0.2 - 2 rad/s) under operational and severe conditions. The formula for calculating the SA of the motion response is given in Eq. (4.1).

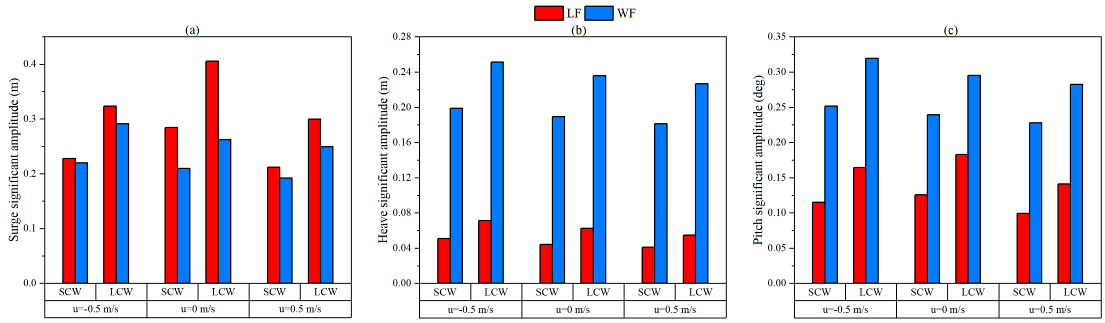

Figure 5.8: Surge (a), heave (b) and pitch (c) SAs within the LF and WF regions under different operational conditions.

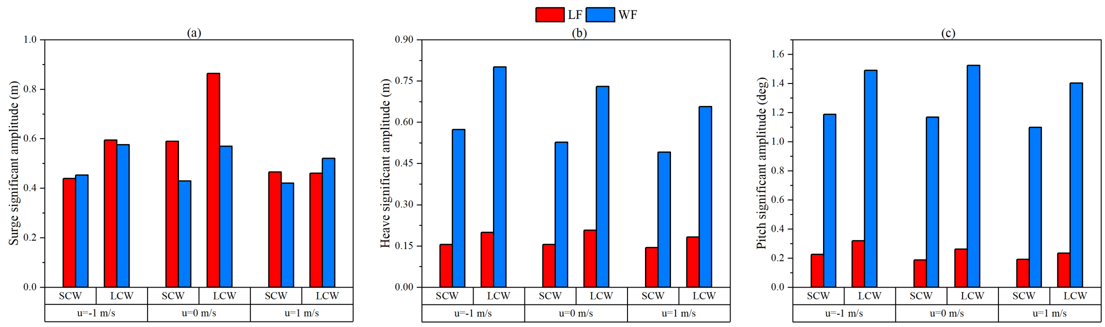

Figure 5.9: Surge (a), heave (b) and pitch (c) SAs within the LF and WF regions under different severe conditions.

From Figures 5.8 and 5.9, it can be observed that the surge WF SA exhibits a downward trend across the current velocity range (u=-0.5-0.5 m/s). In addition, short of the damping effects, the surge LF SA is the largest without the currents. Under operational conditions, the surge SAs in short-crested waves are smaller than those in long-crested waves. However, it is worth noting that, under severe conditions, when the waves and currents are aligned, the surge LF SA under short-crested waves is larger than that under long-crested waves. This is attributed to the stronger damping effects of the currents under long-crested waves. Furthermore, under LC2-1-S and LC2-3-L, the WF SA of the surge is larger than its LF SA. Similar to the surge WF SA, the heave SA under operational conditions exhibits a decreasing trend across this current velocity range. Besides, under severe conditions, the heave LF SA under long-crested waves is the largest without the currents. This phenomenon can also be attributed to the damping effects of the currents.

As for the pitch DoF, under operational conditions, its WF SA also shows a decreasing trend across the current velocity range (u=-0.5-0.5 m/s). Besides, under severe conditions, the pitch WF SAs under short-crested waves show a similar trend across this current velocity range. However, short of the damping effects, the pitch WF SA under long-crested waves reach its maximum without the currents. Additionally, compared to severe conditions, the difference between the pitch WF and LF SAs is significantly smaller under operational conditions. This implies that, as the external forces increase, the sensitivity of the WF response becomes more pronounced. It is notable that, under both operational and severe conditions, the SAs of the heave and pitch under short-crested waves are smaller than those under long-crested waves. This is attributed to the stronger excitation associated with long-crested waves.

Furthermore, it can be noticed from Figure 5.8 that, the pitch LF SA with the currents is smaller than that without the currents, which is due to the damping effects of the currents. Figure 5.9 shows that, under long-crested waves, the pitch LF SA exhibits a decreasing trend across the current velocity range (u=-1-1 m/s). This indicates that the damping effects of the opposing currents are weaker than the excitation of the second-order wave moments. However, under short-crested waves, the pitch LF SA with the currents is larger than that without the currents.

This phenomenon implies that the currents do not exhibit the damping effects but the amplifying effects.

Motion phase Characteristics

Under severe conditions, the motion phase plots of the platform can be used to evaluate its dynamic stability. A smaller and more compact phase trajectory generally indicates better stability, whereas a larger and more scattered phase trajectory suggests poorer stability [95]. Figure 5.10 shows the surge, heave and pitch motion phase plots under severe conditions.

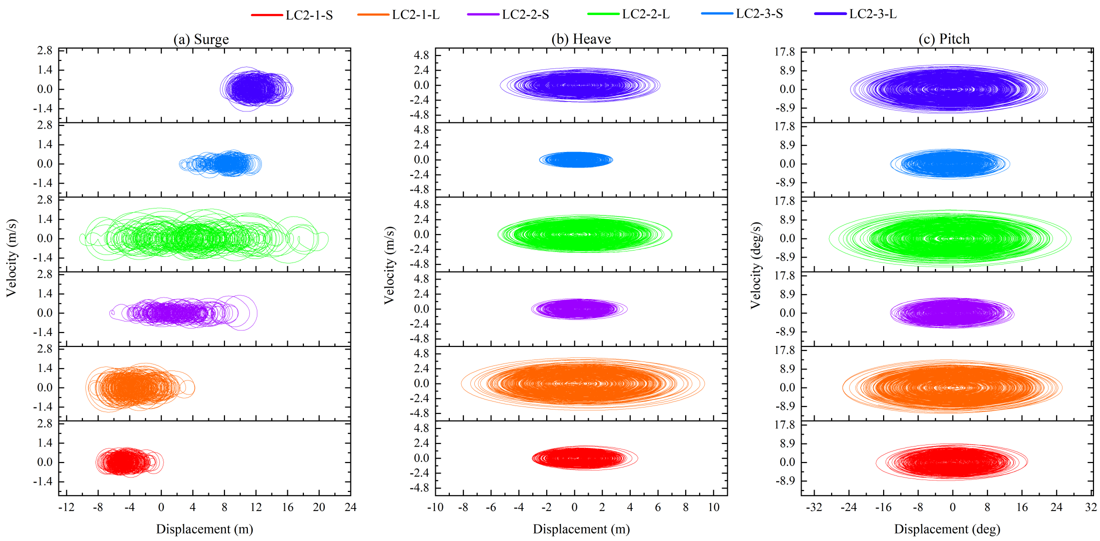

Figure 5.10: Surge (a), heave (b) and pitch (c) motion phase plots under various severe conditions.

In Figure 5.10(a), it is obvious that the surge phase plot is non-periodic. This is because both LF and WF components are prominent in the surge response, as seen in Figure 5.9(a). Notably, the stability of the surge is optimal under LC2-1-S and worst under LC2-2-L. Under LC2-2-L, the surge phase plot exhibits a large span in the displacement and velocity. This is because, under this condition, the damping effects are absent, and the excitation from long-crested waves is stronger.

It is shown in Figure 5.10(b) that the stability of the heave under short-crested waves is better than that under long-crested waves. Besides, the stability of the heave gradually weakens within the current velocity range of u=-1-1 m/s. These phenomena can be explained by the variation trends of wave excitation forces across this current velcocity. Unlike the surge motion, the heave motion is mainly dominated by the wave-frequency (WF) response, as shown in Figure 5.9(b), and therefore its phase plot remains much closer to harmonic-like closed orbits.

Figure 5.10(c) demonstrates that, under short-crested waves, the stability of the pitch exhibits the same trend across u=-1-1 m/s with the heave stability. Besides, under long-crested waves, the stability of the pitch is weaker without the currents than with the currents. Similar to the stability of the surge under LC2-2-L, this phenomenon is caused by the damping effects of the currents. Additionally, similar to the heave motion, the WF component dominates the pitch response, as demonstrated in Figure 5.9(c). Consequently, its phase plot also exhibits harmonic-like features.

5.1.4 Mooring line tension

This section selects mooring lines #5 and #1 as the study objects, which are in the upstream and downstream directions, respectively.

Tension response

Figures 5.11 and 5.12 show the tension responses of #1 and #5 under operational and severe conditions, respectively. In Figure 5.11, it is observed that under operational conditions, the #1 mean tension response exhibits a decreasing trend across u= -0.5 to 0.5 m/s, and it is lower under long-crested waves than that under short-crested waves. However, for the #5 tension response, the opposite trend is observed. Additionally, under operational conditions, the STDs of the #1 and #5 tension responses are larger without the currents than those with the currents. Besides, their STDs are larger under long-crested waves than under short-crested waves. The above phenomena are closely related to the variation trends of the surge response under different wave and current conditions, as the surge DoF directly affects the suspended length of the mooring lines, thereby influencing the resulting mooring tension. Based on the analysis of the surge response in Figure 5.4(a), the variation trends of #1 and #5 tension responses can be inferred.

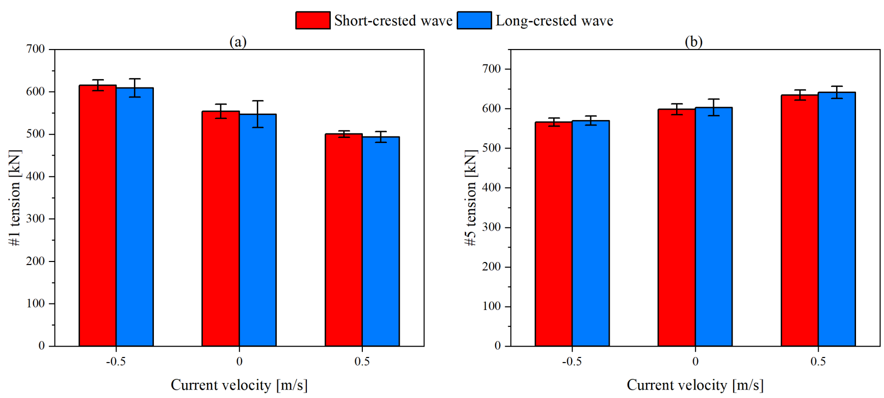

Figure 5.11: Mean values and STDs of the #1 (a) and #5 (b) tension responses under different operational conditions.

Figure 5.12 demonstrates that under severe conditions, the mean tension responses of #1 and #5 exhibit a decreasing and increasing trend across u= -1 to 1 m/s, respectively, which is similar to that observed in Figure 5.11. When u= -1 and 0 m/s, the #1 mean tension response under short-crested waves is smaller than that under long-crested waves. Besides, when u= -1 m/s, the #5 mean tension response under long-crested waves is smaller than that under short-crested waves. This is because, under severe conditions, the heave and pitch mean responses of the platform also begin to affect the suspension length of the mooring lines, which is not solely determined by the surge mean response.

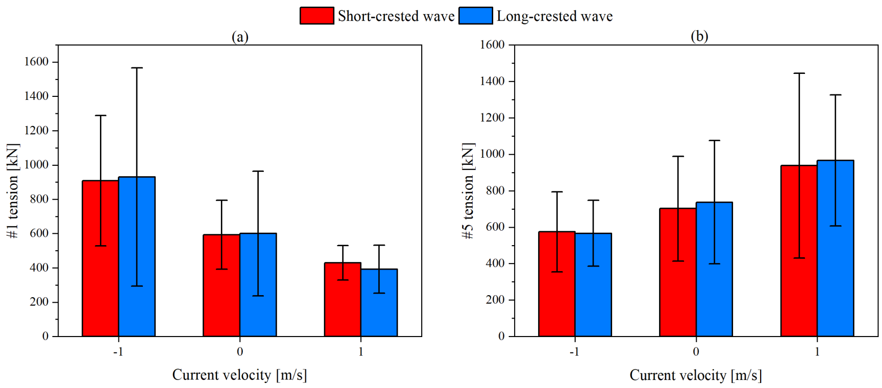

Figure 5.12: Mean values and STDs of the #1 (a) and #5 (b) tension responses under different severe conditions.

As for the STDs of the #1 and #5 tension responses under severe conditions, their variation trends across this current velocity range are different from those under operational conditions. The STD of #1 tension response shows a decreasing trend across u= -1 to 1 m/s, whereas for #5, the trend is the opposite. Furthermore, the STD #1 tension response is smaller under short-crested waves than under long-crested waves, while the opposite trend is observed for #5. These phenomena can be attributed to the effects of the suspended length variation on the restoring stiffness of the mooring lines. A larger suspended length leads to higher restoring stiffness, thereby suppressing the oscillations of the tension response.

Tension response spectrum

Figures 5.13 and 5.14 exhibit the #1 and #5 tension response spectra under operational and severe conditions, respectively. In Figure 5.13, it is obvious that under operational conditions, the tension response consists of the LF and WF components. For the LF response, it is smaller in the presence of currents, compared to the absence of currents, which indicates that the currents play a damping role in suppressing the LF response. Additionally, the #1 WF tension response shows a decreasing trend across u=-0.5-0.5 m/s, while for #5, the opposite trend is observed. Notably, the #1 tension response under short-crested waves is generally smaller than that under long-crested waves.

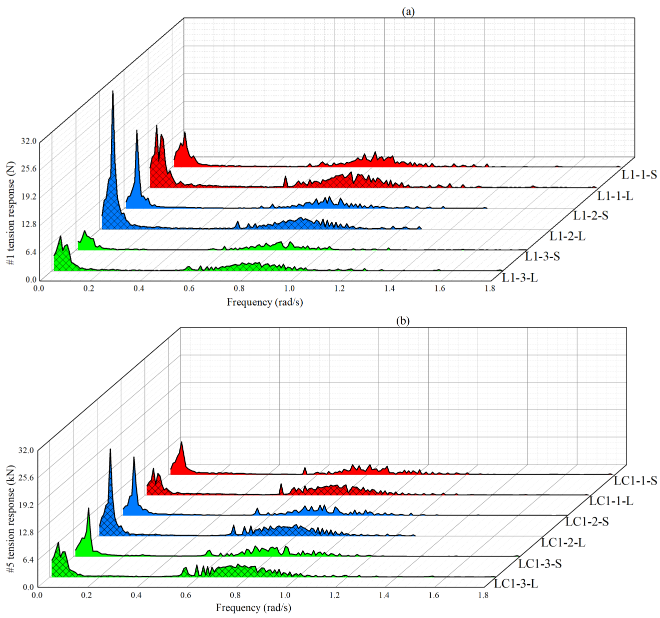

Figure 5.13: Tension response spectra of #1 (a) and #5 (b) under different operational conditions.

Figure 5.14 indicates that under severe conditions, the tension response consists of LF, WF and high-frequency (HF) components. Compared to u= -1 m/s and 0 m/s, the #1 LF tension response is significantly small at u= 1 m/s. This implies that, at this current velocity, the second-order drift forces exhibit a relatively weak excitation on the #1 tension. For the #5 LF tension response, under short-crested waves, it shows an increasing trend across u= -1 to 1 m/s. Besides, under long-crested waves, it is smaller with the currents than without the currents. Notably, in the presence of currents, the #5 LF tension response under long-crested waves is smaller than that under short-crested waves. This phenomenon indicates that the damping effects induced by the currents suppress the excitation associated with the second-order drift forces.

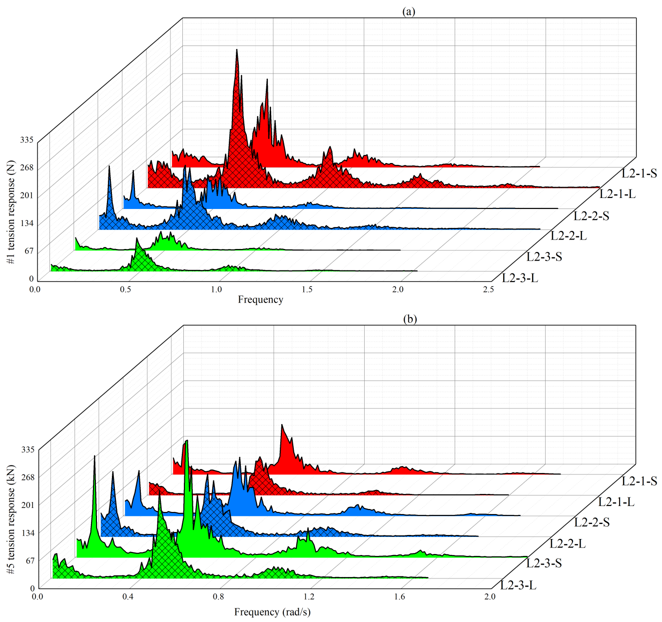

Figure 5.14: Tension response spectra of #1 (a) and #5 (b) under different severe conditions.

Furthermore, under severe conditions, the variation trends of the #1 and #5 WF tension responses across u= -1 - 1 m/s are similar to those observed under operational conditions. The #1 WF tension response is significantly smaller under short-crested waves than under long-crested waves. It is also noteworthy that, HF components are induced in the #1 and #5 tension responses by the external excitation, which is not observed under operational conditions. Interestingly, the variation trend of the double-frequency component of the #1 tension regarding different wave and current conditions follows the same trend as that of its WF component, which is also observed for #5. Moreover, for the tension response, the components at the frequencies higher than the double-frequency are relatively small.

Tension Significant amplitude

To further investigate the tension characteristics, Figures 5.15 and 5.16 show the tension LF (0 - 0.2 rad/s) and WF (0.2 - 2 rad/s) SAs of the #1 and #5 under operational and severe conditions, respectively. The calculation formula for the tension SA is identical with Eq. (4.1).

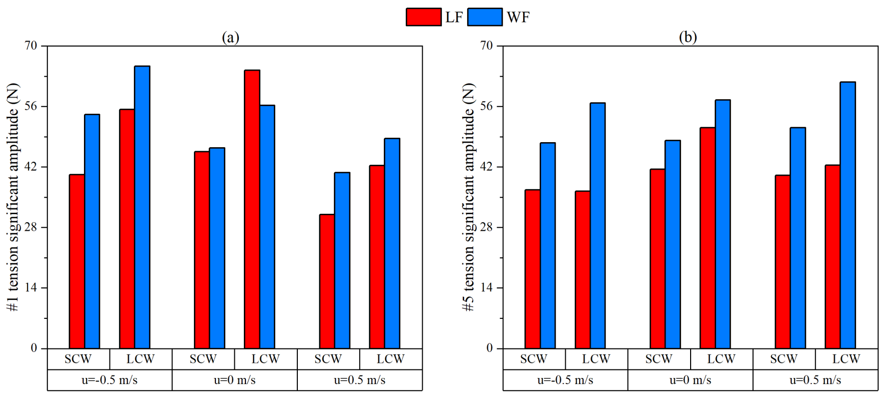

Figure 5.15: LF and WF SAs of the #1 (a) and #5 (b) tension responses under different operational conditions.

In Figure 5.15, under operational conditions, it can be observed that the WF SA of the #1 tension response exhibits a downward trend across u= -0.5-0.5 m/s, while the situation for #5 is the opposite. Additionally, for the LF SAs of the #1 and #5 tension responses, they are larger in the absence of currents than in the presence of currents, which can be attributed to the damping effects. Furthermore, the SAs of the #1 and #5 tension responses under short-crested waves exhibit smaller than those under long-crested waves.

Figure 5.16 shows that under severe conditions, the variation trends of the WF SAs of the #1 and #5 tension responses across u= -1-1 m/s are similar to those observed under operational conditions. Additionally, the LF SA of the #1 tension response exhibits a downward trend across this current velocity range, while for #5 under short-crested waves, the opposite trend is observed. Notably, due to the damping effects, the LF SA of the #5 tension response under long-crested waves is smaller with the currents than that without the currents. Furthermore, with the currents, the SA of the #5 tension under long-crested waves is smaller than that under short-crested waves, suggesting that the damping effects of the currents are significantly weaker under short-crested waves than under long-crested waves.

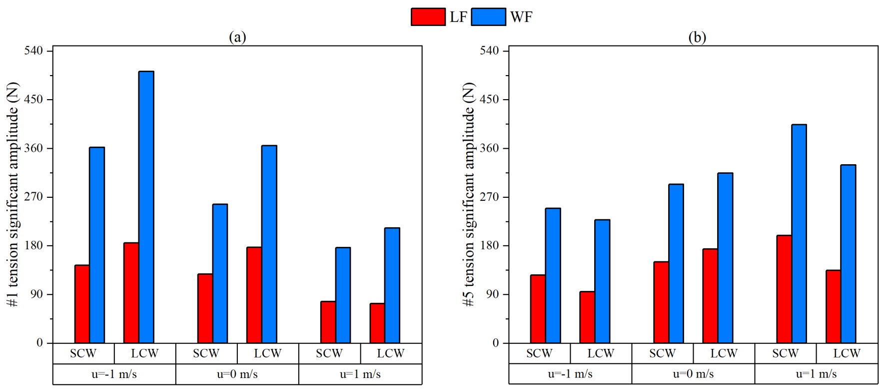

Figure 5.16: LF and WF SAs of the #1 (a) and #5 (b) tension responses under different severe conditions.

Figures 5.15 and 5.16 also reveal that, except for LC1-2-L, under all other operational and severe conditions, the LF SAs of the #1 and #5 tension responses are smaller than their WF SAs. This implies that, except for LC1-2-L, the WF component dominates the tension response under other ECs. Additionally, under severe conditions, the difference between the tension WF and LF SAs is significantly larger than that under operational conditions. This can be attributed to the fact that the first-order wave excitation is significantly enhanced under severe conditions, leading to a more pronounced WF tension response. Although the second-order drift force also increases, which is closely related to the LF tension response, its contribution is insufficient to overcome the limiting effects imposed by the mooring restoring characteristics and current-induced damping. Consequently, the WF tension component increases more significantly than the LF component under severe conditions.

5.1.5 Power capture performance

This section explores the power capture of the individual WEC, WEC row, and WEC array under different operational conditions. For the individual WEC, WECs 1-3 and WECs 8-9 are considered, while for the WEC row, Rows 1 and 3 are selected.

Figure 5.17 presents the power output of the individual WECs under various operational conditions. It is found that the power output of each WEC exhibits a downward trend across u=-0.5-0.5 m/s. Additionally, except for WEC 1, the absorbed power of other WECs is less under short-crested waves than under long-crested waves. As for WEC 1, its absorbed power is almost unaffected by the wave distribution. Furthermore, among different operational conditions, WEC 9 absorbs the most power. Besides, WECs 8 and 2 absorb the least power under short-crested and long-crested waves, respectively.

Since the PTO devices are driven by the vertical motion between the platform

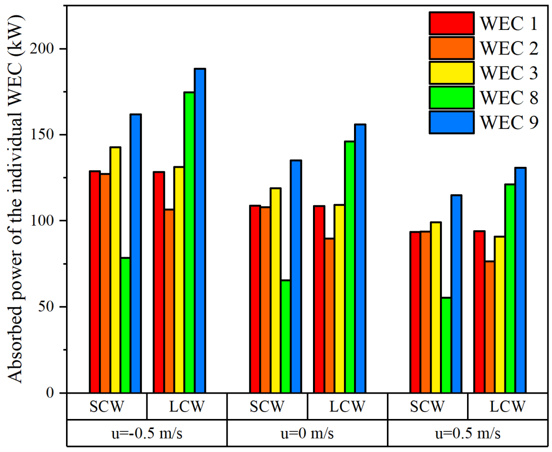

Figure 5.17: Power output of the individual WECs under various operational conditions.

and WECs, the relative heave response of WEC 8 is used to explore the features of its power absorption, as demonstrated in Figure 5.18. This figure shows that the heave relative response is smaller under short-crested waves than under long-crested waves, and it also exhibits a downward trend across u=-0.5-0.5 m/s. These variation patterns of the relative heave response align with those of the absorbed power of WEC 8 under various operational conditions.

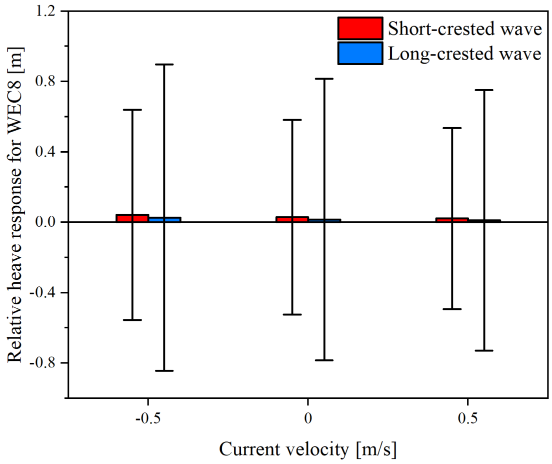

Figure 5.18: Mean values and STDs of the relative heave response between the platform and WEC8 under various operational conditions.

Figure 5.19 gives the absorbed power of Rows 1 and 3 under different operational conditions. The power absorption of the WEC rows exhibits a downward trend across u=-0.5-0.5 m/s. Notably, Row 1 absorbs more power under short-crested waves than under long-crested waves, whereas Row 3 exhibits the opposite trend. Additionally, the captured power of Rows 1 and 3 is nearly identical under short-crested waves, while under long-crested waves, Row 3 captures significantly more power than Row 1.

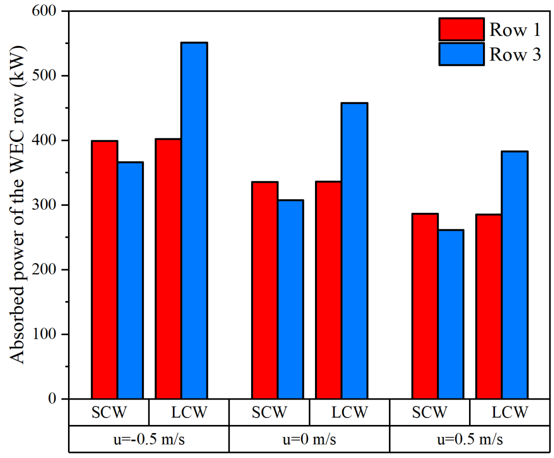

Figure 5.19: Power output of the WEC rows under various operational conditions.

Figure 5.20 shows the captured power of the WEC array under different operational conditions. It can be seen that the power captured by the WEC array also exhibits a downward trend across u=-0.5-0.5 m/s, and its power capture performance under long-crested waves is superior to that under short-crested waves.

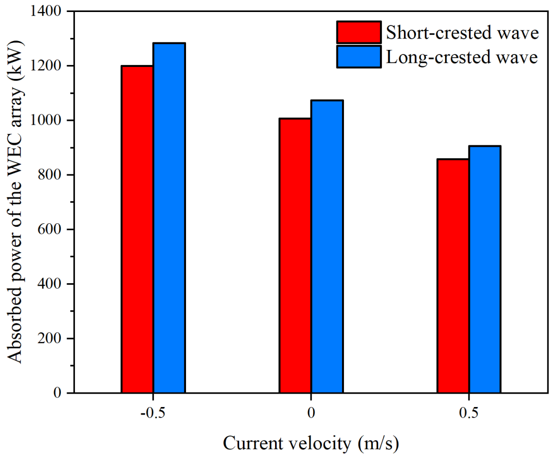

Figure 5.20: Power output of the WEC array under various operational conditions.

5.2 Summary

This chapter investigates the dynamic responses and power capture characteristics of the floating wave-energy harvesting platform under operational and severe conditions with WCI. A couple of time-domain simulations are carried out to explore the influence of short-crestedness and currents on the platform, mooring line tension, and the power absorption of this wave-energy capture system. For the current conditions, different current directions and velocities are considered. According to the results, some key findings are presented as follows:

(1)Under operational conditions, the surge, heave and pitch wave forces and moments on the platform exhibit a downward trend across u=-0.5-0.5 m/s, and they are smaller under short-crested waves than under long-crested waves. However, under severe conditions, the pitch wave moments and the surge second-order wave forces exhibit different trends from those observed under operational conditions due to the WCI.

(2)Due to the damping effects, the surge and pitch STDs are larger with no currents than with the currents under operational conditions. Besides, the heave STD exhibits a downward trend across u=-0.5-0.5 m/s. Under severe conditions, the surge STD is also larger without the currents than with the currents. Additionally, the heave and pitch responses under severe conditions exhibit the same variation trends across u=-0.5-0.5 m/s as the heave response under operational conditions. Furthermore, the platform motion responses are generally smaller under short-crested waves than under long-crested waves.

(3)Under both operational and severe conditions, the #1 mean tension value exhibits a downward trend across the considered current velocity ranges, while for #5, the opposite trend is observed. Additionally, under operational conditions, the tension STDs of #1 and #5 are smaller in the presence of currents due to the damping effects. Under severe conditions, the STDs of #1 and #5 tension show similar variation trends to their mean values across u=-1-1 m/s. Furthermore, under operational conditions, the tension responses of #1 and #5 are generally smaller in short-crested waves than in long-crested waves, while under severe conditions, the situation is reversed for #5 in the presence of currents.

(4)The power capture of the individual WEC, WEC rows, and WEC arrays under operational conditions exhibits a weakening trend across u=-0.5-0.5 m/s. In addition, the power output of the individual WECs, Row 3, and WEC array is higher under long-crested waves than under short-crested waves, while for Row 1, the situation is reversed.

Although extensive research has been carried out on wave-energy capture systems subjected to irregular waves and currents, the combined influence of short-crested waves and WCI on the performance of such energy-harvesting systems has not been sufficiently investigated. Therefore, this chapter examines the proposed wave-energy capture platform under short-crested waves with WCI, focusing on its dynamic responses and power-capture characteristics under different current conditions. Given that multidirectional wave propagation and WCI are frequently encountered in real ocean environments, this study provides useful insights for the engineering design and performance evaluation of this type of offshore structure.

Chapter 6

Conclusions and Future research

6.1 Conclusions

This thesis proposes a new floating wave-energy harvesting platform that integrates a SPIC semi-submersible platform with an array of point-absorber WECs, which provides another promising choice for the development of wave energy. Owing to the limitations of existing potential-flow-based commercial software in simulating WCI and multi-body connections, a coupled hydro-connected-mooring dynamic model is established based on 3D potential flow theory, the Lagrange multiplier technique, and the lumped-mass method.

For complex multi-body connected systems, the developed model can achieve the constraint relationships in a more straightforward manner through the Lagrange multiplier method, avoiding the need for complicated mechanical derivations and secondary development within the interfaces of commercial software. In addition, this model facilitates the investigation of various models for simulation of complex ECs on the performance of multi-body connected systems. For instance, the spectral model with WCI effects, as considered in this thesis, can be conveniently implemented within the present framework, whereas such modelling generally cannot be directly achieved using commercial software without secondary development.

Although extensive research has been carried out on wave-energy capture systems subjected to irregular waves, and combined irregular waves and currents, the influence of short-crestedness and WCI on the performance of such offshore structures has not been sufficiently investigated. Given that multidirectional wave propagation and WCI are frequently encountered in real ocean environments, this thesis investigates these two factors on the dynamic responses and power capture characteristics of the proposed wave-energy capture platform under the corresponding ECs. Following the verifications of the established dynamic model and the associated wave models, a series of time-domain simulations are carried out. Based on the results, some key conclusions are summarised as follows:

(1) Chapter 3 investigates the influence of wave directional spreading on the performance of the proposed wave-energy harvesting system under both operational and severe conditions. Although the wave energy of short-crested waves becomes increasingly concentrated around the mean incident direction as the spreading exponent increases, the platform motion response and mooring line tension response do not increase as expected. Besides, their variation trends across the spreading exponent differ among theses ECs. These phenomena can be attributed to the fact that this harvesting system is a complex multi-body connected system, in which the platform motions and mooring line tension are affected not only by the corresponding wave forces, but also by multi-body hydrodynamic interactions and hinge constraint forces.

In addition, the power absorbed by the WEC array shows a slight decreasing trend with increasing spreading exponent under mild operational condition, whereas it remains almost unchanged under moderate operational conditions.

(2)Chapter 4 investigates the influence of WCI on the dynamic responses and power-capture characteristics of this wave-energy harvesting system under operational conditions. The results show that the current has a damping effect on the LF surge and pitch responses of the platform, while it amplifies the WF surge response. When WCI is not considered, the heave response and the WF pitch response remain almost unchanged with variations in current velocity. However, after incorporating WCI, both responses become larger under opposing-current conditions than under following-current conditions.

For the mooring system, the LF tension response is reduced due to the damping effect of the current, whereas the WF tension response of the downstream line is amplified. Besides, the WF tension response of the upstream line is larger under following currents than under opposing currents.

In terms of power capture, the absorbed power of individual WECs, WEC rows, and the entire WEC array is almost unaffected by current velocity without WCI. Once WCI is considered, however, the power-capture performance is enhanced under opposing currents compared with following currents.

(3)Chapter 5 investigates the effects of short-crestedness and currents on the dynamic behavior and power capture performance of this wave-energy harvesting system under both operational and severe conditions with WCI. For the platform motions, the results show that, under operational conditions, the STDs of the surge and pitch responses are larger without the currents than with the currents, owing to the damping effects of the current. The heave STD is larger under opposing currents than under following currents. Under severe conditions, the surge STD also remains larger without currents than with currents, while the heave and pitch responses exhibit trends similar to those of the heave response under operational conditions. In general, the platform motion responses under short-crested waves are smaller than those under long-crested waves.

For the mooring system, under severe conditions, the tension response of the downstream line is larger under opposing currents than under following currents, whereas the opposite trend is observed for the upstream mooring line. Under operational conditions, the tension STDs of the mooring lines are reduced in the presence of currents due to the damping effects of the currents. Moreover, the mooring-line tension responses under operational conditions are generally smaller in short-crested waves than in long-crested waves. However, under severe conditions, this trend is reversed for the upstream line with the currents.

In terms of power capture, the individual WECs, WEC rows, and WEC array show better performance under opposing currents than under following currents under operational conditions. In addition, the power output of the individual WECs and the entire WEC array is higher under long-crested waves than under short-crested waves.

6.2 Future research

Although this thesis employs well-established theories and methodologies to conduct the coupled numerical simulations and analysis of the floating wave-energy harvesting platform, several limitations remain. They will be investigated in future research and include the following:

(1)In this thesis, the hydrodynamic coefficients, wave forces, and restoring stiffness are evaluated using the potential-flow BEM based on the mean wetted surface of the floating body. Future work should extend the present time-domain model by incorporating the effects of the instantaneous wetted surface, particularly for large-amplitude motions and extreme sea states.

(2)The PTO device is simplified as a hinged connection with rotational damping in this thesis. However, a practical PTO device is a relatively complex mechanical system. Therefore, a more detailed representation of its mechanical characteristics should be incorporated in future work, which would be beneficial for the practical design of this type of wave-energy harvesting systems.

(3)In this thesis, the short-crested directional spectrum under WCI is constructed by combining the WCI-modified long-crested wave spectrum with the directional spreading function. Although this treatment ensures that the total wave energy of the short-crested spectrum remains consistent with that of the corresponding long-crested spectrum, it is an engineering approximation. Therefore, future work should explore a fully direction-dependent WCI formulation for short-crested wave spectrum with current-induced modifications.

(4)Compared with numerical simulations, experimental investigations can provide additional insight into the physical characteristics of the proposed system, particularly those associated with nonlinear hydrodynamic effects, multi-body coupling, PTO dynamics, and mooring-line behavior. Therefore, future experimental studies would be valuable for further examining the dynamic responses and power capture of the proposed wave-energy harvesting platform.

Bibliography

[1] X. Shi, B. Liang, S. Du, Z. Shao, and S. Li, “Wave energy assessment in the china east adjacent seas based on a 25-year wave-current interaction numerical simulation,” *Renewable Energy*, vol. 199, pp. 1381–1407, 2022.

[2] Z. Zhang, L. Guan, H. Wu, L. Wu, W. Liu, and L. Cui, “Effects of the second-order hydrodynamics on the dynamic behavior of the platform among the wind-wave hybrid systems,” *Journal of Engineering Research*, vol. 13, no. 2, pp. 1603–1616, 2025.

[3] K. Gunn and C. Stock-Williams, “Quantifying the global wave power resource,” *Renewable Energy*, vol. 44, pp. 296–304, 2012.

[4] H. Nguyen, C. Wang, Z. Tay, and V. Luong, “Wave energy converter and large floating platform integration: A review,” *Ocean Engineering*, vol. 213, p. 107768, 2020.

[5] H. Wu and Z. Yuan, “Numerical investigation of the effects of short-crested irregular waves on the performance of a floating power capture platform,” *Ocean Engineering*, vol. 313, p. 119548, 2024.

[6] V. Sricharan and S. Chandrasekaran, "Time-domain analysis of a bean-shaped multi-body floating wave energy converter with a hydraulic power take-off using wec-sim," *Energy*, vol. 223, p. 119985, 2021.

[7] H. Zhang, B. Zhou, J. Zang, C. Vogel, P. Jin, and D. Ning, "Optimization of a three-dimensional hybrid system combining a floating breakwater and a wave energy converter array," *Energy Conversion and Management*, vol. 247, p. 114717, 2021.

[8] J. Hu, B. Zhou, C. Vogel, P. Liu, R. Willden, K. Sun, J. Zang, J. Geng, P. Jin, L. Cui, B. Jiang, and M. Collu, "Optimal design and performance analysis of a hybrid system combing a floating wind platform and wave energy converters," *Applied Energy*, vol. 269, p. 114998, 2020.

[9] Y. Si, Z. Chen, W. Zeng, J. Sun, D. Zhang, X. Ma, and P. Qian, "The influence of power-take-off control on the dynamic response and power output of combined semi-submersible floating wind turbine and point-absorber wave energy converters," *Ocean Engineering*, vol. 227, p. 108835, 2021.

[10] H. R. Ghafari, A. Neisi, H. Ghassemi, and M. Iranmanesh, "Power production of the hybrid wavestar point absorber mounted around the hywind spar platform and its dynamic response," *Journal of Renewable and Sustainable Energy*, vol. 13, no. 3, p. 033308, 2021.

[11] Y. Li and Y. H. Yu, "A synthesis of numerical methods for modeling wave energy converter-point absorbers," *Renewable and Sustainable Energy Reviews*, vol. 16, no. 6, pp. 4352–4364, 2012.

[12] O. Nwogu, "Analysis of fixed and floating structures in random multi-directional waves," Ph.D. dissertation, University of British Columbia, 1989.

[13] J. Park, Y. Uno, T. Sato, H. Miyata, and H. Chun, "Numerical reproduction of fully nonlinear multi-directional waves by a viscous 3d numerical wave tank," *Ocean Engineering*, vol. 31, no. 11, pp. 1549–1565, 2004.

[14] Z. Chen, J. Jiao, Y. Chen, C. Jiang, and S. Chen, "Influence of wave directional spreading of short-crested irregular waves on ship motions and wave loads," *Marine Structures*, vol. 103, p. 103825, 2025.

[15] N. E. Huang, D. T. Chen, C. C. Tung, and J. R. Smith, "Interactions between steady won-uniform currents and gravity waves with applications for current measurements," *Journal of Physical Oceanography*, vol. 2, no. 4, pp. 420 – 431, 1972.

[16] T. S. Hedges, K. Anastasiou, and D. Gabriel, "Interaction of random waves and currents," *Journal of Waterway, Port, Coastal, and Ocean Engineering*, vol. 111, no. 2, pp. 275–288, 1985.

[17] J. Dai, B. C. Abrahamsen, T. Viuff, and B. J. Leira, "Effect of wave-current interaction on a long fjord-crossing floating pontoon bridge," *Engineering Structures*, vol. 266, p. 114549, 2022.

[18] M. Elobeid, A. C. Pillai, L. Tao, D. Ingram, J. E. Hanssen, and P. Mayorga, "Implications of wave–current interaction on the dynamic responses of a floating offshore wind turbine," *Ocean Engineering*, vol. 292, p. 116571, 2024.

[19] H. R. Ghafari, H. Ghassemi, and G. He, “Numerical study of the wavestar wave energy converter with multi-point-absorber around deepcwind semisubmersible floating platform,” *Ocean Engineering*, vol. 232, p. 109177, 2021.

[20] Y. Wang, W. Shi, C. Michailides, L. Wan, H. Kim, and X. Li, “Wec shape effect on the motion response and power performance of a combined wind-wave energy converter,” *Ocean Engineering*, vol. 250, p. 111038, 2022.

[21] M. Chen, J. Deng, Y. Yang, H. Zhou, T. Tao, S. Liu, L. Sun, and L. Hua, “Performance analysis of a floating wind–wave power generation platform based on the frequency domain model,” *Journal of Marine Science and Engineering*, vol. 12, no. 2, 2024.

[22] K. Zhu, H. Shi, S. Zheng, S. Michele, and F. Cao, “Hydrodynamic analysis of hybrid system with wind turbine and wave energy converter,” *Applied Energy*, vol. 350, p. 121745, 2023.

[23] P. Jin, Z. Zheng, Z. Zhou, B. Zhou, L. Wang, Y. Yang, and Y. Liu, “Optimization and evaluation of a semi-submersible wind turbine and oscillating body wave energy converters hybrid system,” *Energy*, vol. 282, p. 128889, 2023.

[24] Z. Zhang, Y. Bu, H. Wu, L. Wu, and L. Cui, “Parametric study of the effects of clump weights on the performance of a novel wind-wave hybrid system,” *Renewable Energy*, vol. 219, p. 119464, 2023.

[25] P. Sun, S. Yang, Z. Liu, K. Sun, and Y. Li, “Comprehensive performance analysis of a semi-submersible multi-arm-buoy wec system with various catenary mooring configurations,” *Energy*, p. 141238, 2026.

[26] L. Cui, H. Wu, M. Li, M. Lu, W. Liu, and Z. Zhang, "Effects of mooring failure on the dynamic behavior of the power capture platforms," *Energy*, vol. 313, p. 133761, 2024.

[27] C. F. Lee, S. Fjermedal, and M. C. Ong, "Design and comparative analysis of mooring systems for a combined wind and wave energy system at intermediate water depth," *Journal of Ocean Engineering and Science*, vol. 10, no. 4, pp. 492–508, 2025.

[28] Y. Li, M. C. Ong, K. Wang, L. Li, and Z. Cheng, "Power performance and dynamic responses of an integrated system with a semi-submersible wind turbine and four torus-shaped wave energy converters," *Ocean Engineering*, vol. 259, p. 111810, 2022.

[29] Z. Chen, J. Sun, J. Yang, Y. Sun, Q. Chen, H. Zhao, P. Qian, Y. Si, and D. Zhang, "Experimental and numerical analysis of power take-off control effects on the dynamic performance of a floating wind-wave combined system," *Renewable Energy*, vol. 226, p. 120353, 2024.

[30] E. Homayoun, S. Panahi, H. Ghassemi, G. He, and P. Liu, "Power absorption of combined wind turbine and wave energy converter mounted on braceless floating platform," *Ocean Engineering*, vol. 266, p. 113027, 2022.

[31] T. Liu, Y. Liu, S. Huang, and G. Xue, "Research on dual-objective control of the wind-wave hybrid system with an aerodynamic-hydrodynamic-hydraulic-mooring coupled model," *Physics of Fluids*, vol. 37, no. 9, p. 097133, 2025.

[32] Z. Zhai, J. Miao, and Z. Guo, "Interaction of short-crested waves with cylinder and concentric segmented arc breakwaters," *Ocean Engineering*, vol. 311, p. 118782, 2024.

[33] L. Li and Y. Liu, "Short-crestedness effect on the dynamic response of offshore floating wind turbines," *Ships and Offshore Structures*, vol. 17, no. 10, pp. 2272–2281, 2022.

[34] S. Tödter, J. Neugebauer, and O. el Moctar, "Experimental investigation of the influence of short-crested seas and swell on sloshing-induced impact loads," in *The 33rd International Ocean and Polar Engineering Conference*, 2023, pp. ISOPE–I–23–369.

[35] H. Zhang, S. Liu, J. Li, R. Zhang, and J. Hao, "Interactions between multi-directional irregular waves and a pile group in a side-by-side arrangement: Statistical analysis," *Coastal Engineering*, vol. 147, pp. 115–134, 2019.

[36] J. Jiao, C. Chen, and H. Ren, "A comprehensive study on ship motion and load responses in short-crested irregular waves," *International Journal of Naval Architecture and Ocean Engineering*, vol. 11, no. 1, pp. 364–379, 2019.

[37] M. Göteman, C. McNatt, M. Giassi, J. Engström, and J. Isberg, "Arrays of point-absorbing wave energy converters in short-crested irregular waves," *Energies*, vol. 11, no. 4, 2018.

[38] X. Ji, S. Liu, H. B. Bingham, and J. Li, "Multi-directional random wave interaction with an array of cylinders," *Ocean Engineering*, vol. 110, pp. 62–77, 2015.

[39] S. H. Sørum, J. R. Krokstad, and J. Amdahl, "Wind-wave directional effects on fatigue of bottom-fixed offshore wind turbine," *Journal of Physics: Conference Series*, vol. 1356, no. 1, p. 012011, 2019.

[40] T. Viuff, B. J. Leira, X. Xiang, and O. Øiseth, "Effects of wave directionality on extreme response for a long end-anchored floating bridge," *Applied Ocean Research*, vol. 90, p. 101843, 2019.

[41] C. C. Tung and N. E. Huang, "Influence of current on statistical properties of waves," *Journal of the Waterways, Harbors and Coastal Engineering Division*, vol. 100, no. 4, pp. 267–278, 1974.

[42] C. Guedes Soares and H. de Pablo, "Experimental study of the transformation of wave spectra by a uniform current," *Ocean Engineering*, vol. 33, no. 3, pp. 293–310, 2006.

[43] R. J. Lai, S. R. Long, and N. E. Huang, "Laboratory studies of wave-current interaction: Kinematics of the strong interaction," *Journal of Geophysical Research: Oceans*, vol. 94, no. C11, pp. 16 201–16 214, 1989.

[44] G. P. Thomas, "Wave-current interactions: an experimental and numerical study. part 1. linear waves," *Journal of Fluid Mechanics*, vol. 110, p. 457–474, 1981.

[45] L. Chen and B. Basu, "Wave-current interaction effects on structural responses of floating offshore wind turbines," *Wind Energy*, vol. 22, no. 2, pp. 327–339, 2019.

[46] S. Sarkar, L. Chen, B. Fitzgerald, and B. Basu, "Multi-resolution wavelet pitch controller for spar-type floating offshore wind turbines including wave-

current interactions," *Journal of Sound and Vibration*, vol. 470, p. 115170, 2020.

[47] X. Qu, Y. Li, Y. Tang, Z. Hu, P. Zhang, and T. Yin, "Dynamic response of spar-type floating offshore wind turbine in freak wave considering the wave-current interaction effect," *Applied Ocean Research*, vol. 100, p. 102178, 2020.

[48] Z. Xin, X. Li, and Y. Li, "Coupled effects of wave and depth-dependent current interaction on loads on a bottom-fixed vertical slender cylinder," *Coastal Engineering*, vol. 183, p. 104304, 2023.

[49] T. P. Mazarakos and S. A. Mavrakos, "Wave-current interaction effects on the oc4 deepcwind semi-submersible floating offshore wind turbine," *Journal of Marine Science and Engineering*, vol. 12, no. 9, 2024.

[50] O. SINTEF, *Veres3D User Manual*, SINTEF Ocean, Trondheim, Norway, 2020.

[51] Q. Cao, L. Xiao, Z. Cheng, and M. Liu, "Dynamic responses of a 10 mw semi-submersible wind turbine at an intermediate water depth: A comprehensive numerical and experimental comparison," *Ocean Engineering*, vol. 232, p. 109138, 2021.

[52] M. A. Bhinder, A. Babarit, L. Gentaz, and P. Ferrant, "Potential time domain model with viscous correction and cfd analysis of a generic surging floating wave energy converter," *International Journal of Marine Energy*, vol. 10, pp. 70–96, 2015.

[53] M. Yue, Q. Liu, C. Li, Q. Ding, S. Cheng, and H. Zhu, "Effects of heave plate on dynamic response of floating wind turbine spar platform under the

coupling effect of wind and wave," *Ocean Engineering*, vol. 201, p. 107103, 2020.

[54] M. Fontana, P. Casalone, S. A. Sirigu, G. Giorgi, G. Bracco, and G. Mattiazzo, "Viscous damping identification for a wave energy converter using cfd-urans simulations," *Journal of Marine Science and Engineering*, vol. 8, no. 5, 2020.

[55] Q. Cao, E. E. Bachynski-Polić, Z. Gao, L. Xiao, Z. Cheng, and M. Liu, "Experimental and numerical analysis of wind field effects on the dynamic responses of the 10 mw spic floating wind turbine concept," *Ocean Engineering*, vol. 261, p. 112151, 2022.

[56] H. S. Yang, A. Alkhabbaz, W. Tongphong, and Y. H. Lee, "Cross-comparison analysis of environmental load components in extreme conditions for pontoon-connected semi-submersible fowt using cfd and potential-based tools," *Ocean Engineering*, vol. 304, p. 117248, 2024.

[57] N. D. P. Barltrop, *Floating structures: a guide for design and analysis.* Centre for Marine and Petroleum Technology, 1998.

[58] Z. M. Yuan, A. Incecik, S. Dai, D. Alexander, C. Y. Ji, and X. Zhang, "Hydrodynamic interactions between two ships travelling or stationary in shallow waters," *Ocean Engineering*, vol. 108, pp. 620–635, 2015.

[59] J. Newman, "The theory of ship motions," *Advances in Applied Mechanics*, vol. 18, pp. 221–283, 1979.

[60] J. L. Hess and A. M. O. Smith, "Calculation of nonlifting potential flow about arbitrary three-dimensional bodies," *Journal of Ship Research*, vol. 8, no. 04, pp. 22–44, 1964.

[61] C. Yang, Z. Lu, C. Li, and L. Johanning, "Semi-analytical study on the hydrodynamic performance of an integrated wave energy extraction system consisting of a heaving buoy over a sill and a jarlan-type breakwater," *Ocean Engineering*, vol. 316, p. 119998, 2025.

[62] S. Gueydon, T. Duarte, and J. Jonkman, "Comparison of second-order loads on a semisubmersible floating wind turbine," in *International Conference on Offshore Mechanics and Arctic Engineering*, 2014, p. V09AT09A024.

[63] J. A. Pinkster, "Low frequency second order wave exciting forces on floating structures," Ph.D. dissertation, Technische Universiteit Delft, 1980.

[64] J. Newman, "Second-order, slowly-varying forces of vessels in irregular waves," in *International Symposium on the Dynamics of Marine Vehicles and Structures in Waves*, 1974.

[65] I. Ansys, *AQWA Theory Manual*, ANSYS, Inc., Canonsburg, PA, USA, 2020.

[66] A. W. Lewis and R. N. Allos, "Jonswap's parameters: Sorting out the inconsistencies," *Ocean Engineering*, vol. 17, no. 4, pp. 409–415, 1990.

[67] O. M. Phillips, "The dynamics of the upper ocean," *Journal of Fluid Mechanics*, vol. 88, no. 4, pp. 793–794, 1977.

[68] B. Molin, *Offshore structure hydrodynamics.* Cambridge University Press, 2022.

[69] O. M. Faltinsen, *Sea loads on ships and offshore structures.* Cambridge University Press, 1993.

[70] L. Li, Z. Hu, J. Wang, and Y. Ma, "Development and validation of an aero-hydro simulation code for an offshore floating wind turbine," *Journal of Ocean and Wind Energy*, vol. 2, pp. 1–11, 2015.

[71] S. Li, T. Moan, S. Fu, S. Zhang, and Y. Xu, "Hydroelastic analysis of a floating bridge under spatially inhomogeneous waves, with emphasis on the effect of drift force modeling," *Applied Ocean Research*, vol. 139, p. 103666, 2023.

[72] J. Yang and Z. Hu, "Dynamic modelling of mooring system for integrated analysis of floating offshore wind turbines," *Ocean Engineering*, vol. 342, p. 122916, 2025.

[73] M. Masciola, J. Jonkman, and A. Robertson, "Extending the capabilities of the mooring analysis program: A survey of dynamic mooring line theories for integration into fast," in *International Conference on Offshore Mechanics and Arctic Engineering*, 2014.

[74] M. Hall and A. Goupee, "Validation of a lumped-mass mooring line model with deepcwind semisubmersible model test data," *Ocean Engineering*, vol. 104, pp. 590–603, 2015.

[75] J. R. Morison, J. W. Johnson, and S. A. Schaaf, "The force exerted by surface waves on piles," *Journal of Petroleum Technology*, vol. 2, no. 05, pp. 149–154, 1950.

[76] V. Aslanov, G. Kruglov, and V. Yudintsev, “Newton–euler equations of multibody systems with changing structures for space applications,” *Acta Astronautica*, vol. 68, no. 11, pp. 2080–2087, 2011.

[77] O. A. Bauchau, “A self-stabilized algorithm for enforcing constraints in multibody systems,” *International Journal of Solids and Structures*, vol. 40, no. 13, pp. 3253–3271, 2003.

[78] S. Sarkar and B. Fitzgerald, “Use of kane’s method for multi-body dynamic modelling and control of spar-type floating offshore wind turbines,” *Energies*, vol. 14, no. 20, 2021.

[79] Z. Zheng, P. Jin, Q. Huang, B. Zhou, R. Xiang, Z. Zhou, and L. Huang, “Motion response and energy harvesting of multi-module floating photovoltaics in seas,” *Ocean Engineering*, vol. 310, p. 118760, 2024.

[80] D. Q. Zhang, Z. M. Yuan, G. W. Zhao, Y. J. Chen, and J. F. Du, “An experimental and numerical study of motion responses of multi-body arrays with hinge connections,” *Journal of Marine Science and Engineering*, vol. 12, no. 10, p. 1791, 2024.

[81] X. Zhao, J. Wang, S. Geng, J.and Zhou, and C. Guedes Soares, “Hydrodynamic investigation of a multi-module floating platform with a wave energy device array,” *China Ocean Engineering*, vol. 38, p. 1034–1046, 2024.

[82] L. Sun, R. E. Taylor, and Y. S. Choo, “Responses of interconnected floating bodies,” *The IES Journal Part A: Civil & Structural Engineering*, vol. 4, no. 3, pp. 143–156, 2011.

[83] W. E. Cummins, "The impulse response function and ship motions," *Schiffstechnik*, vol. 9, pp. 101–109, 1962.

[84] C. Jin, I. Lee, F. Bakti, D. K. Kim, S. Kim, and M. Kim, "Multi-body-based 2d hydro-elasticity simulations in time domain for moored floating structure," *Engineering Structures*, vol. 329, p. 119789, 2025.

[85] F. Huo, H. Zhang, D. Yang, and J. Cui, "Sensitivity analysis of non-linear air gap and wave slamming load with respect to current for semi-submersible platform design," in *The Twenty-fifth International Ocean and Polar Engineering Conference*, 2015, pp. ISOPE–I–15–024.

[86] W. Wei, S. Fu, T. Moan, Z. Lu, and S. Deng, "A discrete-modules-based frequency domain hydroelasticity method for floating structures in inhomogeneous sea conditions," *Journal of Fluids and Structures*, vol. 74, pp. 321–339, 2017.

[87] H. R. Ghafari, H. Ghassemi, and K. A. Vakilabadi, "Hydrodynamic performance and power absorption of the hybrid wind-wave energy systems with different platform geometries," *Ocean Engineering*, vol. 332, p. 121440, 2025.

[88] Q. Cao, L. Xiao, and Z. Cheng, "An experimental study on dynamic behavior of a new concept of 10mw semi-submersible wind turbine," in *International Ocean and Polar Engineering Conference*, 2020, pp. ISOPE–I–20–1310.

[89] Q. Cao, L. Xiao, Z. Cheng, and M. Liu, "Dynamic responses of a 10 mw semi-submersible wind turbine at an intermediate water depth: A comprehensive numerical and experimental comparison," *Ocean Engineering*, vol. 232, p. 109138, 2021.

[90] G. He, C. Liu, W. Zhang, Z. Luan, and Z. Zhang, “Numerical study of the effect of central platform motion on the wave energy converter array,” *Ocean Engineering*, vol. 286, p. 115483, 2023.

[91] B. Zhou, J. Hu, K. Sun, Y. Liu, and M. Collu, “Motion response and energy conversion performance of a heaving point absorber wave energy converter,” *Frontiers in Energy Research*, vol. 8, 2020.

[92] Y. Wang, L. Zhang, C. Michailides, L. Wan, and W. Shi, “Hydrodynamic response of a combined wind–wave marine energy structure,” *Journal of Marine Science and Engineering*, vol. 8, no. 4, 2020.

[93] Q. Cao, L. Xiao, Z. Cheng, M. Liu, Y. Chen, and K. Zhang, “Research on the conceptual design and performance analysis of a 10 mw spic concept floating wind turbine foundation in intermediate water depth,” *Journal of Renewable and Sustainable Energy*, vol. 15, no. 6, p. 063303, 2023.

[94] Y. M. Low and A. J. Grime, “Extreme response analysis of floating structures using coupled frequency domain analysis,” *Journal of Offshore Mechanics and Arctic Engineering*, vol. 133, no. 3, p. 031601, 2011.

[95] C. Srinivasan, B. Shah, and Y. J. Chauhan, “Dynamic analyses of triceratops under hurricane-driven metocean conditions in gulf of mexico,” *Ocean Engineering*, vol. 256, p. 111511, 2022.